CRS-based minimum-aperture Kirchhoff migration in the time domain

---

CRS-basierte Kirchhoff-Migration mit minimaler Apertur im Zeitbereich

Zur Erlangung des akademischen Grades eines

DOKTORS DER NATURWISSENSCHAFTEN

von der Fakultät für Physik der

Universität Karlsruhe (TH)

genehmigte

DISSERTATION

von

Dipl.-Geophys. Miriam Eva Tanja Spinner

aus

Ludwigshafen

Abstract

A key element in the seismic imaging sequence is migration, the transformation of the preprocessed seismic data into a structural image of the subsurface which resembles the distribution of geological interfaces. Thus, the primary aim of migration is to reverse the effects of wave propagation. So-called true-amplitude migration schemes additionally appropriately compensate for the dynamic effects of the wave propagation. This allows to recover reflection amplitudes which can be directly related to the angle-dependent reflection coefficients at the interfaces. The latter can finally be inverted for physical properties which characterise the adjacent rock formations.

Migration requires a solution of the elastodynamic wave equation which is usually employed to describe the wave propagation in the Earth. Various approaches for this task have been proposed. In this thesis, I consider the Kirchhoff migration which is based on an integral solution of the wave equation. An additional weighting factor ensures that the migrated output is true-amplitude.

The evident output domain of migration is the depth domain in which the migrated image resembles the actual geological structures. However, in this domain the solution of the wave equation requires a model of the velocity distribution in depth. Errors in the estimated model lead to poorly focussed and mispositioned images and additionally bias the migrated amplitudes. Time migration has been introduced as an approximate alternative requiring only smooth models of integral velocities. As time migration shows a strongly reduced sensitivity to model errors, it is well suited for studies on reflection amplitudes. The time-migrated image is still defined in the time domain, thus requiring a subsequent time-to-depth conversion for interpretation.

Kirchhoff migration can be realised in terms of a so-called diffraction stack based on Huygens' principle. From a theoretical point of view, such a diffraction stack requires an integration over an infinite aperture. Of course, this is infeasible due to the always finite acquisition area. Therefore, an optimum finite aperture has to be defined which guarantees optimal resolution in the image, physically sound amplitudes, and the highest possible signal-to-noise ratio at the same time. This optimum aperture corresponds to the minimum aperture given by the size of the first projected Fresnel zone. It is centred around the stationary point where the migration operator is tangent to the actual reflection event. The usually employed smooth migration velocity models obtained by means of stacking velocities or by migration velocity analysis are not sufficient to calculate these properties prior to migration. Thus, minimum-aperture migration cannot be addressed by conventional migration schemes.

In this thesis, a generalisation of stacking velocity analysis called Common-Reflection-Surface stack method is utilised to obtain information beyond stacking velocity. Based on a spatial stacking operator, the Common-Reflection-Surface stack provides a whole set of stacking parameters which characterise the kinematics of the reflection events. These so-called kinematic wavefield attributes cannot only be utilised in the migration velocity model building but also to estimate the location of the stationary

point and the size of the projected Fresnel zone. This allows a direct application of (true-amplitude) minimum-aperture migration.

In this thesis, the theoretical background as well as the practical application of minimum-aperture Kirchhoff migration in the time domain is discussed for the 2.5D and 3D case. I demonstrate the potential of the method for synthetic as well as real datasets. The time-domain approach allows an efficient and stable implementation of the minimum-aperture estimation due to the considered analytic migration operators. The main observation is an overall improved quality of the migrated images, reduced imaging artifacts, and a higher signal-to-noise ratio. Amplitudes extracted from the migrated images show less scattering and better defined AVO/AVA responses compared to the conventional approach.

Zusammenfassung

Vorbemerkung: Die vorliegende Dissertation ist bis auf diese Zusammenfassung in englischer Sprache geschrieben. Da auch in der deutschen Sprache einige englische Fachausdrücke gebräuchlich sind, wurde bei diesen Ausdrücken auf eine Übersetzung verzichtet. Sie werden, mit Ausnahme ihrer groß geschriebenen Abkürzungen, *kursiv* dargestellt.

Einleitung

Ziel der Geophysik ist es, die Struktur, Zusammensetzung und Dynamik der Erde mittels quantitativer physikalischer Methoden zu erfassen. In der Explorationsgeophysik werden diese Methoden bei der Auffindung und Erschließung von Kohlenwasserstoff- und Minerallagerstätten eingesetzt. Das dabei am häufigsten angewandte Verfahren ist die Reflektionsseismik, bei der künstlich generierte akustische oder elastische Wellen zur Untersuchung des Untergrundes verwendet werden. Als Quellen dienen meist Explosionen oder hydraulisch erzeugte Vibrationen. Die Wellen werden an geologischen Grenzschichten, d. h. an Unstetigkeitsstellen der elastischen Parameter des Untergrundes, reflektiert, transmittiert und gestreut. Ein Teil der elastischen Energie kehrt schließlich an die Erdoberfläche zurück. Dort wird mit Hilfe von sogenannten Geophonen die Bodenbewegung (im Falle von Landseismik) bzw. Druckänderung (bei mariner Seismik) als Funktion der Zeit registriert.

Durch die Kombination mehrerer solcher Einzelexperimente mit verschiedenen Quell- und Empfängerpositionen erhält man einen mehrfach überdeckten Datensatz, aus dem mittels reflektionsseismischer Bildgebungsverfahren (*seismic imaging*) ein strukturelles Abbild des Untergrundes bestimmt werden kann. Dabei wird meist nur ein Teil des im Allgemeinen beliebig komplexen Wellenfeldes betrachtet, in der Regel sind dies unkonvertierte primäre Reflektionen. Werden zusätzlich die dynamischen Aspekte der Wellenausbreitung bei der Datenverarbeitung berücksichtigt, können über die seismische Amplituden die winkelabhängigen Reflektionskoeffizienten an den Grenzschichten bestimmt werden. Diese wiederum erlauben Rückschlüsse auf die physikalischen Eigenschaften der Gesteine an den Grenzschichten.

Strahlentheorie

Die mathematische Beschreibung für die Ausbreitung elastischer Wellen in der Erde liefert die Kontinuumsmechanik in Form der elastodynamischen Wellengleichung, die die räumlichen und zeitlichen Änderungen der Partikelverschiebung miteinander verknüpft. Die Lösung seismischer Inversionsprobleme basiert oft auf der Strahlentheorie, welche eine approximative Hochfrequenzlösung

der Wellengleichung für inhomogene Medien darstellt. Hierbei wird angenommen, dass sich die charakteristischen Größen des betrachteten Mediums über die Wellenlänge des seismischen Signals nicht signifikant ändern.

Über einen Reihenansatz ergeben sich zwei fundamentale Gleichungen zur Beschreibung der Kinematik und Dynamik ausgewählter Wellentypen: die Eikonal- und die Transportgleichung. Zur Vereinfachung wird die Reihenentwicklung meist auf den Term nullter Ordnung beschränkt (*zero-order ray theory*), der zur Beschreibung elementarer Wellentypen ausreicht. Die Lösung der Eikonalgleichung führt auf das kinematische *ray-tracing* System, aus dem sich die Strahlen als Charakteristiken des Wellenfeldes ergeben. Bei bekannter Geschwindigkeitsverteilung kann die Laufzeit eines Signals dann durch einfache Integration entlang des Strahlwegs bestimmt werden. Die dazugehörige Amplitude ergibt sich durch anschließende Lösung der Transportgleichung entlang des zuvor bestimmten Strahls. Dabei zeigt sich, dass die Amplitude eng mit dem *ray Jacobian* und somit der Strahldichte verknüpft ist.

Die paraxiale Erweiterung der Strahlentheorie approximiert schließlich die Laufzeit entlang von Strahlen in der unmittelbaren Nähe eines bekannten (Zentral-)Strahls. Eng mit dem zugehörigen paraxialen *ray-tracing* System ist das dynamische *ray-tracing* System verknüpft, mit dessen Hilfe sich Größen wie der geometrische Ausbreitungsverlust bestimmen lassen.

Common-Reflection-Surface Stapelung

Sogenannte Stapelungsmethoden stellen einen wichtigen Schritt in der seismischen Datenverarbeitung dar. Hierbei wird die Redundanz der mehrfach überdeckten Daten genutzt, um den kinematischen Einfluss der Messgeometrie aus den Daten zu entfernen. Durch Summation (Stapelung) der so korrigierten Daten simuliert man eine sogenannte *zero-offset* Sektion, bei der Schuss- und Empfängerposition koinzident sind. Im Allgemeinen weist diese Sektion ein verbessertes Signal-zu-Rauschen-Verhältnis im Vergleich zu den mehrfach überdeckten Daten auf und liefert einen ersten Eindruck von der Struktur des Untergrundes.

Konventionelle Stapelungsmethoden beschreiben die Abhängigkeit der Reflektionslaufzeit vom Quell-Empfänger-Abstand über eine hyperbolische Laufzeitapproximation. Dieser Operator wird in der Regel über eine sogenannte *normal-moveout* (NMO) oder *stacking* Geschwindigkeit parametrisiert, die sich physikalisch als integrale Geschwindigkeit des Überbaus eines Reflektionspunktes interpretieren lässt. Durch Anpassung der Laufzeitkurven an die tatsächlichen Reflektionsereignisse in den Daten kann so ein integrales Geschwindigkeitsmodell des Untergrundes gewonnen werden.

Die *Common-Reflection-Surface* (CRS) Stapelung kann als verallgemeinerte Geschwindigkeitsanalyse betrachtet werden, bei der die Reflektionsantwort eines Reflektorsegments approximiert wird. Dadurch ergeben sich Stapelsektionen mit deutlich erhöhtem Signal-zu-Rauschen-Verhältnis im Vergleich zu konventionellen Methoden. Zusätzlich liefert die Laufzeitapproximation einen ganzen Satz von Stapelparametern, welche die Kinematik der Reflektionsereignisse charakterisieren. Zwei Anwendungsmöglichkeiten dieser sogenannten kinematischen Wellenfeldattribute oder CRS Attribute werden im Rahmen dieser Arbeit diskutiert: die Bestimmung eines Geschwindigkeitsmodells für die Zeitmigration und die Berechnung optimaler Migrationsaperturen.

Amplitudenbewahrende Kirchhoff-Migration

Ziel der Migration ist es, ein strukturelles Abbild des Untergrundes zu erstellen, das die Verteilung geologischer Schichtgrenzen widerspiegelt. Das Hauptaugenmerk liegt dabei auf den kinematischen Effekten der Wellenpropagation. Durch ihre Kompensation werden Diffraktionsmuster zu den sie verursachenden Punktstreuern kollabiert, Triplikationen entfaltet sowie die Lage und Neigung der Reflektionsereignisse korrigiert. Wenn das Migrationsresultat zusätzlich dynamisch korrekt ist, d. h. die Amplituden im migrierten Abbild einen physikalisch wohldefinierten Wert erhalten, spricht man von amplitudenbewahrender Migration. Dazu müssen bei der Migration die dynamischen Aspekte der Wellenausbreitung, d. h. im Wesentlichen der geometrische Ausbreitungseffekt, kompensiert werden. In einer weiterführenden Analyse des Amplitudenverhaltens mit Quell-Empfängerabstand bzw. Reflektionswinkel (AVO / AVA Analyse) kann dann auf petrophysikalische Eigenschaften des Untergrundes geschlossen werden.

Eine mögliche Formulierung der Migration ist die sogenannte Kirchhoff-Migration. Mathematisch basiert sie auf einer integralen Lösung der Wellengleichung. Eine anschaulichere Betrachtung ergibt sich aus den Abbildungsbedingungen von Hagedoorn. Dabei wird ausgenutzt, dass die Diffraktionslaufzeitfläche oder Huygens-Fläche eines Punktes auf dem Reflektor, die anschaulich als sein kinematisches Abbild im Zeitbereich aufgefasst werden kann, tangential zur Reflektionsantwort im Zeitbereich ist. Gemäß des Huygensschen Prinzips wird in der Kirchhoff-Migration jeder zu migrierende Punkt als Diffraktor aufgefasst, für den bei bekannter Geschwindigkeitsverteilung die zugehörige Huygens-Fläche bestimmt werden kann. Im eigentlichen Migrationsprozess werden die Amplitudenwerte entlang der Huygens-Fläche in den Messdaten aufsummiert und das Ergebnis dem jeweiligen Punkt zugewiesen. Nur für Punkte in unmittelbarer Umgebung tatsächlicher Reflektoren ergeben sich durch die Tangentialität der Operatoren bei der Summation von Null verschiedene Ergebnisse.

Ein migriertes Abbild kann sowohl im Zeit- als auch im Tiefenbereich erstellt werden. Während die Tiefenmigration keine Einschränkungen bezüglich des Mediums macht, basiert die Zeitmigration auf der Annahme einer lateral homogenen Geschwindigkeitsverteilung. In diesem Fall kann ein lokal homogener Überbau angenommen werden, der über eine integrale Geschwindigkeit charakterisiert wird. Der zugehörige Migrationsoperator kann im einfachsten Fall unter der Annahme gerader Strahlwege (*straight-ray approximation*) vollständig analytisch beschrieben werden. In der Praxis wird die Anwendung von Zeitmigration auf Medien mit moderaten lateralen Geschwindigkeitsvariationen erweitert. Der Vorteil der Zeitmigration gegenüber der Tiefenmigration liegt vor allem in der vereinfachten Bestimmung des Geschwindigkeitsmodells und der geringeren Sensitivität des Verfahrens gegenüber fehlerhaften Geschwindigkeitswerten. Auch bei einem ungenau oder fehlerhaft bestimmten Geschwindigkeitsmodell führt Zeitmigration zu einem fokussierten strukturellen Abbild und – vor allem – unverfälschten Amplituden. Daher finden zeitmigrierte Daten häufig Anwendung bei der Analyse von Reflektionsamplituden.

Bestimmung der Zeitmigrationsgeschwindigkeiten aus kinematischen Wellenfeldattributen

Der Zeitmigrationsoperator wird üblicherweise für Medien mit lateral homogener Geschwindigkeitsverteilung über *root-mean-square* (RMS) Geschwindigkeiten parametrisiert. Für horizontale Reflektoren entsprechen diese den NMO Geschwindigkeiten, da in diesem Fall die Bildlokationen im migrierten und unmigrierten Zeitbereich übereinstimmen. In der Praxis wird die Anwendung von Zeitmigration auf Medien mit moderater lateraler Geschwindigkeitsvariation erweitert. Die Parametrisierung des

Operators erfolgt über eine sogenannte Migrationsgeschwindigkeit, die im Apex des Migrationsoperators definiert ist und diesen so aufbaut, dass der Operator optimale Anpassung an die Reflektionsereignisse in den mehrfach überdeckten Daten aufweist. Physikalisch kann dieser Parameter nicht mehr als RMS Geschwindigkeit aufgefasst werden, sondern stellt wie die *stacking* Geschwindigkeit eine Art *best fit* Parameter dar. Konventionell werden diese Geschwindigkeiten in einem iterativen Verfahren aus den Stapelgeschwindigkeiten bestimmt.

Basierend auf den kinematischen Wellenfeldattributen lässt sich ein approximatives Zeitmigrationsgeschwindigkeitsmodell bestimmen, das für moderate Reflektorneigungen und nicht zu große *offsets* eine gute Konsistenz mit den mehrfach überdeckten Daten aufweist. Der Vorteil dieses Verfahrens gegenüber der konventionellen Bestimmung der Migrationsgeschwindigkeiten liegt vor allem in seiner Effizienz und weitgehenden Automatisierung. Für die in dieser Dissertation betrachteten Anwendungen weisen die über CRS Attribute bestimmten Geschwindigkeitsmodelle eine gute Konsistenz mit den mehrfach überdeckten Daten auf, wie an den synthetischen und realen Datenbeispielen gezeigt wird.

Kirchhoff-Zeitmigration mit minimaler Apertur

Die im Rahmen der Kirchhoff-Migration verwendete Diffraktionsstapelung müsste aus theoretischer Sicht mit einer unbegrenzten Apertur durchgeführt werden. Dies ist schon wegen des zwangsläufig begrenzten Messgebiets und der endlichen Aufzeichnungsdauer in der Praxis nicht realisierbar.

Die Qualität des migrierten Abbildes und der Amplituden, aber auch die Effizienz des Migrationsprozesses, hängen stark von der gewählten Aperturgröße ab. Im Fall einer zu kleinen Apertur ist eine verfälschte oder unvollständige Darstellung insbesondere steiler Ereignisse zu erwarten. Bei zu großer Apertur ist andererseits mit verringerter Effizienz und niedrigerem Signal-zu-Rauschen-Verhältnis des Migrationsergebnisses zu rechnen. Zudem steigt in diesem Fall die Wahrscheinlichkeit für das Auftreten bestimmter Migrationsartefakte wie *operator aliasing*. *Antialias* Filter, die zur Verminderung dieser Artefakte eingesetzt werden können, sind im Allgemeinen rechenaufwändig und beeinflussen die Migrationsamplituden. Das Amplitudenverhalten reagiert erwartungsgemäß sehr sensibel auf die Aperturgröße, selbst wenn kaum Artefakte in den migrierten Abbildern zu erkennen sind. Daher ist insbesondere für weiterführende Analysen der Amplituden eine optimale Wahl der finiten Apertur essentiell.

Die Anwendung der Methode der stationären Phase auf das Migrationsintegral ergibt, dass die erwünschten konstruktiven Beiträge zum Migrationsergebnis aus der Umgebung des sogenannten stationären Punktes, d. h. des Tangentialpunktes von Migrationsoperator und Reflektionsantwort, stammen. Die optimale Apertur um diesen stationären Punkt ist durch die erste projizierte Fresnelzone definiert, die gerade der minimalen Apertur entspricht, mit der sich physikalisch sinnvolle Amplituden ergeben.

Eine exakte Bestimmung der minimalen Apertur setzt neben einem Migrationsgeschwindigkeitsmodell auch ein strukturelles Modell der Grenzschichten im Untergrund voraus. Diese Information ist in diesem Stadium der Datenverarbeitung i. d. R. nicht verfügbar. In der konventionellen Migration wird daher die Apertur um den Apex des Migrationsoperators zentriert; die Apertur muss vom Anwender abgeschätzt werden und hinreichend groß sein, um steile Ereignisse abbilden zu können.

Mit Hilfe der kinematischen Attribute aus der CRS Stapelung kann die minimale Apertur und deren Lage für *zero offset* abgeschätzt werden. Ferner erlauben sie in gewissem Umfang auch eine Extrapolation des stationären Punktes zu finiten *offsets*. Alle relevanten Größen werden dabei in zweiter

Ordnung hinsichtlich der Raumkoordinaten approximiert. Jäger (2005a) verwendete diesen Ansatz zur Bestimmung minimaler Aperturen in der Tiefenmigration. Die hohe Empfindlichkeit der Tiefenmigration gegenüber Fehlern im Migrationsgeschwindigkeitsmodell kann allerdings zur fehlerhaften Abschätzung der Apertur und ihrer Lage, und somit zu verfälschten Ergebnissen führen. Es liegt daher nahe, den Ansatz in die Zeitmigration zu überführen. Die dort verwendeten integralen Migrationsgeschwindigkeiten und die analytischen Migrationsoperatoren erlauben eine stabile und effiziente Abschätzung der minimalen Migrationsapertur. Besonders in Hinblick auf die Verwendung der migrierten Amplituden in AVO/AVA Analysen profitiert die Methode vom Übergang in den migrierten Zeitbereich. Darüber hinaus wird der Ansatz im Rahmen dieser Arbeit auch auf den bisher unbehandelten 3D Fall für finite *offsets* erweitert.

Anwendung

Die zuvor eingeführt Methode zur Kirchhoff-Zeitmigration mit minimalen Aperturen wird im Rahmen dieser Dissertation sowohl an synthetischen als auch an Realdaten jeweils für zwei- und dreidimensionale Messgeometrien getestet. Dabei werden die kinematischen Wellenfeldattribute sowohl zur Erstellung der Migrationsgeschwindigkeitsmodelle als auch zur Bestimmung der minimalen Apertur und ihrer Lage verwendet. Für jeden Datensatz werden zusätzlich Vergleichsresultate mit konventioneller Apertur berechnet.

Im Vergleich der jeweiligen Migrationsresultate mit den konventionellen Ergebnissen zeigen sich Verbesserungen bezüglich der Bildqualität der migrierten Sektion sowie bezüglich der migrierten Amplituden. Durch die Beschränkung der Diffraktionsstapelung auf die minimale Apertur kommt es zur verminderten Aufsummierung von Störsignalen und somit zu einem verbesserten Signal-zu-Rauschen-Verhältnis im Migrationsergebnis. Migrationsartefakte werden gleichzeitig reduziert oder treten, wie im Fall des *operator aliasings*, gar nicht auf. Gleichzeitig nimmt die Streuung der migrierten Amplituden ab und Verfälschungen durch Migrationsartefakte oder Störsignale werden vermieden. Die erhöhte Qualität und Zuverlässigkeit der Amplituden zeigt sich auch in weiterführenden Auswertungen wie z. B. der Erstellung eines *crossplots* mittels einer AVA Analyse, wie an Hand des synthetischen 2D Datensatzes beispielhaft gezeigt wird.

Schlussfolgerungen

Im Rahmen dieser Dissertation wurde die Transformation reflektionsseismischer Daten in ein strukturelles Abbild des Untergrundes mittels amplitudenbewahrender Kirchhoff-Migration im Zeitbereich untersucht. Das Hauptaugenmerk der vorliegenden Arbeit liegt auf der Erstellung eines geeigneten Geschwindigkeitsmodells und der Bestimmung optimaler Migrationsaperturen. Bei beiden Aspekten kommen kinematische Wellenfeldattribute zum Einsatz, die mit Hilfe der CRS Stapelung bestimmt werden können.

Für die untersuchten Datenbeispiele hat die vorgestellte Strategie zur Bestimmung der Migrationsgeschwindigkeitsmodelle eine hinreichende Approximation der gesuchten Geschwindigkeiten erlaubt. Verbleibende Inkonsistenzen sind auf die verwendete *straight-ray* Approximation zurückzuführen.

Die aus den Wellenfeldattributen abgeschätzte minimalen Migrationsapertur führt zu einer Verbesserung des migrierten Abbildes, vor allem aber zu deutlich zuverlässigeren Amplituden. Dabei kommt

auch die Anwendung der Migration im Zeitbereich zum Tragen. Sie führt zu einer deutlichen Stabilisierung der Ergebnisse im Vergleich zur Tiefenmigration.

Das vorgestellte Migrationsverfahren basiert auf der Annahme gerader Strahlwege, die zu einer Einschränkung des Anwendungsbereichs auf einfache Untergrundmodelle führt. Erweiterungen auf eine allgemeinere Beschreibung des Migrationsoperators sind jedoch generell möglich. Zudem muss bei der praktischen Anwendung des Verfahrens berücksichtigt werden, dass die Bestimmung der Migrationsapertur jeweils lokal durchgeführt wird und damit direkt von der örtlich und zeitlich variablen Zuverlässigkeit der Attribute abhängt. Eine sorgfältige Bestimmung und Evaluierung der Wellenfeldattribute ist daher unerlässlich.

Zusammenfassend kann die hier vorgestellte Methode der Kirchhoff-Migration mit minimalen Aperturen im Zeitbereich als Ergänzung konventioneller Verfahren angesehen werden, insbesonders im Hinblick auf eine Anwendung auf ausgewählte Zielhorizonte zur weiterführenden Analyse der migrierten Amplituden.

Contents

Chapter 1

Introduction

Geophysics aims at exploring the structure, composition, and dynamics of the Earth using quantitative physical methods. The investigation of the Earth's interior is naturally based on indirect measurements including gravity, reflection and refraction seismics, magnetic, electrical, and electromagnetic techniques. The practical application of these methods in the search for hydrocarbons and mineral deposits is task of exploration geophysics.

In this chapter, I will describe the reflection seismic method which is the most frequently applied technique in the context of oil and gas exploration due to its advantages concerning accuracy, resolution, and penetration depths. Here, the propagation and reflection of artificially generated elastic waves is utilised to gain information about the Earth's reflectivity. Proper processing of the seismic data allows to image and characterise the subsurface. In conjunction with geological and borehole data, this information can be used to map features of interest, e. g., possible locations of hydrocarbon accumulation.

Within the seismic processing sequence, migration, i. e., the transformation of the recorded data into an interpretable image of the subsurface, plays an important role. In this thesis, I present a strategy to incorporate kinematic wavefield attributes obtained by means of the Common-Reflection-Surface (CRS) stack into 2.5D and 3D Kirchhoff migration in order to enhance the quality of the structural image and to increase the reliability of the dynamic information.

1.1 Reflection seismics

As already mentioned, the aim of a seismic reflection experiment is to gain information about the structure and composition of the subsurface. For this purpose, seismic methods utilise artificially generated elastic or acoustic waves which propagate through the area under investigation. These waves are reflected at discontinuities along which the elastic parameters of the Earth change abruptly compared to the scale of the dominant wavelength of the source signal. More precisely, only a part of the energy is reflected while another part is transmitted into the deeper medium. In addition, mode conversion between compressional and shear waves can occur. The part of the reflected wavefield that returns to the surface is recorded. Thereby, spatially continuous events are recognised as wavefronts and referred to as reflection events. Each reflection event is characterised by the lateral emergence locations and the corresponding traveltimes. In general, the wavefield might get quite complicated

1

due to multiple reflections, diffractions, and ground roll, i. e., waves that travel along the Earth's surface. Although all wave types carry information on the subsurface, we are usually only interested in a specific subset of the data: unconverted waves that were reflected only once, so-called primary reflections. From the traveltimes and amplitudes of these events the elastic properties of the rocks as well as the position, orientation, and curvature of reflectors can be deduced by means of seismic processing. All other events are considered as noise and are tried to suppress during the data processing.

Basically, reflection seismics can be divided into three main steps which will be briefly summarised in the following: the acquisition of the seismic data in the field, the seismic data processing, and the structural and stratigraphical interpretation of the obtained results.

1.1.1 Data acquisition

Seismic reflection data is acquired in various environments and acquisition geometries: on land, in transition zones, and in marine environments ranging from shallow to ultradeep waters. Seismic equipment covers a large range that allows to study the subsurface from the near surface down to several tens of kilometres in depth.

In large-scale land seismics, seismic pulses are usually generated by means of explosives or hydraulic vibrators installed on large trucks which produce a frequency-modulated sweep with a duration of several seconds. The reflected wavefield is recorded by geophones as a function of time after excitation of the seismic energy. The measured quantity is one or three components of the particle displacement, velocity, or acceleration. In the marine case, the seismic pulse is generated by the sudden release of highly compressed air into the water. The interconnection of several of these so-called air guns with certain time delays allows to vary the energy level, directivity, and frequency characteristic of the pulse. Marine receivers (hydrophones) are based on piezoelectric sensors which are sensitive to pressure changes.

In commonly applied survey designs, the wavefield generated by one source (often termed shot) is recorded by a multitude of receivers. Due to the high ambiguity in the seismic inversion problem, several of these so-called common-shot (CS) experiments with varying shot and receiver positions are necessary to collect redundant information on the subsurface structure. The obtained multicoverage dataset consists of one discrete time series for each shot-receiver pair which is usually referred to as (seismic) trace, while an ensemble of traces with a certain geometry is referred to as gather. The specific survey design depends on the purpose of the seismic experiment as well as on the complexity of the subsurface structure and environmental conditions. Especially in 3D land seismics, this often leads to irregular geometries which have to be taken into account during processing. Information on seismic survey design can be found in, e. g., Vermeer (2002).

In many seismic processing steps, an appropriate sorting of the recorded multicoverage dataset with respect to the shot-receiver configuration is necessary. The most frequently used configurations are:

- The common-midpoint (CMP) configuration: a CMP gather is made up of all traces that share a common midpoint between shot and receiver location.

- The common-offset (CO) configuration: a CO gather contains traces with the same shot-receiver distance (offset).

- The zero-offset (ZO) configuration: a ZO gather consists of traces with coinciding shot and receiver location and is, thus, a special case of a CO gather.

The different configurations are depicted in Figure 1.1. Their use will be explained in the context of the particular processing steps.

1.1.2 Seismic data processing

The objective of seismic processing is to convert the measured seismic data into an image of the sub-surface which represents the distribution of geological interfaces. Further analyses which do not only consider the kinematic part of the data (related to the traveltimes) but also the dynamic information (related to the amplitudes) additionally allow a characterisation of the elastic properties of the rocks. However, this requires an appropriate treatment of the amplitudes in the processing sequence.

Seismic data processing usually starts in the field. Here, records from nearby shots and receivers are combined to enhance the signal-to-noise ratio. In case of land data, static corrections are usually carried out to correct for topographic elevations and the influence of the weathering layer. The subsequent main processing sequence strongly depends on the geological objectives and the noise conditions. The basic stages of such a processing sequence are briefly addressed in the following. A thorough description of seismic data processing can be found in Yilmaz (2001).

Preprocessing

Before seismic imaging, the raw data has to be preconditioned for the subsequent steps. Usually, this starts with the conversion of the field tapes to a convenient format and dead or corrupt traces are set to zero. In the next step, the field geometry, i. e., shot and receiver coordinates etc., is assigned to the trace headers. By means of filtering, coherent noise or noise outside the considered frequency range can be reduced. Residual static corrections may be applied for land data to deal with small-scale near-surface velocity variations. Automatic gain functions, which are often applied in this stage to compensate for spherical divergence and attenuation losses, should be avoided if amplitudes are to be used in further analyses.

Deconvolution

The next step in seismic data processing is deconvolution. Deconvolution can be regarded as a kind of inverse filter that removes the effects on the source pulse. In doing so, the pulse length is shortened and transformed to zero-phase —ideally to a Dirac impulse— which increases the temporal resolution of the data. For a mathematical description of the different deconvolution methods see, e. g., Buttkus (2000) and references therein.

CMP sorting

After initial signal processing, the data is usually sorted from the recorded CS geometry to CMP gathers. For 2D geometries, the CMP-sorted multicoverage dataset is defined by a midpoint, offset, and time dimension making up a 3D volume. The 3D case, however, is more complicated: here, shot and receiver coordinates are given by 2D vectors which leads to a 5D data (hyper-)volume. In principle, 2D midpoint and offset vectors can be used in analogy to the 2D case. However, there are processing steps like seismic migration where the reformulation in offset azimuth and Euclidean offset is more convenient.
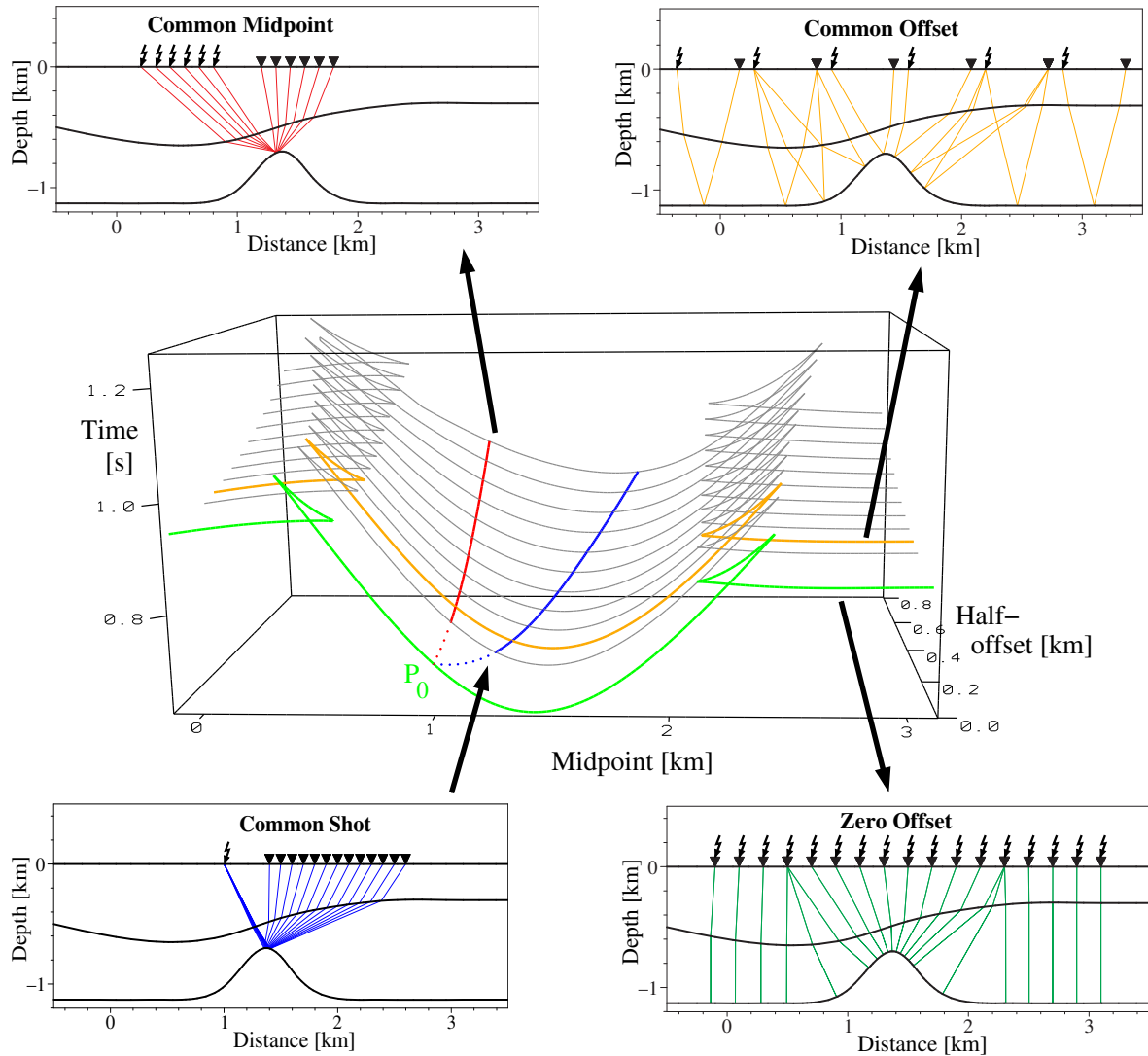
Figure 1.1: Different source and receiver configurations for 2D acquisition. The smaller pictures on the top and the bottom of the figure show selected rays for the different experiments. Shots are marked by flash symbols and receivers by triangles. The sketch in the middle depicts the multicoverage seismic dataset in midpoint m and half-offset h coordinates. Constant-offset traveltime curves are displayed in black. The part of the data which would be obtained by one of the experiments is indicated in colour (figure taken from Höcht, 2002).

Velocity analysis and stacking

For a single horizontal layer with constant velocity, the traveltime curve for one CMP gather constitutes a hyperbola if displayed as function of source-receiver offset. For more general media and reflector geometries the behaviour of the traveltime curve gets quite complicated. Nevertheless, in case of gentle dips and moderate lateral velocity variations, a hyperbolic approximation is still applicable if the maximum considered offset is small[1]. The actual form of the hyperbola is controlled by the so-called normal-moveout (NMO) or stacking velocity which can be regarded as an effective velocity of the medium. For a horizontally stratified medium with constant layer velocities, the NMO or stacking velocity equals the root-mean-square (RMS) velocity. In principle, the definition of NMO and stacking velocities slightly differs: while NMO velocities are based on a small-spread traveltime assuming horizontal layers, stacking velocity are defined for the hyperbola that fits best over the entire offset range. However, this difference is often ignored in practice.

Velocity analysis tools make use of the hyperbolic approximation to derive a model of the effective velocity distribution of the subsurface. A variety of different approaches exist for the automatic analysis of the reflection events, e. g., the signal coherence is evaluated along the hyperbolic trajectories defined by a range of feasible velocity values. The coherence maxima are selected and the corresponding velocities are interpolated along the profile.

The knowledge of the NMO velocity allows to remove the influence of the measurement geometry by a so-called normal-moveout correction. This procedure corrects for the traveltime difference between a finite offset and the (hypothetical) zero-offset ray. In this way, the reflection events in the CMP sections are flattened and can be summed up (stacked) coherently. In case of a homogeneous overburden the summation of these gathers yields a true ZO section, i. e., a hypothetical section that would be obtained with coincident shot and receiver locations. For more complex media, a CMP gather contains data from different reflection points in depth, i. e., it suffers from so-called reflection-point-dispersal which falsifies the results of the velocity analysis and, to a smaller extent, the stacking result. In principle, this effect can be compensated by a dip-moveout (DMO) correction which transforms the CMP gathers to common-reflection-point (CRP) gathers (see Figure 1.2). Unfortunately, this process is only possible with the knowledge of the true medium velocities. As these velocities are not known initially, DMO is applied in an approximate manner. The original data is NMO corrected and the analytic DMO operator for a dipping reflector in a constant velocity medium is applied. A subsequent inverse NMO with the previously obtained velocities yields a new prestack dataset which, in general, provides better results in the velocity analysis.

With the stacking process, one ZO trace is obtained for each CMP gather. In this way, not only the amount of data is significantly reduced compared to the multicoverage dataset, but also the signal-to-noise ratio is increased by approximately $\sqrt{N}$ where N is the number of traces in the CMP gather. The latter is based on the fact that the uncorrelated noise is less amplified in the stacking process than the reflected signal. The ZO section gives a first impression of the subsurface structure. However, the obtained image is inaccurate as the effects of the wave propagation are not completely removed from the data. For this purpose, an additional processing step is necessary that *migrates* the reflectors to their correct dip and spatial location.

---

[1]As a rule of thumb, for a considered reflector the source-receiver offset should not exceed the expected depth.
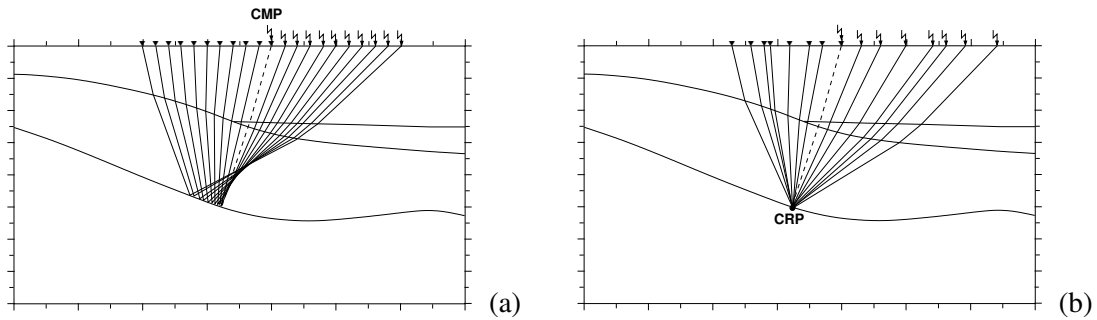
Figure 1.2: Comparison of (a) a common-midpoint (CMP) and (b) a common-reflection-point (CRP) experiment. For non-horizontal reflectors or lateral velocity variations, a CMP gather reveals reflection point dispersal, i. e., the reflection events do not illuminate the same point on the reflector.
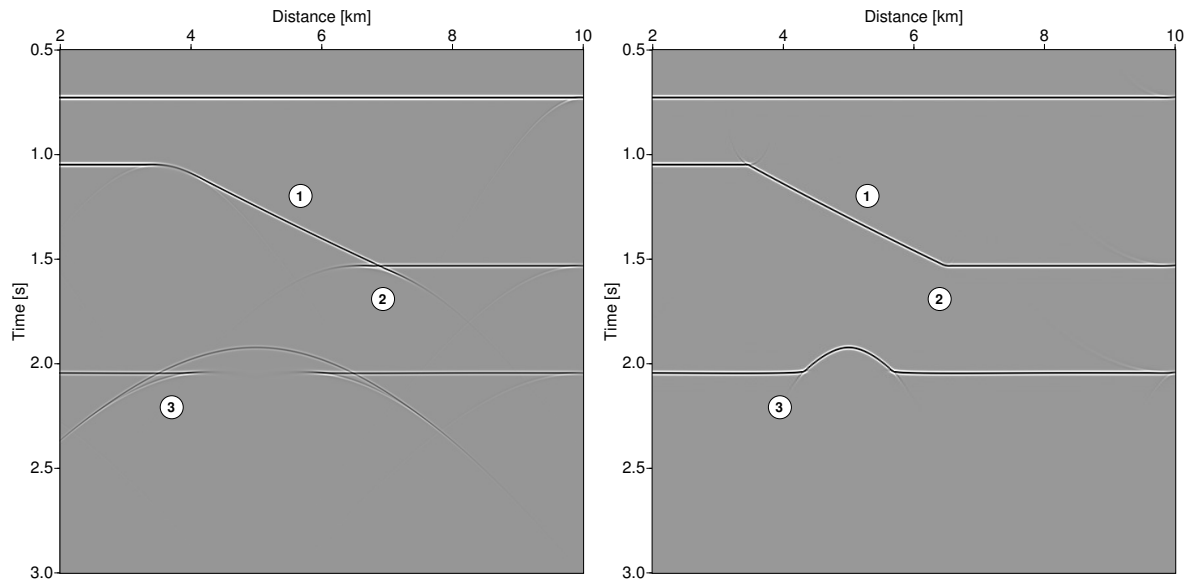
Migration

Seismic migration is a wave-equation based process that removes the influence of the reflector overburden from the data. In detail, migration alters the location and inclination of reflection events, collapses diffraction patterns that are caused by point scatterers and unfolds triplications. In Figure 1.3, a ZO section is displayed before (left) and after (right) migration. The extension to true-amplitude migration supplementary accounts for the dynamic effects related to the seismic amplitudes of the wave-propagation process. By incorporating proper amplitude handling into the migration scheme, additional information about geological and physical properties of the subsurface can be extracted from the migrated image. In order to obtain a physically well-defined value for the amplitudes in the migrated image, the amplitude change during wave propagation has to be compensated in the migration process. Under the assumption of weak parameter contrasts at seismic interfaces, the only major influence on the amplitudes besides the reflection results from geometrical spreading effects. Thus, it is usually assumed that all other factors affecting seismic amplitudes are either negligible or that they are already corrected for before migration. Therefore, by compensating for the geometrical spreading factor, the resulting amplitude of the reconstructed source pulse is proportional to the reflection coefficient. This product, i. e., the source wavelet multiplied with the reflection coefficient, is traditionally called a *true-amplitude* signal.

The migrated seismic section can be constructed in the time (time migration) or in the depth domain (depth migration). In both cases, appropriate velocity information is essential. Whereas time migration is based on integral velocity information, depth migration requires the true medium velocities. The difference between both techniques is not only the different domain in which the migrated section is constructed: time migration locally assumes a 1D medium and, thus, fails for strong lateral variations. Although depth seems to be the natural domain for an image of the geological structure, time migration is frequently applied because the velocity model building is simplified and errors have less impact on the migration result and, in particular, the amplitudes. Moreover, it allows a direct comparison with the unmigrated section for interpretation.

Both time and depth migration can either be applied to the full multicoverage dataset (prestack migration) or the simulated ZO section (poststack migration). In prestack migration, the migration process is separately carried out for each offset bin[2] (or offset-azimuth bin in 3D) where offsets within a cer-

---

[2]Alternatively, a parameterisation in terms of common scattering angle is possible, leading to the so-called common-

Figure 1.3: Comparison of a ZO section before (left) and after (right) time migration. Seismic migration alters the location and inclination of reflection events (1), collapses diffractions (2) and unfolds triplications (3).

tain range are combined to guarantee a sufficient number of traces. While poststack migration is faster and usually provides a clearer image due to the improved S/N-ratio of the input section, it might fail for complex structures. Moreover, only prestack migration allows to check the quality of the velocity model as it provides a separate image of the subsurface for each offset panel. This allows to extract so-called common-image gathers (CIGs) in which traces that belong to a common lateral position are displayed as a function of offset. If the velocity model is consistent with the input data, all the common-offset sections are kinematically equivalent. Thus, the events in the CIGs are flat. A positive moveout, i. e., images of larger offset appear at smaller traveltimes compared to those from shorter offsets, indicates that the migration velocity was too low and vice versa. Therefore, prestack migrated gathers allow to extract informations for an update of the velocity model. The range of application for pre- and poststack migration in the time and depth domain is depicted in Figure 1.4.

Various migration algorithms have been developed which are in general variations of three different approaches (Sheriff and Geldart, 1982): an integral solution of the wave equation (Kirchhoff or diffraction stack migration), a solution of the wave equation in the frequency domain (e. g., Stolt or Gazdag migration), or a finite-difference approach in the time domain. Among those, Kirchhoff migration is one of the oldest techniques but it is still widely used especially in 3D as it is less compute-intensive than the other methods and highly parallelisable. Moreover, it allows a target-oriented application, i. e., the imaging of a selected region in the output space, and can handle irregular geometries. Drawbacks of the method are mainly related to the Green's function tables (GFTs) required for migration. GFTs provide the traveltime information and optional the dynamic properties for the calculation of the weight function and are usually calculated on the basis of zero-order ray theory which will be presented in the next chapter. A discussion of advantages and disadvantages of the different methods and especially Kirchhoff migration can be found in, e. g., Gray (2001) and Robein (2003).

---

angle migration.
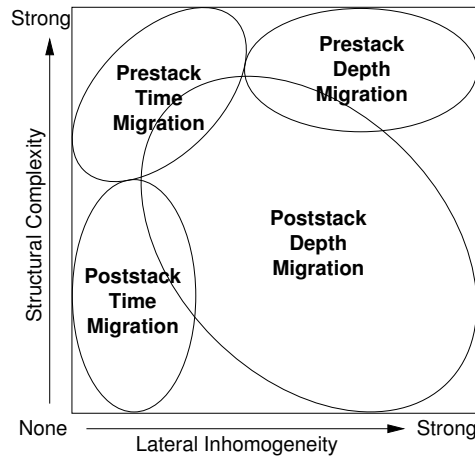
Figure 1.4: Range of application for pre-and poststack time and depth migration. Time migration is suitable for small to moderate lateral velocity variations, strong lateral inhomogeneities require depth migration. Prestack migration has to be carried out if the structure of the subsurface is complex (after Liner, 1999).

Amplitude analyses

After a true-amplitude migration, the migrated seismic signal becomes a direct measure of the reflection coefficient which itself depends on the reflection angle and, thus, on the lithology, porosity, and fluid content of the rocks at the considered interface. From an analysis of amplitude variation with offset (AVO) or reflection angle (AVA) conclusions can be drawn on the elastic properties of the medium and anomalies that might indicate gas or oil accumulation. Most popular hydrocarbon indicators are so-called bright spots (associated with a local increase in amplitude) or dim spots (a local decrease). Flat spots, i. e., discordant horizontal reflectors, indicate an interface between two fluids such as gas-oil or gas-water.

1.1.3 Seismic interpretation

Seismic interpretation aims at determining the geological significance of the seismic data. This includes the *structural analysis* of the reflector geometry to identify potential reservoirs, and the *stratigraphical analysis* that relates reflections to chronostratigraphical units. Input for both techniques are the migrated sections together with the unmigrated counterparts. In case of time migration, an additional conversion to depth is necessary; well measurements of the considered target region can be used for the calibration of the seismic data. The analyses are complemented by seismic modelling, i. e., the building of synthetic sections based on sonic log data to gain physical insight into the subsurface parameters.

1.2 Outline of this thesis

In this chapter, a brief introduction into the reflection seismic method was given and the main steps in a seismic processing workflow were summarised.

Chapter 2 starts with the elastodynamic wave equation as theoretical background of the reflection seismic method. Based on a high-frequency approximation, the ray method provides a solution to the isotropic wave equation in terms of two fundamental equations, namely the eikonal and transport equations. Two extensions of the classical ray theory are presented that find a broad application in seismic modelling and inversion techniques.

The Common-Reflection-Surface (CRS) stack is introduced in Chapter 3 as a generalised high-density stacking velocity analysis tool. Based on a second-order traveltime expansion, the CRS method was originally mainly thought of as alternative to the conventional NMO/DMO/stack sequence for the simulation of stacked sections. Additionally, the CRS stack provides a set of so-called kinematic wavefield attributes that carry detailed information on the kinematics of the reflection events. These attributes will be utilised in the minimum-aperture time migration approach for the derivation of approximate time migration velocities and the estimation of the optimum migration aperture.

Chapter 4 provides the theoretical background for true-amplitude Kirchhoff migration for 3D and 2.5D media. Starting from the depth migration scheme for arbitrary isotropic models, a general expression for the Kirchhoff migration integral and the corresponding true-amplitude weight is derived. Kirchhoff time migration usually assumes a laterally homogeneous subsurface which leads to analytic expressions for the migration formula as well as for the weight function.

Kirchhoff time migration is usually parameterised in terms of root-mean-square velocities defined at the apex of the migration operator. This treatment is strictly valid only for 1D media, otherwise, the required migration velocity constitutes a "best-fit" parameter. In Chapter 5, an approach to derive approximate time migration velocities from the kinematic wavefield attributes is presented and its applicability and limitations are discussed.

The image quality as well as the noise level and the reliability of the migration amplitudes in Kirchhoff migration strongly depend on the selection of the migration aperture. Optimal results are obtained if the migration aperture is restricted to the smallest possible size which governs the constructively contributing part of the migration operator. In Chapter 6, a minimum-aperture approach for Kirchhoff time migration based on the kinematic wavefield attributes is presented. While in the 2.5D case all required information for the estimation of the optimal aperture for pre- and poststack migration can directly be obtained from the CRS attributes, additional assumptions on the velocity distribution are necessary in 3D. However, these restrictions are in accordance with the limitations of time migration.

The minimum-aperture time migration approach is applied to both synthetic and real datasets. The results for the 2D and 3D data are presented in Chapter 7 and 8, respectively. Conventionally obtained migration results are provided for comparison. The benefits and limitations of the minimum-aperture time migration with respect to kinematic and dynamic results are discussed.

Finally, a summary and conclusions are given in Chapter 9.

1.3   Notation and abbreviations

Throughout this thesis, the Einstein summation convention is used, implying summation over repeated indices. The mathematical syntax is summarised in the following tables:

Scalars, vectors, and matrices

	symbol	element
scalar	a	
2D vector	$\mathbf{a}$	$a_i \quad (i = 1, 2)$
3D vector	$\hat{\mathbf{a}}$	$a_i \quad (i = 1, 2, 3)$

	symbol	element
2×2 matrix	$\mathbf{A}$	$A_{ij} \quad (i, j = 1, 2)$
3×3 matrix	$\hat{\mathbf{A}}$	$A_{ij} \quad (i, j = 1, 2, 3)$
4×4 matrix	$\hat{\hat{\mathbf{A}}}$	$A_{ij} \quad (i, j = 1, 2, 3, 4)$

Vector and matrix operations

vector operations	
·	inner product
×	cross product
$\mathbf{a}^{\mathrm{T}}$	transpose of $\mathbf{a}$

matrix operations	
$\hat{\mathbf{A}}^{\mathrm{T}}$	transpose of $\hat{\mathbf{A}}$
$\hat{\mathbf{A}}^{-1}$	inverse of $\hat{\mathbf{A}}$

Vector calculus

The Nabla operator in Cartesian coordinates is denoted by $\hat{\nabla} = (\partial/\partial r_1, \partial/\partial r_2, \partial/\partial r_3)^{\mathrm{T}}$, $\Delta = \hat{\nabla} \cdot \hat{\nabla}$ symbolises the Laplace operator.

vector calculus operations	
$\hat{\nabla} U$	gradient of scalar field U
$\hat{\nabla} \cdot \hat{\mathbf{A}}$	divergence of vector field $\hat{\mathbf{A}}$
$\hat{\nabla} \times \hat{\mathbf{A}}$	curl of vector field $\hat{\mathbf{A}}$

Abbreviations

In this thesis, I make use of the following abbreviations that are common in the literature about reflection seismics:

AVA/AVO	:	amplitude variation with angle/offset
CIG	:	common-image gather
CMP	:	common-midpoint
CO	:	common-offset
CRP	:	common-reflection-point
CRS	:	common-reflection-surface
CS	:	common-shot
DMO	:	dip-moveout
NIP/PIP	:	normal-incidence/paraxial-incidence point
NMO	:	normal-moveout
RMO	:	residual-moveout
RMS	:	root-mean-square
S/N	:	signal-to-noise
ZO	:	zero-offset

Chapter 2

Ray theory

In reflection seismics, the propagation of waves through the Earth is usually described in terms of continuum mechanics. The most fundamental equation in this context is the elastodynamic wave equation, a partial differential equation of second order which can, in general, not be solved analytically for arbitrary complex media. Common approaches rely either on a direct numerical solution of the wave equation by means of finite-difference schemes or on an approximate asymptotic or iterative solution such as the ray theory or the WKBJ method. Although the approximate methods suffer from a limited range of validity and applicability, they are commonly utilised in both forward and inverse seismic problems. Besides their computational efficiency, the asymptotic methods allow to handle different elementary waves like, e. g., primary reflections and converted waves, independently which simplifies the interpretation of the results. Both approximate methods break down under certain conditions, e. g., in focal or shadow regions. Recent extensions like the Gaussian beam method and the Maslov-Chapman method are able to overcome some of the limitations, thus allowing a broader applicability of the approximate solutions.

The following chapter focuses on ray theory which provides a high frequency solution to the wave equation in terms of the so-called ray series. Usually, the description is restricted to the leading term of this series which is known as zero-order ray theory. Assuming a sufficiently smooth medium, the ray method provides an approximate solution for both the kinematics and dynamics of the wavefield in form of the eikonal and transport equations. Paraxial ray tracing, an extension to conventional ray theory, utilises the quantities of a known ray to approximate rays in its vicinity. The paraxial system can be further extended to the dynamic ray-tracing system which parameterises whole traveltime fields and provides dynamic quantities as, e. g., the geometrical spreading factor.

The following derivations are restricted to the theoretical aspects actually needed in the further considerations. A detailed treatment of the ray method can be found in, e. g., Červený (2001), see also references therein. The presented paraxial ray method mostly follows the lines of Schleicher et al. (2007).

2.1   Elastodynamic wave equation

The basis of the elastodynamic wave equation is the conservation of momentum. Together with a linear relationship between stress and strain, i. e., the generalised Hooke's law, and further linearisations,

we arrive at a second order partial differential equation. The latter relates the temporal derivatives to the spatial derivatives of the particle displacement field, thus allowing to compute this field for given initial and boundary conditions, provided the spatial distribution of the medium parameters is known. Detailed derivations are given in, e. g., Aki and Richards (1980), Lay and Wallace (1995), and Chapman (2004).

Anisotropic inhomogeneous case

In the following, the motion of a selected particle within a solid, linear-elastic body is considered. Using the Lagrangian description of motion in an elastic continuum, its dislocation can be described with respect to the original location $\hat{\mathbf{r}} = (r_1, r_2, r_3)$ of the particle at a reference time t_0. The time-dependent dislocation vector is thus given by $\hat{\mathbf{u}}(\hat{\mathbf{r}}, t)$, the velocity and acceleration of the particle by $\partial \hat{\mathbf{u}}/\partial t$ and $\partial^2 \hat{\mathbf{u}}/\partial t^2$, respectively.

The stress condition at any point $\hat{\mathbf{r}}$ in the medium is described by means of the symmetric stress tensor $\boldsymbol{\tau}(\hat{\mathbf{r}}, t)$. The diagonal elements of the stress tensor τ_{ii} represent normal stresses while the off-diagonal elements $\tau_{ij}, i \neq j$, represent shear stresses. The deformation of the body under stress is specified by means of the strain tensor $\boldsymbol{e}(\hat{\mathbf{r}}, t)$ which is also symmetric.

The spatial variation of the stress tensor τ_{ij} can be related to the time variation of the displacement vector $\hat{\mathbf{u}}$ using the equation of motion:

$$\rho \frac{\partial^2 u_j}{\partial t^2} = f_j + \frac{\partial \tau_{ij}}{\partial r_i} \,. \tag{2.1}$$

Here, $\rho(\hat{\mathbf{r}})$ denotes the density and $\hat{\mathbf{f}}$ is the density of the external body forces.

Under the assumption of a linear-elastic solid, the spatial derivatives of the stress tensor in equation (2.1) can be expressed in terms of the displacement vector using the constitutive relation, a generalisation of Hooke's law:

$$\tau_{ij} = c_{ijkl} e_{kl} \,, \qquad i, j, k, l = (1, 2, 3) \,, \tag{2.2}$$

with

$$e_{kl} = \frac{1}{2} \left(\frac{\partial u_k}{\partial r_l} + \frac{\partial u_l}{\partial r_k} \right) \,. \tag{2.3}$$

The latter only holds for small deformations which allows to neglect higher-oder terms. The 4th order tensor $\boldsymbol{c}(\hat{\mathbf{r}})$ in equation (2.2) is usually called stiffness or elastic tensor, its components c_{ijkl} elastic moduli. Due to the symmetry of the stress and the strain tensor and with the assumption of an adiabatic deformation process, only 21 of the 81 components of the elastic tensor are independent for the most general case of an adiabatic, anisotropic medium.

Rewriting $\partial \tau_{ij}/\partial r_i$ as

$$\frac{\partial \tau_{ij}}{\partial r_i} = \frac{1}{2} \frac{\partial}{\partial r_i} \left(c_{ijkl} \frac{\partial u_k}{\partial r_l} + c_{ijkl} \frac{\partial u_l}{\partial r_k} \right) \tag{2.4a}$$

$$= \frac{\partial}{\partial r_i} \left(c_{ijkl} \frac{\partial u_k}{\partial r_l} \right) \,, \tag{2.4b}$$

and substituting the result in equation (2.1) yields the elastodynamic wave equation for an inhomogeneous anisotropic linear-elastic medium:

$$\rho \frac{\partial^2 u_j}{\partial t^2} - \frac{\partial}{\partial r_i} \left(c_{ijkl} \frac{\partial u_k}{\partial r_l} \right) = f_j \,. \tag{2.5}$$

Isotropic inhomogeneous case

For isotropic media, the number of independent elastic parameters reduces to the two so-called Lamé parameters $\lambda = \lambda(\hat{\mathbf{r}})$ and $\mu = \mu(\hat{\mathbf{r}})$. The latter quantifies the resistance to shear stresses and is usually called shear modulus. The relationship of the Lamé parameters to the elastic tensor is given by

$$c_{ijkl} = \lambda\delta_{ij}\delta_{kl} + \mu\left(\delta_{ik}\delta_{jl} + \delta_{il}\delta_{jk}\right) , \tag{2.6}$$

with the Kronecker symbol δ_{ij} which equals 1 for $i = j$ and 0 for $i \neq j$.

With equation (2.6), the wave equation for inhomogeneous isotropic linear-elastic media can be formulated in vector notation as

$$\rho\frac{\partial^2\hat{\mathbf{u}}}{\partial t^2} - (\lambda + \mu)\hat{\boldsymbol{\nabla}}(\hat{\boldsymbol{\nabla}}\cdot\hat{\mathbf{u}}) - \mu\Delta\hat{\mathbf{u}} - \hat{\boldsymbol{\nabla}}\lambda(\hat{\boldsymbol{\nabla}}\cdot\hat{\mathbf{u}}) - \hat{\boldsymbol{\nabla}}\mu\times(\hat{\boldsymbol{\nabla}}\times\hat{\mathbf{u}}) - 2(\hat{\boldsymbol{\nabla}}\mu\cdot\hat{\boldsymbol{\nabla}})\hat{\mathbf{u}} = \hat{\mathbf{f}} . \tag{2.7}$$

Acoustic case

The elastodynamic wave equation can be further simplified for acoustic media fluids where the shear modulus equals zero. Expressing the displacement $\hat{\mathbf{u}}$ in terms of pressure $p(\hat{\mathbf{r}}, t) = -\lambda\hat{\boldsymbol{\nabla}}\cdot\hat{\mathbf{u}}(\hat{\mathbf{r}}, t)$ and assuming $\hat{\mathbf{f}} = \hat{\mathbf{0}}$, the acoustic wave equation reads

$$\frac{1}{\lambda}\frac{\partial^2 p}{\partial t^2} - \hat{\boldsymbol{\nabla}}\cdot(\frac{1}{\rho}\hat{\boldsymbol{\nabla}}p) = 0 . \tag{2.8}$$

In case of a medium with constant density ρ this equation reduces to the well-known form

$$\frac{1}{c^2}\frac{\partial^2 p}{\partial t^2} - \Delta p = 0 . \tag{2.9}$$

Here, $c = \sqrt{\lambda/\rho}$ denotes the acoustic wave velocity.

2.2 Ray theory

As already mentioned, the elastodynamic wave equation cannot be solved analytically for arbitrary inhomogeneous media. In the homogeneous case, however, analytic solutions can be found for certain initial conditions from which some general properties of seismic waves may be derived. The simplest solution is obtained for time harmonic plane waves, i. e., waves of the type

$$\hat{\mathbf{u}}(\hat{\mathbf{r}}, t) = U\, e^{-i\omega(t-\tau(\hat{\mathbf{r}}))} , \tag{2.10}$$

with U being a vectorial constant (or scalar in the acoustic case), and ω the circular frequency. The eikonal $\tau(\hat{\mathbf{r}})$ is a linear homogeneous function of the coordinates r_i and describes the traveltime of the considered wave. Inserting ansatz (2.10) into the appropriate wave equation for the considered medium yields a linear system of homogeneous equations with, in the most general case of an anisotropic medium, three different non-trivial solutions. These solutions are related to three decoupled plane waves with, in general, different properties. The three eigenvalues of the linear system describe the propagation velocities while the corresponding eigenvectors determine the polarisation directions.

In the isotropic case, the system degenerates: two eigenvalues coincide and the polarisation direction is given by a linear combination of the two corresponding eigenvectors. For the two remaining wave types, one obtains a well defined relation between the direction of polarisation and the direction of wave propagation. The so-called P-wave, a compressional wave, is polarised in the direction of wave propagation. The so-called S-wave with particle displacement in the plane normal to the propagation direction is, in general, elliptically polarised. However, it is quite common to consider two linearly polarised wave types which are mutually orthogonal. One exhibits a purely horizontal polarisation (SH wave), whereas the other also allows a vertical polarisation component (SV wave). The propagation velocities of the P- and S-waves read $v_p = \sqrt{(\lambda + 2\mu)/\rho}$ and $v_s = \sqrt{\mu/\rho}$, respectively. Finally, in the acoustic case only one type of plane wave is observed: the compressional wave which can be described by the scalar pressure.

For inhomogeneous media, the strict separation of the wavefield into independent wave types no longer holds. However, in case of a smooth medium where medium properties do not vary significantly over the length scale of the source wavelet, the high-frequency elastic wavefield is still approximately separable into independent P- and S-wave contributions. The properties of these high-frequency elementary wave types are locally very similar to those of the homogeneous case. At interfaces, i.e., zero-order discontinuities where medium parameters change abruptly, the wave equation cannot be solved across the boundary. Instead, explicit boundary conditions have to be considered. These conditions follow from the assumed type of contact at the interface. In a similar way, free surfaces can be handled.

One commonly applied approach to describe the propagation of high-frequency waves in smooth media is seismic ray theory: each elementary wave is expressed in terms of a so-called ray series, a series in inverse powers of ω in the frequency domain. Usually, only the zero-order term of the series is considered, leading to the so-called zero-order ray theory which is briefly summarised in the following sections.

2.2.1 Eikonal and transport equation

For simplicity, the ray method is demonstrated for the acoustic case using equation (2.8).

The ray ansatz for the derivation of the approximate high-frequency (HF) solution of the wave equation is based on a series expansion of the plane wave solution (2.10). For acoustic media, the scalar ray series reads

$$p(\hat{\mathbf{r}}, t) = e^{-i\omega(t - \tau(\hat{\mathbf{r}}))} \sum_{n=0}^{\infty} (-i\omega)^{-n} P^{(n)}(\hat{\mathbf{r}}), \qquad (2.11)$$

where $P^{(n)}(\hat{\mathbf{r}}), n = 0, 1, 2...$ denotes the amplitude coefficients of the ray series. In the zero-order approximation considered here, only the leading term of equation (2.11) is taken into account, which is given by

$$p(\hat{\mathbf{r}}, t) = P(\hat{\mathbf{r}})\, e^{-i\omega(t - \tau(\hat{\mathbf{r}}))} \qquad \text{with } P = P^{(0)}. \qquad (2.12)$$

Inserting this ansatz into equation (2.8) and sorting the terms with respect to the powers of ω yields

$$-\omega^2 \left[\left(\hat{\boldsymbol{\nabla}} \tau \right)^2 - \frac{\rho}{\lambda} \right] - \frac{i\omega}{P} \left[2\hat{\boldsymbol{\nabla}} P \cdot \hat{\boldsymbol{\nabla}} \tau + P \Delta \tau - \frac{P}{\rho} \hat{\boldsymbol{\nabla}} \rho \cdot \hat{\boldsymbol{\nabla}} \tau \right] + \frac{\rho}{P} \hat{\boldsymbol{\nabla}} \cdot \left(\frac{1}{\rho} \hat{\boldsymbol{\nabla}} P \right) = 0, \qquad (2.13)$$

which has to be satisfied for all frequencies. In general, we cannot expect that terms of different powers of ω cancel each other. Therefore, the terms have to vanish independently.

Setting the coefficients with ω^2 and ω to zero leads to the well-known eikonal equation

$$\left(\hat{\boldsymbol{\nabla}}\tau\right)^2 = \frac{1}{c^2}\,,\tag{2.14}$$

and transport equation

$$2\hat{\boldsymbol{\nabla}}\left(\frac{P}{\sqrt{\rho}}\right)\cdot\hat{\boldsymbol{\nabla}}\tau + \left(\frac{P}{\sqrt{\rho}}\right)\Delta\tau = 0\,,\tag{2.15}$$

which play a fundamental role in the seismic ray theory. The third condition which follows from setting the third term in equation (2.13) to zero can, however, not be satisfied explicitly for general cases. For sufficiently high frequencies, i.e., sufficiently smooth media, it is assumed that this term can be neglected. In fact, it is possible to evaluate the term once the solutions to the eikonal and transport equation are known. In this way, a measure for the applicability of the zero-order ray theory for the specific problem can be obtained.

For isotropic inhomogeneous media, similar derivations can be carried out using a vectorial ray series ansatz. Then, we obtain eikonal and transport equations for both P- and S-wave which basically exhibit the same structure as in the acoustic case:

$$\left(\hat{\boldsymbol{\nabla}}\tau\right)^2 = \frac{1}{v^2}\qquad\text{and}\tag{2.16}$$

$$2\hat{\boldsymbol{\nabla}}\left(\sqrt{\rho v^2}\,A_{P/S}\right)\cdot\hat{\boldsymbol{\nabla}}\tau + \sqrt{\rho\,v^2}\,A_{P/S}\,\Delta\tau = 0\,,\tag{2.17}$$

where v denotes the respective velocity for the P- or S-wave and $A_{P/S}$ the corresponding amplitude coefficient. Here, the amplitude coefficient for the S-wave A_S can be expressed as

$$A_S(\hat{\mathbf{r}}) = B(\hat{\mathbf{r}})\,\hat{\mathbf{e}}_1 + C(\hat{\mathbf{r}})\,\hat{\mathbf{e}}_2\,,\tag{2.18}$$

with $B(\hat{\mathbf{r}})$ and $C(\hat{\mathbf{r}})$ being scalar, complex-valued amplitude functions. In general, the unit vectors $\hat{\mathbf{e}}_1$ and $\hat{\mathbf{e}}_2$ are chosen perpendicular to each other and to the slowness vector of the S-wave. In this case, the components B and C and consequently the corresponding transport equations are coupled.

2.2.2 Solution of the eikonal equation

In the following, we seek a solution to the eikonal equation (2.16) where the symbol v represents the appropriate velocity for the considered medium and wave type, i.e., c, α, or β. Equation (2.16) represents a nonlinear partial differential equation of first order in τ which is a special case of the class of Hamilton-Jacobi equations and can be solved using the method of characteristics. For that purpose, equation (2.16) is expressed in terms of the slowness vector

$$\hat{\mathbf{p}} = \hat{\boldsymbol{\nabla}}\tau\,,\tag{2.19}$$

which is perpendicular to the wavefronts described by $t = \tau$. The eikonal equation can then be expressed by

$$|\hat{\mathbf{p}}|^2 = \frac{1}{v^2}\,.\tag{2.20}$$

Equation (2.20) can also be formulated as a Hamiltonian, i. e., in the form $\mathcal{H}(\hat{\mathbf{r}}, \hat{\mathbf{p}}) = 0$. From the latter, a characteristic system of differential equations of first order can be established, the so-called kinematic ray-tracing system (for derivation, see, e. g., Bleistein, 1984):

$$\frac{d\hat{\mathbf{r}}}{du} = \hat{\mathbf{\nabla}}_p \mathcal{H}, \qquad \frac{d\hat{\mathbf{p}}}{du} = -\hat{\mathbf{\nabla}}\mathcal{H}, \qquad \frac{d\tau}{du} = \hat{\mathbf{p}} \cdot \hat{\mathbf{\nabla}}_p \mathcal{H}, \qquad (2.21)$$

where $\hat{\mathbf{\nabla}}_p$ denotes the gradient with respect to the components of $\hat{\mathbf{p}}$ and u being a monotonously increasing parameter. The solutions of (2.21), i. e., the characteristics, describe space trajectories in the 6D phase space spanned by $\hat{\mathbf{r}}$ and $\hat{\mathbf{p}}$ along which $\mathcal{H}(\hat{\mathbf{r}}, \hat{\mathbf{p}}) = 0$ is satisfied. The projection of such a trajectory into the 3D $\hat{\mathbf{r}}$-space is referred to as ray in seismic literature. The solutions related to $\hat{\mathbf{r}}$ define the characteristic curve as 3D trajectory, while the solutions for $\hat{\mathbf{p}}$ describe the vector change along the ray. These equations are coupled and have to be solved together. The solution for τ can be obtained by an additional integration and describes the change of τ along the characteristics.

The actual form of the Hamiltonian depends on the specified problem, a common choice is $\mathcal{H}(\hat{\mathbf{r}}, \hat{\mathbf{p}}) = |\hat{\mathbf{p}}| - \frac{1}{v}$ and $u = s$, the arclength, leading to:

$$\frac{d\hat{\mathbf{r}}}{ds} = v\hat{\mathbf{p}}, \qquad \frac{d\hat{\mathbf{p}}}{ds} = \hat{\mathbf{\nabla}}\left(\frac{1}{v}\right), \qquad \frac{d\tau}{ds} = \frac{1}{v}. \qquad (2.22)$$

In order to solve the system for a certain ray, its initial position $\hat{\mathbf{r}}_0$ and direction $\hat{\mathbf{p}}_0$ have to be specified. Usually, the kinematic ray tracing system is solved numerically using Runge-Kutta methods.

2.2.3 Solution of the transport equation

With the solution of the eikonal equation, the kinematics along the rays in the medium are known. In order to solve the transport equation along one of these rays, a whole system of rays, a ray field, has to be considered that represents the wavefront $t = \tau(\hat{\mathbf{r}})$ of the considered wave. A unique description of each ray within the ray field is obtained by the transition to so-called ray coordinates. A common choice for the coordinates if a point source is considered are the two take-off angles γ_1 and γ_2 which specify the initial slowness of the ray at the source S and a monotonously increasing parameter γ_3 along the ray, for instance the arclength s or the traveltime τ (see also Figure 2.1). The ray coordinates γ_1, γ_2, and γ_3 form a curvilinear system which provides a valid but not necessarily unique description of each point reached by an arbitrary ray of the field. For these points, the transformation from the ray coordinates $\hat{\mathbf{\gamma}}$ to the global Cartesian coordinates $\hat{\mathbf{r}}$ can be expressed by

$$d\hat{\mathbf{r}} = \hat{\mathbf{Q}}^{(r)} d\hat{\mathbf{\gamma}}, \qquad (2.23)$$

where the elements of the 3×3 transformation matrix $\hat{\mathbf{Q}}^{(r)}$ are given by $Q_{ij} = \partial r_i/\partial \gamma_j$, $i, j = 1, 2, 3$. The corresponding Jacobian of transformation, also denoted as ray Jacobian if $\gamma_3 = s$, reads

$$J = \left| \frac{\partial(r_1, r_2, r_3)}{\partial(\gamma_1, \gamma_2, \gamma_3)} \right| = \left(\frac{\partial \hat{\mathbf{r}}}{\partial \gamma_1} \times \frac{\partial \hat{\mathbf{r}}}{\partial \gamma_2} \right) \cdot \frac{\partial \hat{\mathbf{r}}}{\partial \gamma_3} = \det \hat{\mathbf{Q}}^{(r)}. \qquad (2.24)$$

The ray field is called regular within a region, if the Jacobian is defined and does not vanish at any point of this region. Otherwise, the ray field is called singular.

For the solution of the transport equation certain properties of the Jacobian J have to be considered. In principle, all derivations can be carried out for any arbitrarily chosen ray parameter γ_3. However,
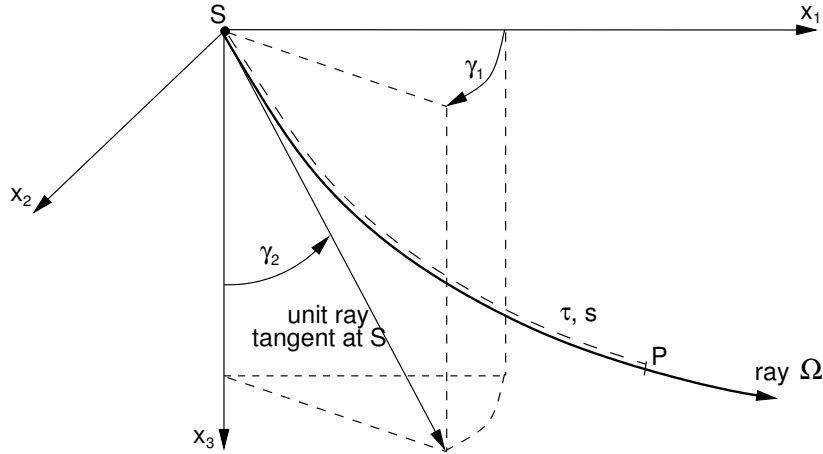
Figure 2.1: For a point source S, the ray-coordinates $\hat{\gamma}$ are usually specified by means of two take-off angles γ_1 and γ_2 at S and a monotonously increasing parameter γ_3 which describes the position along the ray, for instance the traveltime τ or the arclength s.

it is convenient to work with the ray Jacobian, i. e., $\gamma_3 = s$. Introducing the so-called elementary ray tube which is defined by a family of rays whose ray coordinates are within the limits of $(\gamma_1, \gamma_1 + d\gamma_1)$ and $(\gamma_2, \gamma_2 + d\gamma_2)$, the amplitudes of the propagating wave can be directly related to the ray Jacobian J. Geometrically, J represents the cross-sectional area of the elementary ray tube and is, thus, related to the density of the wavefield: small J, i. e., a small cross-sectional area, means high density of rays and, consequently, high amplitudes, whereas high values of J are related to a low ray density and small amplitudes. Furthermore, geometrical considerations allow to express the factor $\Delta\tau$ using the ray Jacobian:

$$\Delta\tau = \frac{1}{J}\frac{d}{ds}\left(\frac{J}{v}\right),\tag{2.25}$$

where v denotes the general velocity. With the help of expression (2.25), the transport equation can now be solved along rays in terms of the ray Jacobian.

We start with the acoustic case (2.15). Along the ray, $\hat{\nabla}\tau$ can be expressed by means of the acoustic velocity c and the unit tangent vector $\hat{\mathbf{t}}$ as $\hat{\nabla}\tau = \hat{\mathbf{t}}/c$. With

$$\hat{\mathbf{t}}\cdot\hat{\nabla}\left(\frac{P}{\sqrt{\rho}}\right) = \frac{d\left(P/\sqrt{\rho}\right)}{ds},\tag{2.26}$$

the transport equation reads

$$\frac{d}{ds}\left(\frac{P}{\sqrt{\rho}}\right) + \frac{c}{2}\frac{P}{\sqrt{\rho}}\Delta\tau = 0.\tag{2.27}$$

Substituting $\Delta\tau$ in equation (2.27) by equation (2.25) yields

$$\frac{d}{ds}\ln\left(P(s)\sqrt{\frac{J(s)}{\rho(s)c(s)}}\right) = 0,\tag{2.28}$$

which is solved for the amplitude $P(s)$. The final solution reads

$$P(s) = C(\gamma_1, \gamma_2)\sqrt{\rho(s)\,c(s)/J(s)},\tag{2.29}$$

17

$C(\gamma_1, \gamma_2)$ being a constant along the ray. The amplitude $P(s)$ can thus be determined from the amplitude $P(s_0)$ at some reference point s_0 via

$$P(s) = \sqrt{\frac{\rho(s)\, c(s)\, J(s_0)}{\rho(s_0)\, c(s_0)\, J(s)}}\, P(s_0) \tag{2.30}$$

if the ray Jacobian J is known. In this equation, the factor $\sqrt{J(s_0)/J(s)}$ describes the amplitude loss caused by geometrical divergence of the propagating wave, the quantity $\mathcal{L} = \sqrt{J(s)}$ is commonly referred to as geometrical spreading factor.

In a similar way, the solution of the respective transport equations for elastic P- and S-waves can be derived. For S-waves, the transport equation is in general coupled, i.e., the amplitude coefficients B and C in equation (2.18) are not independent. A certain choice for the unit vectors $\hat{\mathbf{e}}_1$ and $\hat{\mathbf{e}}_2$, however, leads to a decoupling of the transport equation which then takes the same form as for the P-wave. In this case, the general solution for the elastic amplitude can be expressed as

$$A(s) = \sqrt{\frac{\rho(s)\, v(s)\, J(s_0)}{\rho(s_0)\, v(s_0)\, J(s)}}\, A(s_0), \tag{2.31}$$

where $A(s)$ replaces the amplitude term $A_P(s)$ for P-waves or $B(s)$ and $C(s)$ for S-waves and $v(s)$ the corresponding velocity α or β.

In singular regions, i.e., regions where the Jacobian becomes zero, the description of the amplitudes by means of equations (2.30) and (2.31) breaks down. Such points are called caustics. In general, we distinguish between caustics of first order where the cross section of the ray tube shrinks to a line, and caustics of second order where the cross section is reduced to a point. Mathematically, the first case corresponds to rank $\hat{\mathbf{Q}}^{(r)} = 2$, the second to rank $\hat{\mathbf{Q}}^{(r)} = 1$. In passing through a singular region, the wave phase is subject to a phase shift of $\pi/2$ in case of a first-order caustic and π for a caustic of second order.

In order to account for caustics in the computation of seismic amplitudes, the actually continuous transition of the phase along a ray through a caustic region is approximated in ray theory by a discontinuous phase jump. This can be achieved by incorporating an additional phase term in the definition of the square-root of J:

$$\sqrt{J} = |J|^{\frac{1}{2}}\, e^{-i\frac{\pi}{2}\kappa}. \tag{2.32}$$

Here, the KMAH index κ is increased by one for each caustic of first order passed by the wave and by two for each caustic of second order (for details see Ziolkowski and Deschamps, 1980). The geometrical spreading factor thus becomes $\mathcal{L} = |J|^{\frac{1}{2}}\, e^{-i\frac{\pi}{2}\kappa}$, or if normalised with respect to the velocity v_S and v_G at starting and end point of the ray

$$\overline{\mathcal{L}} = \frac{1}{\sqrt{v_S\, v_G}}\, |J|^{\frac{1}{2}}\, e^{-i\frac{\pi}{2}\kappa}. \tag{2.33}$$

2.2.4 Physical rays

The seismic ray as solution of the eikonal equation is a purely mathematical concept. For a ray Ω connecting a source point S and a receiver R via the reflection point M_R it can be interpreted as
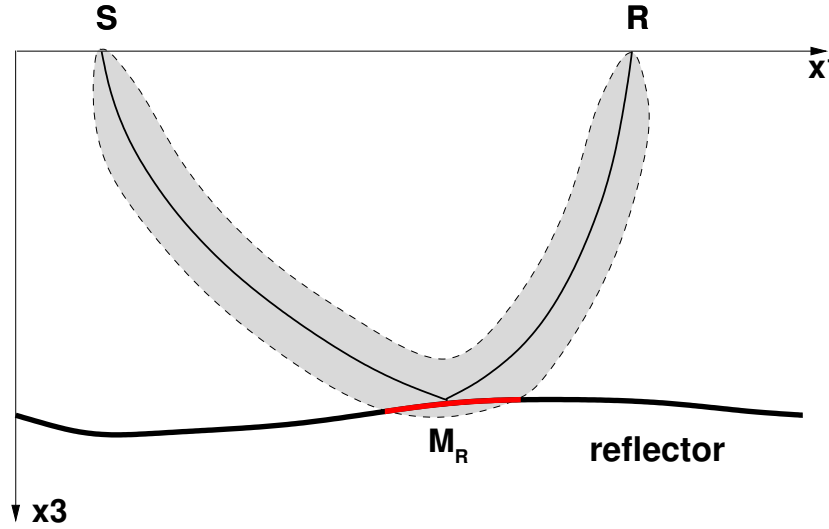
Figure 2.2: Schematic sketch of the Fresnel volume (grey) of a reflected ray $S\,M_R\,R$. The intersection of the Fresnel volume with a reflecting interface defines the interface Fresnel zone (red).

---

the trajectory along which the high-frequency part of the energy of the seismic wave propagates. In reality, the wavefield recorded at R is influenced by the velocity distribution and structure in an entire vicinity of the ray Ω rather than along the exact ray path only. This region which actually affects the wavefield in R is usually referred to as Fresnel volume, sometimes also called physical ray.

The intersection of the Fresnel volume with a reflecting interface defines the so-called interface Fresnel zone which is the natural limit of resolution (see Figure 2.2). Subsurface features smaller than the Fresnel zone cannot be resolved. Obviously, the interface Fresnel zone is frequency-dependent, waves with higher frequency provide a higher spatial resolution. For monochromatic signals with period T, the interface Fresnel zone consists of all points $\overline{M}$ on the interface for which the following inequality holds (Červený and Soares, 1992):

$$\left|\tau(S, M, R) - \tau(S, \overline{M}) - \tau(\overline{M}, R)\right| \leq T/2\,. \tag{2.34}$$

For transient signals, the period T has to be replaced by some measure of the wavelet length τ_ω. A variety of different definitions can be found in Schleicher and Santos (2001). Strictly speaking, equation (2.34) defines the size of the first Fresnel zone. The n-th Fresnel zone can simply be obtained by replacing $T/2$ with $n\,T/2$.

2.3 Dynamic and paraxial ray theory

In the previous section, seismic rays were introduced as characteristics of the HF solution of the elastodynamic wave equation. The kinematic ray-tracing system (2.21) provides the ray trajectory while the amplitude along the ray is related to the ray Jacobian J. In principle, J can be calculated by analysing the elementary ray tube. For that purpose, rays in the close (paraxial) vicinity of the central ray have to be calculated. An efficient solution to this problem is the use of so-called paraxial and dynamic ray-tracing methods.
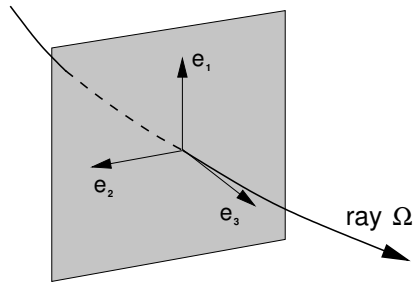
Figure 2.3: The basis vectors e_1, e_2, and e_3 of the ray-centred coordinate system $\hat{\mathbf{q}}$ associated with a ray Ω. The q_3-axis of the system corresponds to a monotonic parameter along the ray, the corresponding basis vector e_3 thus equals the unit tangent to the ray in any point.

For that purpose, the medium velocity is assumed to be adequately approximated by a Taylor expansion of second order with expansion point on the central ray. In this case, the kinematic ray tracing system reduces to the paraxial ray-tracing system which consists of linear differential equations. It describes, up to second order in traveltime, rays in a paraxial vicinity of the central ray in terms of the properties of the central ray. The paraxial ray-tracing system can be further extended to the dynamic ray-tracing system which considers an infinitesimal ray tube around a central ray.

Both, the paraxial and the dynamic ray-tracing systems have the same mathematical form and are closely related: the dynamic ray-tracing yields the derivatives of the phase space coordinates on the central ray with respect to the initial ray parameters, whereas the paraxial system approximates the rays in the vicinity of the central ray.

A particularly convenient representation of the two ray-tracing systems is obtained in ray-centred coordinates associated with the central ray.

2.3.1 Ray-centred coordinates

The ray-centred coordinate system $\hat{\mathbf{q}}$ is a curvilinear system which is associated with a known ray Ω, in the following referred to as central ray. The system is defined in such a way that the coordinate q_3 corresponds to a monotonic parameter along the ray, usually the arclength s. The other two axes are situated in the plane perpendicular to the ray and are chosen such that the vectors form an orthogonal system (see Figure 2.3). The central ray itself is, thus, described by $q_1 = q_2 = 0$.

The region of validity of the ray-centred coordinate system depends on the curvature of the central ray: for a point $\tilde{R}$ in the vicinity of the central ray a unique representation requires that only one plane perpendicular to the central ray can be constructed which contains $\tilde{R}$. Thus, the region of validity is broad for slightly curved rays and narrow in case of rays with large curvature. A detailed description of the ray-centred coordinate system can be found in Popov and Pšenčík (1978).

Note that in contrast to the ray coordinates introduced in context with the solution of the transport equation, the ray-centred coordinates are only associated with the specified reference ray. The transformation from ray to ray-centred coordinates can be expressed in terms of the transformation matrix $\hat{\mathbf{Q}}$, $Q_{ij} = \partial q_i / \partial \gamma_j$. It reads

$$d\hat{\mathbf{q}} = \hat{\mathbf{Q}} \, d\hat{\boldsymbol{\gamma}} \,. \tag{2.35}$$

In the same way, the transformation from ray-centred to global Cartesian coordinates $\hat{\mathbf{x}}$ is given by

$$d\hat{\mathbf{x}} = \hat{\mathbf{H}} \, d\hat{\mathbf{q}}, \tag{2.36}$$

with the transformation matrix $\hat{\mathbf{H}}, H_{ij} = \partial x_i / \partial q_j$.

Using both transformations, the ray Jacobian J can be expressed in ray-centred coordinates by

$$J = \det\left(\hat{\mathbf{H}} \, \hat{\mathbf{Q}}\right) = \det \hat{\mathbf{H}} \, \det \hat{\mathbf{Q}}. \tag{2.37}$$

The definition of J simplifies if the arclength s is chosen as the third axis of the ray and ray-centred coordinate system. Then, the element Q_{33} of the transformation matrix (2.35) equals one. For points on the ray, the determinant of $\hat{\mathbf{Q}}$ thus equals the determinant of its upper-left 2×2 submatrix $\mathbf{Q}$ and $\hat{\mathbf{H}}$ is a rotation matrix with $\det \hat{\mathbf{H}} = 1$. Therefore, the ray Jacobian is entirely determined by the geometrical behaviour of the ray tube and can be calculated from

$$J = \det \mathbf{Q}. \tag{2.38}$$

2.3.2 Ray tracing systems in ray-centred coordinates

The paraxial ray-tracing system is derived from the eikonal equation (2.16) formulated in ray-centred coordinates under the assumption that the medium properties in the vicinity of the central ray can be expressed by a Taylor expansion up to second order in q_1 and q_2. The resulting system of linear equations approximates rays in the paraxial vicinity of a known central ray

$$\frac{dq_i}{ds} = v \, p_i^{(q)}, \qquad \frac{dp_i^{(q)}}{ds} = -\frac{1}{v^2} \, q_j \left. \frac{\partial^2 v}{\partial q_i \partial q_j} \right|_{q_1=q_2=0}, \qquad i,j = 1,2, \tag{2.39}$$

where $\hat{\mathbf{p}}^{(q)}$ symbolises the ray-centred covariant slowness vector. The region of validation of the paraxial ray-tracing system (2.39) depends on the degree of inhomogeneity of the medium.

The dynamic ray-tracing system provides the first partial derivatives of the coordinates $\hat{\mathbf{q}}$ and $\hat{\mathbf{p}}^{(q)}$ with respect to the initial ray parameters. As $\partial/\partial\gamma$ commutes with d/ds, we immediately obtain from equation (2.39)

$$\frac{d}{ds}\left(\frac{\partial q_i}{\partial \gamma}\right) = v \frac{\partial p_i^{(q)}}{\partial \gamma}, \qquad \frac{d}{ds}\left(\frac{\partial p_i^{(q)}}{\partial \gamma}\right) = -\frac{1}{v^2} \frac{\partial q_j}{\partial \gamma} \left. \frac{\partial^2 v}{\partial q_i \partial q_j} \right|_{q_1=q_2=0}, \qquad i,j = 1,2. \tag{2.40}$$

While the paraxial ray-tracing system (2.39) provides approximations of the coordinates $\hat{\mathbf{q}}$ and $\hat{\mathbf{p}}^{(q)}$ along paraxial rays, the dynamic ray-tracing system explicitly determines the partial derivatives $\partial q_i / \partial \gamma$ and $\partial p_i^{(q)} / \partial \gamma$ along the central ray.

A considerably simpler form of equation (2.40) is obtained if an elementary ray tube specified by parameters γ_1 and γ_2 is considered. The dynamic ray-tracing system then reads

$$\frac{d\mathbf{Q}}{ds} = v\mathbf{P}, \qquad \frac{d\mathbf{P}}{ds} = -\frac{1}{v^2} \, \mathbf{VQ}, \tag{2.41}$$

where $\mathbf{V}$ denotes the matrix of second derivatives of v with respect to q_i along the central ray, $\mathbf{Q}$ is the upper-left 2×2 submatrix of the transformation matrix defined in (2.35) and $\mathbf{P}$ is given by

$P_{ij} = \partial p_i^{(q)}/\partial \gamma_j, i, j = 1, 2$. The system (2.41) consists of four linear ordinary differential equations of first order. Its solution for arbitrary initial conditions can be constructed once two linearly independent solutions are known. Here we shall consider the so-called plane wave solutions $\mathbf{Q}_1$ and $\mathbf{P}_1$ and the point source solutions $\mathbf{Q}_2$ and $\mathbf{P}_2$ which are obtained from the initial conditions $\mathbf{Q}(S) = \mathbf{I}, \mathbf{P}(S) = \mathbf{0}$ and $\mathbf{Q}(S) = \mathbf{0}, \mathbf{P}(S) = \mathbf{I}$, respectively. Here, $\mathbf{I}$ and $\mathbf{0}$ denote the 2×2 identity and zero matrix and S is the source point. Using these two solutions, the fundamental 4×4 matrix $\hat{\bar{\mathbf{\Pi}}}$ of the dynamic ray-tracing system which is usually referred to as ray propagator matrix can be expressed as

$$\hat{\bar{\mathbf{\Pi}}}(R, S) = \begin{pmatrix} \mathbf{Q}_1 & \mathbf{Q}_2 \\ \mathbf{P}_1 & \mathbf{P}_2 \end{pmatrix}. \tag{2.42}$$

Once the ray propagator matrix is known for a specified ray connecting a source point S and a receiver R, the solution of the dynamic ray-tracing system can be determined for any initial condition by multiplying $\hat{\bar{\mathbf{\Pi}}}$ with the matrix of the initial conditions. Thus, the general solution to the paraxial ray tracing system (2.39) can be expressed by

$$\begin{pmatrix} \mathbf{q}(R) \\ \mathbf{p}^{(q)}(R) \end{pmatrix} = \hat{\bar{\mathbf{\Pi}}}(R, S) \begin{pmatrix} \mathbf{q}(S) \\ \mathbf{p}^{(q)}(S) \end{pmatrix}. \tag{2.43}$$

Note that the matrix $\hat{\bar{\mathbf{\Pi}}}$ is symplectic and can be chained along the central ray by simple multiplication.

With the knowledge of $\hat{\bar{\mathbf{\Pi}}}$, dynamic parameters along the ray can be calculated. An important property for the handling of dynamic effects in seismic applications is the normalised point source geometrical spreading $\tilde{\mathcal{L}}$ which is given by

$$\tilde{\mathcal{L}} = \frac{1}{\sqrt{v_S \, v_R}} |\mathbf{Q}_2|^{\frac{1}{2}} \, e^{-i\frac{\pi}{2}\kappa}. \tag{2.44}$$

2.3.3 Ray tracing systems in local Cartesian coordinates

An alternative form of expression (2.43) was introduced by Bortfeld (1989). Here, the ray-tracing system is given in local Cartesian coordinates associated with the surfaces containing the starting and end points of the paraxial rays. These surfaces, usually referred to as anterior (for the source) and posterior (in case of the receiver) surface, may be arbitrarily oriented and curved. In the following, a central ray emanating from a source point S on the anterior surface and reaching the posterior surface in receiver point R is considered. The two local Cartesian coordinate systems (x_{S1}, x_{S2}, x_{S3}) and (x_{R1}, x_{R2}, x_{R3}) are centred at the source or receiver point and constructed such that their $x_1 - x_2$ plane is situated within a plane $\Sigma_{S/R}$ tangent to the considered surface. The x_3–axis of the local system is normal to $\Sigma_{S/R}$ and oriented such that it forms an acute angle with the slowness vector of the central ray. The first two components of both systems, (x_{S1}, x_{S2}) and (x_{R1}, x_{R2}), define local 2D Cartesian coordinate systems within the planes Σ_S and Σ_R, respectively.

The central ray is fully defined by its position vectors $\hat{\mathbf{x}}_{S0}$ at S and $\hat{\mathbf{x}}_{R0}$ at R and the slowness vectors $\hat{\mathbf{p}}_S$ and $\hat{\mathbf{p}}_R$. A paraxial ray connecting point $\overline{S}$ on the anterior and $\overline{R}$ on the posterior surface is parameterised by its dislocations $\hat{\mathbf{x}}_S$ and $\hat{\mathbf{x}}_R$ measured with respect to S and R and the deviation of its slowness vectors $\hat{\bar{\mathbf{p}}}_S$ and $\hat{\bar{\mathbf{p}}}_R$ which are defined at $\overline{S}$ and $\overline{R}$ with respect to the slowness vectors of the central ray.

The three–dimensional quantities $\hat{\mathbf{x}}_S$, $\hat{\mathbf{p}}_S$, and $\hat{\bar{\mathbf{p}}}_S$ describing the central and the paraxial ray can be depicted in the local system (x_{S1}, x_{S2}) by 2–component representations that provide a fully suitable
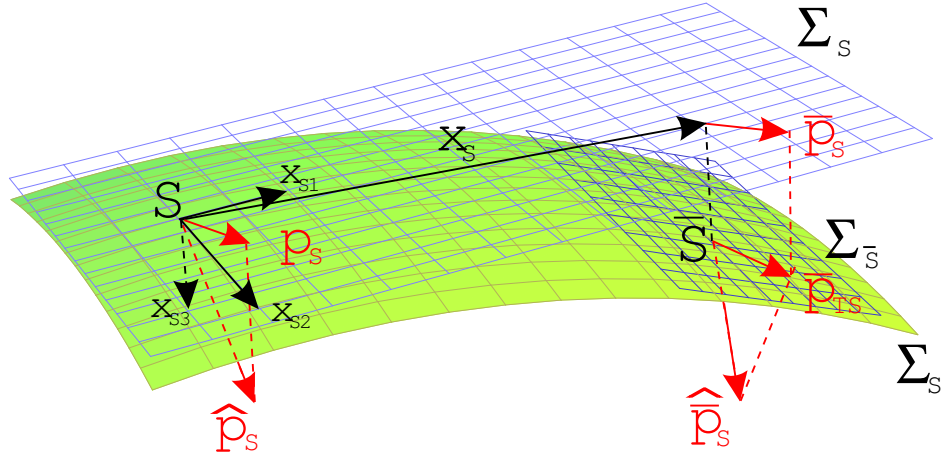
Figure 2.4: Construction of the slowness vector projections $\mathbf{p}_S$ and $\overline{\mathbf{p}}_S$. The initial slowness of the central ray $\hat{\mathbf{p}}_S$ is projected along the plane's normal onto Σ_S. The initial slowness of the paraxial ray $\hat{\overline{\mathbf{p}}}_S$ is firstly projected onto the plane $\Sigma_{\overline{S}}$ tangent to the anterior surface at $\overline{S}$. Thereafter, the resulting vector $\overline{\mathbf{p}}_{TS}$ is projected onto the plane Σ_S.

description of both rays. The 2D vectors $\mathbf{x}_S$ and $\mathbf{p}_S$ are obtained by performing a projection of the vectors $\hat{\mathbf{x}}_S$ and $\hat{\mathbf{p}}_S$ along the plane's normal onto Σ_S. To find the 2D representation of $\hat{\overline{\mathbf{p}}}_S$, two cascaded projections have to be performed. For this purpose, an additional plane $\Sigma_{\overline{S}}$ tangent to the anterior surface at $\overline{S}$ has to be constructed. The projection of $\hat{\overline{\mathbf{p}}}_S$ into the plane $\Sigma_{\overline{S}}$ yields $\overline{\mathbf{p}}_{TS}$, which is then projected into the plane Σ_S resulting in the searched–for vector $\overline{\mathbf{p}}_S$ (see Figure 2.4). Knowing the anterior surface and the velocity v_S at the source allows the reconstruction of the 3D quantities from their 2D projections. The same considerations hold for the quantities at the receivers R and $\overline{R}$, respectively.

The parameters characterising the paraxial ray are its projected displacement vector and the deviation of its projected slowness vector from the projected slowness vector of the central ray. By means of the paraxial ray-tracing system (2.43) expressed in local Cartesian coordinates, a linear relationship can be established which describes how these quantities change as a result of wave propagation in the vicinity of the central ray (Bortfeld, 1989):

$$\begin{pmatrix} \mathbf{x}(R) \\ \overline{\mathbf{p}}_{(R)} - \mathbf{p}_{(R)} \end{pmatrix} = \hat{\hat{\mathbf{T}}} \begin{pmatrix} \mathbf{x}(S) \\ \overline{\mathbf{p}}_{(S)} - \mathbf{p}_{(S)} \end{pmatrix}, \tag{2.45}$$

with the 4×4 surface-to-surface propagator matrix $\hat{\hat{\mathbf{T}}}$ given by

$$\hat{\hat{\mathbf{T}}} = \begin{pmatrix} \mathbf{A} & \mathbf{B} \\ \mathbf{C} & \mathbf{D} \end{pmatrix}. \tag{2.46}$$

The 2×2 submatrices $\mathbf{A}, \mathbf{B}, \mathbf{C}$, and $\mathbf{D}$ characterise the central ray and allow to derive dynamic properties of the wavefield, e. g., geometrical spreading: in analogy to equation (2.44), the normalised point source geometrical spreading can be written as function of the submatrix $\mathbf{B}$:

$$\tilde{\mathcal{L}} = \sqrt{\frac{\cos \theta_S \cos \theta_R}{v_S \, v_G}} \, |\mathbf{B}|^{\frac{1}{2}} \, e^{-i\frac{\pi}{2}\kappa}. \tag{2.47}$$

23

Here, θ_S and θ_R denote the ray take-off and emergence angle of the central ray measured versus the normal of the considered surface.

A thorough description of the surface-to-surface ray propagator matrix $\hat{\mathbf{T}}$ and its relation to the ray propagator matrix $\hat{\mathbf{\Pi}}$ can be found in Hubral et al. (1992a).

2.3.4 Paraxial traveltimes

From equation (2.46), two relationships describing $\mathbf{p}_S$ and $\mathbf{p}_R$ can be established which lead to a second-order traveltime approximation for the paraxial ray.

Using Hamilton's equation for two point ray–tracing (see Bortfeld, 1989; Schleicher et al., 1993), the traveltime difference between the central ray $S R$ and the paraxial ray $\overline{S R}$ can be expressed as

$$d\tau = \tau(\overline{S}, \overline{R}) - \tau(S, R) = \hat{\overline{\mathbf{p}}}_R \cdot \hat{\mathbf{x}}_R - \hat{\overline{\mathbf{p}}}_S \cdot \hat{\mathbf{x}}_S \ . \tag{2.48}$$

The sign in equation (2.48) is chosen such that displacing $\overline{S}$ in ray direction leads to a decrease of the traveltime, whereas the traveltime is increased if $\overline{R}$ is shifted in ray direction. As the dot product $\hat{\overline{\mathbf{p}}}_I \cdot \hat{\mathbf{x}}_I$, $I = S, R$ vanishes if the vectors are perpendicular (which states that the traveltime derivative vanishes in vertical direction to the ray), equation (2.48) can be understood as an alternative formulation of Fermat's principle.

In order to use the paraxial-ray formalism, the 2D projections of the dislocation and slowness vectors are required. As shown by Bortfeld (1989), the products of the third components are already of second order and may therefore be neglected in paraxial approximation. Hence, rewriting Hamilton's equation as a function of the 2D projection vectors yields

$$d\tau = \overline{\mathbf{p}}_R \cdot \mathbf{x}_R - \overline{\mathbf{p}}_S \cdot \mathbf{x}_S \ , \tag{2.49}$$

where $\overline{\mathbf{p}}_R$ and $\overline{\mathbf{p}}_S$ can be expressed according to equation (2.46) by

$$\overline{\mathbf{p}}_S = \mathbf{p}_S + \mathbf{B}^{-1} \mathbf{x}_R - \mathbf{B}^{-1} \mathbf{A} \mathbf{x}_S \ , \tag{2.50a}$$

$$\overline{\mathbf{p}}_R = \mathbf{p}_R + \mathbf{C} \mathbf{x}_S + \mathbf{D} \mathbf{B}^{-1} \mathbf{x}_R - \mathbf{D} \mathbf{B}^{-1} \mathbf{A} \mathbf{x}_S \ . \tag{2.50b}$$

Inserting equation (2.50) into equation (2.49) and subsequent integration yields the parabolic approximation of the traveltime along the ray $\overline{S R}$:

$$\tau_{\text{par}}(\mathbf{x}_S, \mathbf{x}_R) = \tau_0 + \mathbf{p}_R \cdot \mathbf{x}_R - \mathbf{p}_S \cdot \mathbf{x}_S \tag{2.51}$$
$$-\mathbf{x}_S \cdot \mathbf{B}^{-1} \mathbf{x}_R + \frac{1}{2} \mathbf{x}_S \cdot \mathbf{B}^{-1} \mathbf{A} \mathbf{x}_S + \frac{1}{2} \mathbf{x}_R \cdot \mathbf{D} \mathbf{B}^{-1} \mathbf{x}_R \ ,$$

with τ_0 being the traveltime along the central ray. The last step uses the symplecticity property of the matrix $\hat{\mathbf{T}}$ which states that $\hat{\mathbf{T}} \hat{\mathbf{T}}^{-1} = \hat{\mathbf{I}}$ and $\hat{\mathbf{T}}^{-1} \hat{\mathbf{T}} = \hat{\mathbf{I}}$, $\hat{\mathbf{T}}^{-1}$ being the inverse of $\hat{\mathbf{T}}$ and $\hat{\mathbf{I}}$ the 4×4 identity matrix.

The parabolic traveltime approximation can be interpreted as the second-order Taylor expansion of the exact two-point traveltime between $\overline{S}$ and $\overline{R}$, i. e., equation (2.51) can be expressed in terms of traveltime derivatives of first and second order with respect to the displacement vectors $\mathbf{x}_S$ and $\mathbf{x}_R$. In order to connect both representations of the traveltime approximation, the slowness vectors are

expressed by means of equation (2.19) and the submatrices of $\hat{\hat{\mathbf{T}}}$ are related to the Hessian matrices $\mathbf{N}_S^R$, $\mathbf{N}_R^S$, and $\mathbf{N}_{SR}$ by

$$\mathbf{N}_S^R = \left(\frac{\partial^2 \tau}{\partial x_{Si} \partial x_{Sj}}\right)_{i,j=1,2} = \mathbf{B}^{-1}\mathbf{A}, \tag{2.52a}$$

$$\mathbf{N}_R^S = \left(\frac{\partial^2 \tau}{\partial x_{Ri} \partial x_{Rj}}\right)_{i,j=1,2} = \mathbf{D}\mathbf{B}^{-1}, \tag{2.52b}$$

$$\mathbf{N}_{SR} = \left(\frac{\partial^2 \tau}{\partial x_{Si} \partial x_{Rj}}\right)_{i,j=1,2} = \mathbf{B}^{-1}. \tag{2.52c}$$

Here, the subscript S and R means derivative with respect to shot and receiver coordinate while the superscript S and R stands for constant shot and receiver coordinate. The relationships (2.52) follow from taking the respective derivative of equation (2.51). Note that the matrices $\mathbf{N}_S^R$ and $\mathbf{N}_R^S$ are symmetric whereas $\mathbf{N}_{SR}$ is not.

The resulting parabolic traveltime expansion thus reads

$$\begin{aligned} \tau_{\text{par}}(\mathbf{x}_S, \mathbf{x}_R) = {} & \tau_0 + \mathbf{p}_R \cdot \mathbf{x}_R - \mathbf{p}_S \cdot \mathbf{x}_S \\ & -\mathbf{x}_S \cdot \mathbf{N}_{SR}\, \mathbf{x}_R + \frac{1}{2}\mathbf{x}_S \cdot \mathbf{N}_S^R\, \mathbf{x}_S + \frac{1}{2}\mathbf{x}_R \cdot \mathbf{N}_R^S\, \mathbf{x}_R. \end{aligned} \tag{2.53}$$

Originally, Bortfeld (1989) derived equation (2.51) for models consisting of homogeneous layers separated by curved interfaces. However, the traveltime approximation is equally valid for laterally inhomogeneous media (Hubral et al., 1992a). Nevertheless, equation (2.51) remains an approximation of the true traveltime even for simple media. The frequently used hyperbolic traveltime approximation is exact for a single horizontal or dipping reflector with homogeneous overburden. It can be obtained by squaring equation (2.51) and retaining only terms up to second order in $\mathbf{x}_S$ and $\mathbf{x}_R$:

$$\begin{aligned} \tau_{\text{hyp}}^2(\mathbf{x}_S, \mathbf{x}_R) = {} & (\tau_0 + \mathbf{p}_R \cdot \mathbf{x}_R - \mathbf{p}_S \cdot \mathbf{x}_S)^2 \\ & + \tau_0\left(-2\mathbf{x}_S \cdot \mathbf{B}^{-1}\,\mathbf{x}_R + \mathbf{x}_S \cdot \mathbf{B}^{-1}\mathbf{A}\,\mathbf{x}_S + \mathbf{x}_R \cdot \mathbf{D}\,\mathbf{B}^{-1}\,\mathbf{x}_R\right). \end{aligned} \tag{2.54}$$

Of course, equation (2.54) can also be expressed in terms of traveltime derivatives:

$$\begin{aligned} \tau_{\text{hyp}}^2(\mathbf{x}_S, \mathbf{x}_R) = {} & (\tau_0 + \mathbf{p}_R \cdot \mathbf{x}_R - \mathbf{p}_S \cdot \mathbf{x}_S)^2 \\ & + \tau_0\left(-2\mathbf{x}_S \cdot \mathbf{N}_{SR}\,\mathbf{x}_R + \mathbf{x}_S \cdot \mathbf{N}_S^R\,\mathbf{x}_S + \mathbf{x}_R \cdot \mathbf{N}_R^S\,\mathbf{x}_R\right). \end{aligned} \tag{2.55}$$

For simple layered media, the hyperbolic traveltime formula showed to better describe near-vertical reflections (Ursin, 1982). However, in general the accuracy of the approximations depends on the model.

2.3.5 Paraxial approximation of the Fresnel zone

Another property of the seismic wavefield which can be estimated from the surface-to-surface propagator matrix is the interface Fresnel zone introduced in Section 2.2.4. Here, the fact is used that the propagator matrix of the ray SMR can be decomposed into the surface-to-surface propagator matrices of the single ray segments: $\hat{\hat{\mathbf{T}}} = \hat{\hat{\mathbf{T}}}_2(MR)\,\hat{\hat{\mathbf{T}}}_1(SM)$. This so-called chain rule is a fundamental property

of the propagator matrix (for details see Hubral et al., 1992b). In a similar way, the submatrices of the total-ray propagator matrix $\hat{\hat{\mathbf{T}}}$ can be expressed in terms of the submatrices of the propagator matrices for the ray segments.

In order to find an approximation of the Fresnel zone, the traveltimes of the two ray branches $(S, \overline{M})$ and $(\overline{M}, R)$ considered in equation (2.34) are calculated by means of paraxial ray tracing. Taking into account that the same source and receiver point is considered for the central and paraxial ray, one immediately obtains from equation (2.51)

$$\tau(S, \overline{M}) = \tau(S, M) + \mathbf{p}_M \cdot \mathbf{x}_M + \frac{1}{2}\mathbf{x}_M \cdot \mathbf{D}_1 \, \mathbf{B}_1^{-1} \, \mathbf{x}_M \,, \tag{2.56a}$$

$$\tau(\overline{M}, R) = \tau(M, R) - \mathbf{p}_M \cdot \mathbf{x}_M + \frac{1}{2}\mathbf{x}_M \cdot \mathbf{B}_2^{-1} \, \mathbf{A}_2 \, \mathbf{x}_M \,. \tag{2.56b}$$

Here, the $\mathbf{x}_M$ and $\mathbf{p}_M$ denote the 2D representations of the dislocation vector from $\overline{M}$ to M and the slowness of the central ray in the local Cartesian coordinate system associated with the interface at M. The submatrices of $\hat{\hat{\mathbf{T}}}_1$ and $\hat{\hat{\mathbf{T}}}_2$ are denoted with the respective subscript. Inserting equations (2.56) into the definition of the interface Fresnel zone (2.34) yields

$$|\mathbf{x}_M \cdot \mathbf{H}_F \mathbf{x}_M| \leq \tau_\omega \,, \tag{2.57}$$

with the Fresnel zone matrix $\mathbf{H}_F$. The latter can be expressed in terms of the submatrices of $\hat{\hat{\mathbf{T}}}_1$ and $\hat{\hat{\mathbf{T}}}_2$ by

$$\mathbf{H}_F = \mathbf{D}_1 \, \mathbf{B}_1^{-1} + \mathbf{B}_2^{-1}\mathbf{A}_2 \; = \mathbf{B}_2^{-1}\mathbf{B} \, \mathbf{B}_1^{-1}. \tag{2.58}$$

Equation (2.57) defines an ellipse in the plane tangent to the interface at M which approximates the exact Fresnel zone given by equation (2.34).

Fresnel volumes and zones play an important role in seismic imaging, in particular concerning investigations on the spatial resolution of seismic methods (Sheriff and Geldart, 1982). For the limited-aperture Kirchhoff migration introduced in Chapter 6, the projection of the interface Fresnel zone onto the measurement surface is required as it directly provides the part of the seismic data that actually contributes to the reflection at M_R. The concept of this so-called projected Fresnel zone was introduced by Hubral et al. (1993) for normal rays. Parameterised in terms of the midpoint vector $\mathbf{m}$, the projected Fresnel zone reads:

$$|(\mathbf{m} - \mathbf{m}_0) \cdot \mathbf{H}_P \, (\mathbf{m} - \mathbf{m}_0)| \leq \tau_\omega \,, \tag{2.59}$$

where $\mathbf{m}_0$ is the midpoint vector describing the central ray. The projected Fresnel zone matrix $\mathbf{H}_P$ is given in paraxial approximation by $\mathbf{H}_P = 4\mathbf{B}^{-1}$. Similar to the interface Fresnel zone in Section 2.2.4, equation (2.59) defines an ellipse in the (m_1, m_2)-plane in the time domain.

An extension of the concept to finite offset rays was given by Schleicher et al. (1997).

2.4 Summary

In this chapter, the elastodynamic wave equation and its simplifications for isotropic and acoustic media as the most fundamental equations in context of seismic imaging have been presented. By means of zero-order ray theory, an asymptotic high-frequency solution to the wave equation in terms of seismic rays has been obtained that is suited to describe wave propagation in smoothly varying

inhomogeneous media. Two fundamental equations, the so-called eikonal equation that provides the kinematic ray-tracing system and the transport equation, from which the amplitudes can be calculated, form the basis of seismic ray theory. Two extensions of seismic ray theory, dynamic and paraxial ray-tracing, have been described which find a broad application in seismic modelling and inversion problems.

Chapter 3

Common-Reflection-Surface Stack

Stacking procedures like the frequently applied NMO/DMO/stack sequence form a central part of the seismic processing workflow. In these processes, the redundancy of the multicoverage field data is used to determine so-called stacking parameters which allow to correct for the influence of the measurement geometry on the prestack data. The summation of these moveout-corrected traces provides a simulated ZO section with improved S/N ratio which gives a first impression of the structures in the subsurface and may enter into a subsequent poststack time or depth migration. Conventional stacking techniques like, for instance the NMO/DMO/stack sequence, provide only a single stacking parameter. This parameter, called stacking velocity, is interpreted as an integral velocity of the overburden of the reflection point. Furthermore, the stacking velocities are usually determined for selected locations and then interpolated to the complete target area.

In recent years, the Common-Reflection-Surface (CRS) stack has been established as a powerful alternative to conventional stacking procedures. Based on a second-order traveltime expansion, the CRS stack can be seen as a generalised high-density stacking velocity analysis tool. This means that, in contrast to conventional stacking, the CRS stacking operator spatially extends over several CMP gathers and approximates the reflection response of a whole reflector segment. In this way, an increased number of traces contribute to the stack which leads to an improved S/N ratio in the simulated ZO section. At the same time, a whole set of stacking parameters, the so-called kinematic wavefield attributes, is obtained for each simulated ZO sample. In this case, no interpolation of these parameters is required as far as stacking itself is concerned.

Originally, the CRS stack was implemented as highly automated imaging process for the simulation of ZO sections in 2D (e. g., Hubral et al., 1998; Müller, 1998) and 3D (e. g., Müller, 2003; Bergler, 2004) from data with low S/N ratio. At this stage, the wavefield attributes were regarded as a pure by-product of the stacking process despite the additional information they carry. Meanwhile, the focus has shifted as the attributes find a broad application in subsequent processing steps among which the tomographic velocity model determination by Duveneck (2004) is the most prominent one. Further applications of the CRS attributes include Dix-type inversion schemes (Müller, 2005), automatic approximative time migration without velocity model (Mann et al., 2000), residual static corrections (Koglin and Ewig, 2003), and minimum-aperture migration (Jäger, 2005b). CRS stack, tomographic velocity model determination, and true-amplitude Kirchhoff migration have been combined to set up a consistent CRS-based imaging workflow from the prestack data to the depth-migrated image (Hertweck et al., 2003b).

In this chapter, the CRS technique will be shortly reviewed. Special attention is paid to the reliable determination and preconditioning of the attributes for the subsequent processes.

3.1 The CRS stacking operator

The general idea of the CRS technique is to describe a reflection event in the vicinity of a ZO sample by means of a second-order traveltime approximation similar to equation (2.53) or (2.55). A particularly convenient form of the CRS operator is obtained in midpoint $\mathbf{m}$ and half-offset $\mathbf{h}$ coordinates. These coordinates do not only provide a simple mathematical (and technical) representation of the operator, but also allow to interpret the stacking parameter geometrically, namely in terms of wavefront properties.

Using an entire stacking surface rather than a trajectory (in 2D) in the time-midpoint-half-offset space implies that the considered reflection events are continuous over several neighbouring midpoint gathers. This does not only lead to a stabilisation in the determination of the stacking parameters but also overcomes the problem that a CMP gather may contain information from more than one reflection point in depth. In conventional processing, an additional dip-moveout correction is required to transform the CMP gathers to true CRP gathers which provide dip-corrected stacking velocities. The CRS technique, however, does not require an additional DMO correction. The spatial stacking operator inherently accounts for the reflection point dispersal, i. e., it can be assumed that at least the main part of the CRP trajectory belonging to a specific ZO sample lies within the corresponding stacking surface. In Figure 3.1a), the CRS stacking operator is depicted for a simple 2D model. Figure 3.1b) shows the deviation of the CRP trajectory from the CMP gather for a non-horizontal reflector.

The subsequent considerations are based on the hyperbolic traveltime representation only since it is most frequently used in practical applications. Similar results can be derived for the parabolic operator (see, e. g., Müller, 2003; Bergler, 2004).

3.1.1 Traveltime approximation in midpoint and half-offset coordinates

In the following, a planar measurement surface which coincides with the (x, y)-plane of the general Cartesian coordinate system is considered. Shots and receivers are both located on the measurement surface, i. e., the anterior and posterior surfaces coincide. Therefore, each point on the measurement surface is fully described by a 2D vector. Given a source and a receiver with coordinates $\mathbf{r}_S$ and $\mathbf{r}_R$, respectively, midpoint and half-offset coordinates are provided by the relations

$$\mathbf{m} = \frac{1}{2} \left(\mathbf{r}_S + \mathbf{r}_R \right) , \qquad \mathbf{h} = \frac{1}{2} \left(\mathbf{r}_S - \mathbf{r}_R \right) . \tag{3.1}$$

For displacement vectors like, e. g., $\mathbf{x}_S$ and $\mathbf{x}_R$ used in the traveltime approximation (2.55), equations (3.1) can be extended to midpoint and half-offset displacement vectors $\Delta\mathbf{m}$ and $\Delta\mathbf{h}$:

$$\Delta\mathbf{m} = \mathbf{m} - \mathbf{m}_0 = \frac{1}{2} \left(\mathbf{x}_S + \mathbf{x}_R \right) , \qquad \Delta\mathbf{h} = \mathbf{h} - \mathbf{h}_0 = \frac{1}{2} \left(\mathbf{x}_S - \mathbf{x}_R \right) , \tag{3.2}$$

where $\mathbf{m}_0$ and $\mathbf{h}_0$ refer to the central ray. Solving these relations for $\mathbf{x}_S$ and $\mathbf{x}_R$ and inserting them into equation (2.55) yields the traveltime approximation in midpoint and half-offset coordinates:

$$
\begin{aligned}
\tau_{\text{hyp}}^2(\Delta\mathbf{m}, \Delta\mathbf{h}) \;=\; & \left(\tau_0 + (\mathbf{p}_R - \mathbf{p}_S) \cdot \Delta\mathbf{m} + (\mathbf{p}_R + \mathbf{p}_S) \cdot \Delta\mathbf{h} \right)^2 \\
& + \tau_0 \left(\Delta\mathbf{m} \cdot \mathbf{M}_M^H \Delta\mathbf{m} + 2 \, \Delta\mathbf{m} \cdot \mathbf{M}_{MH} \Delta\mathbf{h} + \Delta\mathbf{h} \cdot \mathbf{M}_H^M \Delta\mathbf{h} \right) ,
\end{aligned} \tag{3.3}
$$
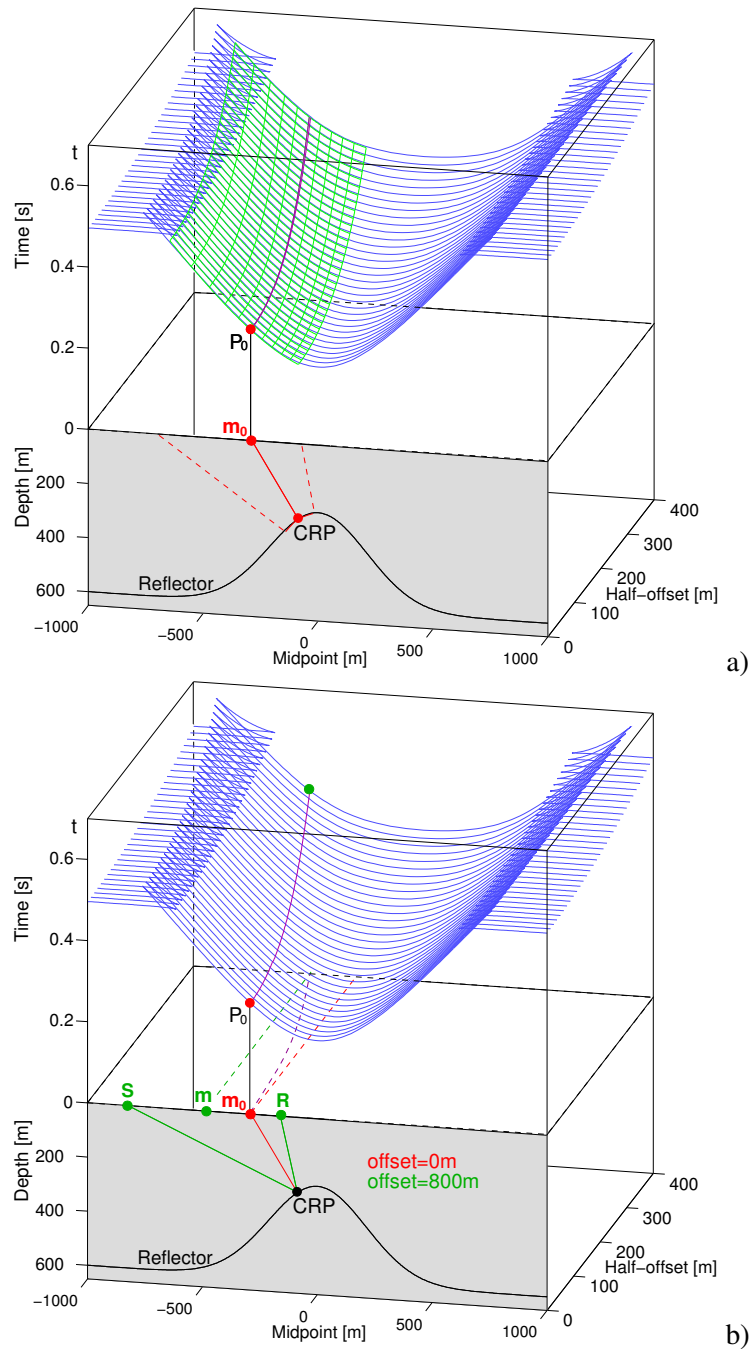
Figure 3.1: CRS stacking operator and CRP trajectory in the time-midpoint-offset volume. The blue curves in the upper part of the pictures represent reflection traveltime curves for fixed source-receiver offsets for the dome-like reflector in the lower part. (a) The green lines indicate the CRS stacking operator for the ZO sample P_0 which approximates the reflection response of the red reflector segment around the Common-Reflection-Point (here set up by means of neighbouring CRP trajectories). (b) The CRP trajectory (purple) connects all points in the time-midpoint-offset volume which belong to a common reflection point in depth. For non-horizontal reflectors or inhomogeneous overburden, the CRP trajectory deviates from the CMP gather.

with $\tau_0 = \tau(\mathbf{m}_0, \mathbf{h}_0)$ and

$$\mathbf{M}_\mathrm{M}^\mathrm{H} = \left(\frac{\partial^2 \tau}{\partial \Delta m_i \partial \Delta m_j}\right)_{i,j=1,2} = \mathbf{N}_\mathrm{S}^\mathrm{R} + \mathbf{N}_\mathrm{R}^\mathrm{S} + \mathbf{N}_\mathrm{SR} + \mathbf{N}_\mathrm{SR}^\mathrm{T}, \tag{3.4a}$$

$$\mathbf{M}_\mathrm{H}^\mathrm{M} = \left(\frac{\partial^2 \tau}{\partial \Delta h_i \partial \Delta h_j}\right)_{i,j=1,2} = \mathbf{N}_\mathrm{S}^\mathrm{R} + \mathbf{N}_\mathrm{R}^\mathrm{S} - \mathbf{N}_\mathrm{SR} - \mathbf{N}_\mathrm{SR}^\mathrm{T}, \tag{3.4b}$$

$$\mathbf{M}_\mathrm{MH} = \left(\frac{\partial^2 \tau}{\partial \Delta m_i \partial \Delta h_j}\right)_{i,j=1,2} = -\mathbf{N}_\mathrm{S}^\mathrm{R} + \mathbf{N}_\mathrm{R}^\mathrm{S} + \mathbf{N}_\mathrm{SR} - \mathbf{N}_\mathrm{SR}^\mathrm{T}. \tag{3.4c}$$

All derivatives are defined at the surface at $(\mathbf{m_0}, \mathbf{h_0})$. Equation (3.3) defines a finite-offset stacking operator in midpoint and half-offset coordinates with a total of 14 independent parameters (note that the matrices $\mathbf{M}_\mathrm{M}^\mathrm{H}$ and $\mathbf{M}_\mathrm{H}^\mathrm{M}$ are symmetric while $\mathbf{M}_\mathrm{MH}$ is not).

In order to find the corresponding zero-offset stacking operator, we consider normal central rays only, i. e., rays which are normal to the reflector in the so-called normal-incidence (NIP) point. For these rays, the up- and down-going ray paths coincide, i. e., $\mathbf{h}_0 = \mathbf{0}$ and $\Delta \mathbf{h} = \mathbf{h}$. Consequently, the following relations hold for the derivatives with respect to $\mathbf{h}$:

$$\left.\frac{\partial \tau}{\partial \mathbf{h}}\right|_{\mathbf{h}=0} = \mathbf{0}, \tag{3.5a}$$

$$\left(\frac{\partial^2 \tau}{\partial \Delta \mathbf{m} \partial \mathbf{h}}\right) = \left(\frac{\partial^2 \tau}{\partial \mathbf{h} \partial \Delta \mathbf{m}}\right) = \mathbf{0}. \tag{3.5b}$$

Moreover, the slowness at the receiver $\mathbf{p}_R$ equals $-\mathbf{p}_S$, for which we introduce

$$2\mathbf{p}_m = \frac{\partial \tau}{\partial \Delta \mathbf{m}} = \mathbf{p}_R - \mathbf{p}_S. \tag{3.6}$$

The resulting hyperbolic ZO traveltime approximation then reads

$$\begin{aligned}
\tau_\mathrm{hyp}^2(\Delta \mathbf{m}, \mathbf{h}) &= (\tau_0 + 2\mathbf{p}_m \cdot \Delta \mathbf{m})^2 \\
&\quad + \tau_0 \left(\Delta \mathbf{m} \cdot \mathbf{M}_\mathrm{M}^\mathrm{H} \Delta \mathbf{m} + \mathbf{h} \cdot \mathbf{M}_\mathrm{H}^\mathrm{M} \mathbf{h}\right),
\end{aligned} \tag{3.7}$$

where the number of independent variables has been reduced from 14 to 8.

Equation (3.7) was derived under the assumption of a horizontal measurement surface and coinciding anterior and posterior surfaces. This, however, is not a general restriction to the CRS approach. Recent extensions allow to handle smooth as well as rugged top-surface topography and use the kinematic wavefield attributes for redatuming of the stacked section (see, e. g., Heilmann, 2002; Zhang et al., 2002). A CRS-based approach for the handling of data with OBS (ocean bottom seismics) and VSP (vertical seismic profiling) geometries can be found in Boelsen and Mann (2005a) and Boelsen and Mann (2005b).

3.1.2 Physical interpretation of the stacking parameters

In order to obtain a more descriptive form of the CRS operator (3.7), the traveltime derivatives are expressed in terms of physical properties of wavefronts related to the incident/emerging wavefield. The relations derived in the following require an isotropic model and a locally constant near-surface velocity v_0 in the vicinity of the emergence location $(\mathbf{m}_0, \mathbf{0})$ of the central ray.
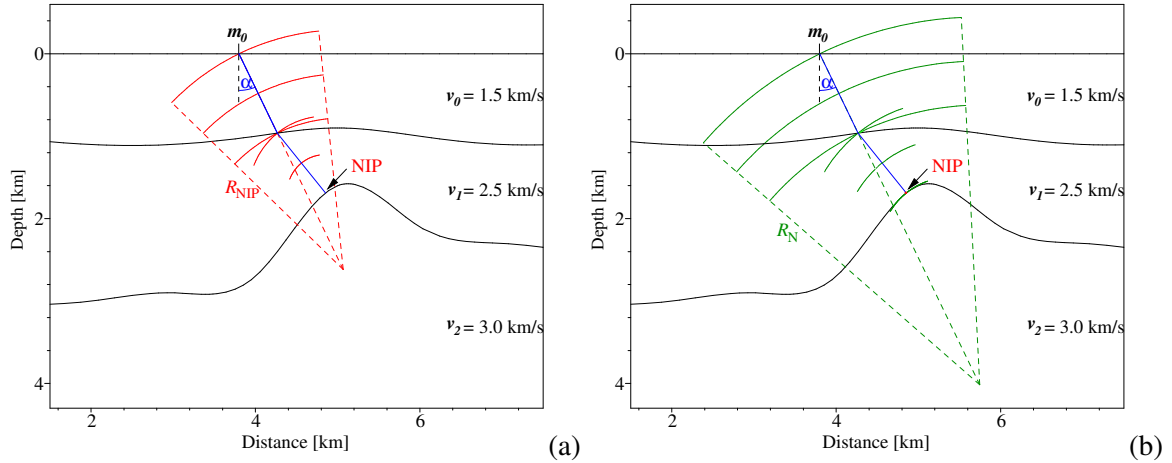
Figure 3.2: NIP and normal wave experiment for a simple 2D model. (a) The explosion of a point source in the NIP causes a NIP wave front that propagates along the central ray indicated in blue. At the emergence location of the central ray, the NIP wave is characterised by the emergence angle α and the local radius R_{NIP}. (b) An exploding reflector element at NIP gives rise to a normal wave that arrives at m_0 with the emergence direction given by α and the local curvature expressed in terms of the radius R_{N} of an approximated segment of a circle (after Mann, 2002).

The vector $\mathbf{p}_m$ defines the horizontal component of the slowness vector of the central ray and, thus, can be related to its emergence direction via

$$\mathbf{p}_m = \frac{1}{v_0} \begin{pmatrix} \cos\phi\sin\alpha \\ \sin\phi\sin\alpha \end{pmatrix}. \tag{3.8}$$

Here, ϕ denotes the azimuth of the emerging ray measured versus the x-axis and α its emergence angle with respect to the surface normal.

The matrices $\mathbf{M}_M^H$ and $\mathbf{M}_H^M$ can be related to the wavefront curvatures of two hypothetical waves, namely the so-called NIP and normal wave, respectively (Hubral, 1983). For this purpose, two experiments are considered which are depicted for a simple 2D model in Figure 3.2.

The first one, the so-called NIP wave experiment, can be carried out by placing a point source in the NIP of the central ray. The excited wave propagates along the central ray to the measurement surface. At the emergence location of the central ray $(\mathbf{m}_0, \mathbf{0})$, the propagation direction of the wave is given by $\mathbf{p}_m$ and the local curvature of the wavefront can be expressed by means of a 2×2 matrix $\mathbf{K}_{\text{NIP}}$. In order to relate this curvature matrix to $\mathbf{M}_H^M$, the NIP experiment is extended to a two-way experiment resulting in identical wavefronts. For this purpose, the wavefront starts at point $(\mathbf{m}_0, \mathbf{0})$ with curvature $-\mathbf{K}_{\text{NIP}}$ and focuses at the NIP where it is reflected back to the surface. Hubral (1983) showed that in paraxial approximation the same traveltimes in the CMP gather would be obtained if the true paraxial reflection points (PIP) of the rays would be placed into the NIP of the central ray (NIP wave theorem). Thus, the matrix $\mathbf{M}_H^M$ can be expressed in terms of the curvature of the NIP wave by

$$\mathbf{M}_H^M = \frac{2}{v_0} \mathbf{H}\mathbf{K}_{\text{NIP}}\mathbf{H}^T, \tag{3.9}$$

where $\mathbf{H}$ is the upper left 2×2 submatrix of the transformation matrix from the ray-centred Cartesian to the global Cartesian coordinate system $\hat{\mathbf{H}}$ defined in equation (2.36).

The second experiment is the so-called normal wave experiment which is equivalent to the exploding reflector experiment introduced by Loewenthal et al. (1976). Thereby, a whole reflector segment in the vicinity of the NIP is assumed to be densely covered with point sources. If all these sources are excited at the same time, a wave is generated with a local curvature equal to the one of the reflector. The corresponding rays are normal to the reflector and the associated wave is called normal wave. The wave emerges at $(\mathbf{m}_0, \mathbf{0})$ with the propagation direction given by $\mathbf{p}_m$ and the wavefront curvature defined by a 2×2 matrix $\mathbf{K}_\mathrm{N}$. Again, the experiment can be extended to a two-way experiment by considering a wave starting at $(\mathbf{m}_0, \mathbf{0})$ with the curvature equal to $-\mathbf{K}_\mathrm{N}$ which is propagated down to the reflector and afterwards reflected back to the measurement surface. As only normal rays are involved in the considerations, the experiment equals a ZO experiment. The curvature matrix $\mathbf{K}_\mathrm{N}$ of the normal wave can be related to the matrix $\mathbf{M}_\mathrm{M}^\mathrm{H}$ via

$$\mathbf{M}_\mathrm{M}^\mathrm{H} = \frac{2}{v_0} \mathbf{H} \mathbf{K}_\mathrm{N} \mathbf{H}^\mathrm{T}, \tag{3.10}$$

where $\mathbf{H}$ again denotes the transformation matrix.

The two angles α and ϕ together with the six independent elements of the symmetric matrices $\mathbf{K}_\mathrm{NIP}$ and $\mathbf{K}_\mathrm{N}$ are summarised as kinematic wavefield attributes. In case of an homogeneous overburden, the attributes can be directly related to properties of the reflector: α and ϕ correspond to the dip and orientation of the reflector element at the NIP. The matrix $\mathbf{K}_\mathrm{NIP}$ has only one independent element K_NIP. The radius of the NIP wave $R_\mathrm{NIP} = 1/K_\mathrm{NIP}$ at the measurement surface equals the length of the ZO normal ray. The matrix $\mathbf{K}_\mathrm{N}$ still consists of up to three independent elements. At the measurement surface, the corresponding curvature matrix equals the sum of the NIP wave radius at the measurement surface and the local curvature matrix of the reflector at the NIP (propagation law). In arbitrary media, the relationship between the kinematic wavefield attributes and the reflector properties is more complex as the attributes are also influenced by the velocity distribution of the reflector's overburden.

Using equations (3.8), (3.9), and (3.10) the traveltime approximation (3.7) reads:

$$\begin{aligned}
\tau_\mathrm{hyp}^2(\Delta\mathbf{m}, \mathbf{h}) &= (\tau_0 + 2\mathbf{p}_m \cdot \Delta\mathbf{m})^2 \\
&\quad + \frac{2\tau_0}{v_0}\left(\Delta\mathbf{m} \cdot \mathbf{H}\mathbf{K}_\mathrm{N}\mathbf{H}^\mathrm{T}\Delta\mathbf{m} + \mathbf{h} \cdot \mathbf{H}\mathbf{K}_\mathrm{NIP}\mathbf{H}^\mathrm{T}\mathbf{h}\right),
\end{aligned} \tag{3.11}$$

Equation (3.11) is the final form of the hyperbolic stacking operator used in the CRS approach. Similar to a conventional stacking velocity analysis, the optimum wavefield attributes for each ZO location $P_0 = (\mathbf{m}_0, t_0)$ are determined automatically by means of coherence analyses in the prestack data. For that purpose, the stacking parameters are varied independently within reasonable limits and a coherence value is determined along the operator (3.11) for each parameter set. The attribute set yielding the highest coherence is used in the actual stack. In 3D, this means solving a global non-linear optimisation problem for 8 independent parameters which requires large compute resources. For practical application, the search for the stacking parameters is usually split up into 3 independent searches in subsets of the prestack data. Details on the search routines can be found in Müller (2003) and Bergler (2004).

The final results of the 3D CRS stack are entire volumes of the wavefield attributes together with the coherence and the CRS stacked volume. The coherence value is a measure of how well the operator

for a given attribute sets fit the prestack data and thus determines—under the assumption that the underlying approximations of the CRS stack are valid—the reliability of the wavefield attributes: the lower the coherence the less reliable are the attributes, they may even be totally meaningless.

An important issue related to the reliability of the wavefield attributes is the size of the aperture used in the search routines. For non-second-order reflection events, the coherence analysis yields second-order stacking parameters and traveltimes that are biased by higher-order contributions. This effect which is proportional to the size of the search aperture is termed as spread-length bias and is also well known from conventional stacking analysis (Al-Chalabi, 1973; Hubral and Krey, 1980). The biased attributes determined in this way do no longer represent second-order but best-fit parameters. Thus, in a strict sense, they are not suitable for further second-order applications. The impact of the spread-length bias can be reduced by choosing small search apertures. However, the stable evaluation of normal and NIP wavefront curvature requires sufficiently large moveout in the data. An approach to correct for the spread-length bias in the 2D CRS stack has been proposed by Müller (2006). In practical applications of the CRS stack, the midpoint and offset aperture has to be chosen with care to find a compromise between these contradicting requests.

3.1.3   The 2D Common-Reflection-Surface stack

In case of a 2D acquisition geometry, the seismic data is recorded along a single line which is usually defined as the x-axis of the global Cartesian coordinate system. This direction is commonly referred to as in-plane or inline direction whereas the y-coordinate defines the out-of-plane or crossline direction. If the properties of the subsurface do not vary in the crossline direction, all rays remain within the vertical observation plane defined by the acquisition line. This situation is usually referred to as 2.5D geometry as it considers 3D wave propagation in a model with 2D variations.

In 2.5D, the midpoint and half-offset coordinates reduce to scalars and the traveltime approximation (3.7) can be expressed in terms of first and second traveltime derivatives by:

$$\tau_{\mathrm{hyp}}^2(\Delta m, h) = \left(\tau_0 + \frac{\partial \tau}{\partial m}\Delta m\right)^2 + \tau_0\left(\frac{1}{2}\frac{\partial^2 \tau}{\partial m^2}\Delta m^2 + \frac{1}{2}\frac{\partial^2 \tau}{\partial h^2}h^2\right). \tag{3.12}$$

In the same way as in the 3D case, the traveltime derivatives can be related to physical properties of the subsurface using equations (3.8), (3.9), and (3.10). Due to the invariance of the model in y-direction, the azimuth ϕ equals zero. Thus, relation (3.8) reduces to

$$\frac{1}{2}\frac{\partial \tau}{\partial m} = \frac{\sin \alpha}{v_0}, \tag{3.13}$$

and second derivatives of the traveltime with respect to the midpoint and offset coordinate are given by

$$\frac{\partial^2 \tau}{\partial m^2} = \frac{2\cos \alpha}{v_0} K_{\mathrm{N}}, \tag{3.14}$$

and

$$\frac{\partial^2 \tau}{\partial h^2} = \frac{2\cos \alpha}{v_0} K_{\mathrm{NIP}}. \tag{3.15}$$

With equation (3.13), (3.14), and (3.15), the final form of the 2D CRS operator yields

$$\tau_{\mathrm{hyp}}^2(\Delta m, h) = \left(\tau_0 + 2\frac{\sin \alpha}{v_0}\Delta m\right)^2 + \frac{2\tau_0 \cos^2 \alpha}{v_0}\left(K_{\mathrm{N}}\Delta m^2 + K_{\mathrm{NIP}}h^2\right). \tag{3.16}$$

3.2 Preconditioning of the kinematic wavefield attributes

For the application of the kinematic wavefield attributes in subsequent processes, an appropriate preconditioning of the CRS sections or volumes is required. In order to remove outliers and noise in the attribute sections, Mann and Duveneck (2004) suggested an event-consistent smoothing algorithm for 2D CRS sections which was extended to the 3D case by Klüver and Mann (2005). The same paper describes an automatic picking strategy based on the coherence values obtained by means of the CRS stack to extract reliable attributes for further processing steps.

3.2.1 The event-aligned volume

The basis for both the smoothing and picking approach is a small window (or volume in 3D) which is aligned with the considered reflection event in the ZO stacked section. The necessary tilting of the window is determined from the local dip information. In order to avoid the mixing of information from different reflection events, the size of the window should not exceed the wavelet size in temporal and the size of the first projected Fresnel zone in horizontal direction. In addition, the dip difference between the central and any other sample is limited by a user-given threshold. Within the smoothing window, local statistics can be applied to the attributes, coherence values, and amplitudes to determine reliable properties.

3.2.2 Event-consistent smoothing

In contrast to conventional stacking velocity analysis, the CRS stack is parameterised in terms of traveltime derivatives which should theoretically remain locally constant over the temporal length of the wavelet. Furthermore, the attributes are expected to vary smoothly along the reflection event in lateral direction as long as the paraxial approximation is valid. As the attributes are independently determined for each ZO sample, this might not always hold and unwanted fluctuation and outliers might occur which deteriorate subsequent applications of the attributes. Within the event-aligned window, local statistics can be applied to determine reliable attributes which are then smoothed by means of a combined median filtering and averaging. Figure 3.3 shows an example of the event-consistent smoothing for a real dataset. Depicted are an inline and crossline section of the dip volume, similar results are obtained for the azimuth volume and the elements of the curvature matrices for the NIP and normal wave. In the last picture in each row, a masked section is displayed which indicates the samples where the smoothing was actually applied. This, however, strongly depends on the user-given coherence and dip difference threshold.

3.2.3 Automatic picking

The automatic picking process utilises the coherence and dip information provided by the CRS method to distinguish reliable attributes from noise. As a sample-by-sample extraction of the attributes only based on the corresponding coherence value is not stable enough, the automatic picking algorithm employs a strategy similar to the one in the event-consistent smoothing based on the event-aligned window. A successful pick requires that a certain percentage of the samples within the window exceed a specified coherence threshold. In this way, uncorrelated noise which might sporadically show high coherence values is avoided in the picking strategy.
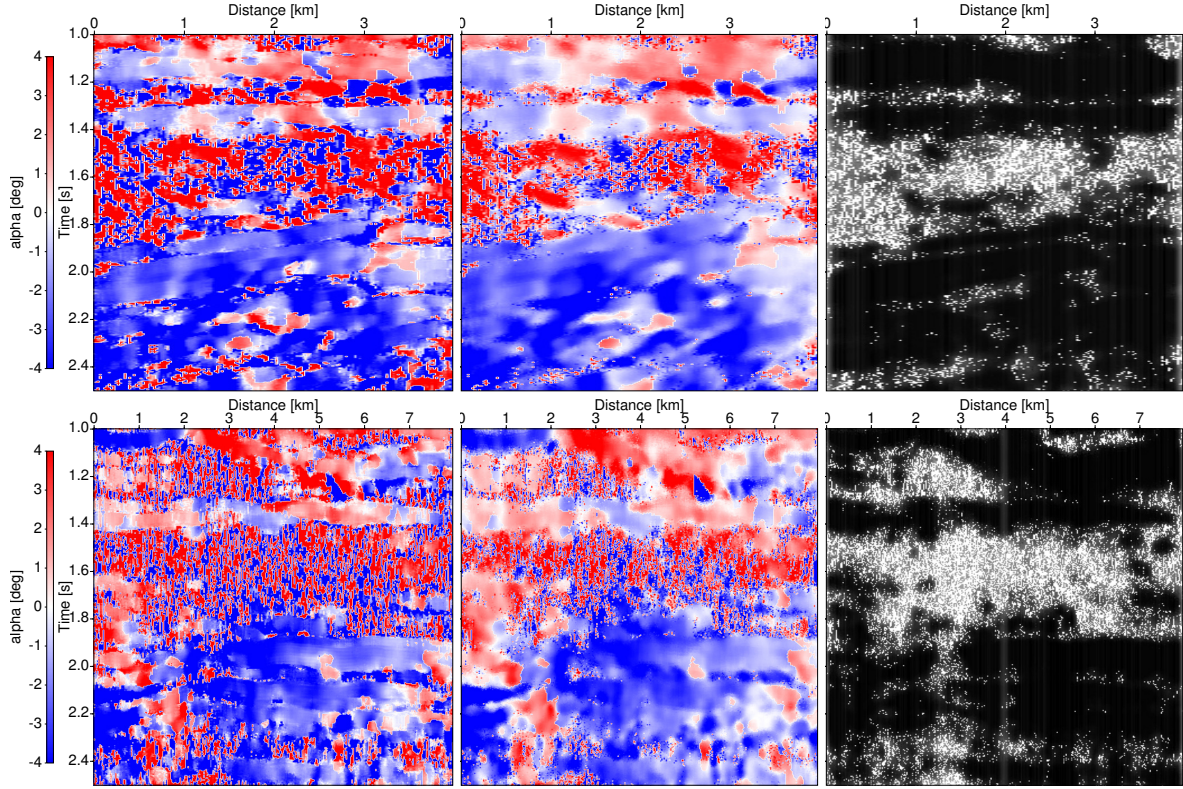
Figure 3.3: Event-consistent smoothing of a dip section (upper row: inline section, lower row: crossline section). Left: original section. Middle: smoothed section. Right: smoothing mask (smoothed samples are indicated in black).

3.3 Application of the kinematic wavefield attributes

The kinematic wavefield attributes provide information beyond the usually determined stacking velocity which find application in a multitude of scenarios. In the CRS-based limited-aperture migration introduced in Chapter 6, the following properties will be used

CRP trajectory. Höcht et al. (1999) derived a second-order approximation of the 2D CRP trajectory in terms of the CRS attributes from geometrical considerations. The projection of the trajectory onto the midpoint-offset plane reads:

$$m(h) = m_0 + r_T \left(\sqrt{h^2/r_T^2 + 1} - 1 \right) \qquad \text{with} \qquad r_T = \frac{R_{\text{NIP}}}{2 \sin \alpha}, \qquad (3.17)$$

which reduces to $m(h) = m_0$ for $\alpha \to 0$. The expression (3.17) provides an exact analytical description of the CRP trajectory in case of a homogeneous overburden where $R_{\text{NIP}} = \tau_0 v_0/2$. The extension to inhomogeneous media is based on the concept of object and image points (Born and Wolf, 1959). Using a circular approximation of the NIP and normal wavefronts, a hypothetical reflector segment can be defined in an auxiliary medium with the constant velocity v_0 which would yield the same emergence angle and wavefront curvatures. The event stemming from the so-defined medium can be directly related to an actual event which allows to establish

a relation between the homogeneous and inhomogeneous case. The transfer of the concept for the homogeneous case to 3D is straightforward and resembles the 2D formula. However, a generalisation to inhomogeneous media as in the 2D case is not possible as the azimuth-dependency of the wavefield properties can not be considered in the approximation.

ZO projected Fresnel zone. Expressing equation (2.59) in terms of the 3D CRS attributes yields the following condition for the size of the ZO projected Fresnel zone:

$$\left| (\mathbf{m} - \mathbf{m}_0) \cdot \left[\mathbf{H}(\mathbf{K}_{\text{NIP}} - \mathbf{K}_{\text{N}})\mathbf{H}^{\text{T}} \right] (\mathbf{m} - \mathbf{m}_0) \right| \leq \frac{v_0 \tau_\omega}{2} . \tag{3.18}$$

The corresponding equation for the 2D case, expressed as half-width W_{F}, reads (Mann, 2002):

$$\frac{W_{\text{F}}}{2} = |m - m_0| = \frac{1}{\cos \alpha} \sqrt{\frac{v_0 \tau_\omega}{2} \left| \frac{1}{R_{\text{N}}} - \frac{1}{R_{\text{NIP}}} \right|} . \tag{3.19}$$

In the CRS-based limited-aperture migration introduced in Chapter 6, all relevant information for the determination of the optimum migration aperture will be directly obtained from the kinematic wavefield attributes.

3.4   Summary

The Common-Reflection-Surface Stack technique addressed in this chapter is a highly automated imaging process for the simulation of ZO sections. Based on a spatial stacking operator, much more traces contribute in the stacking process compared to conventional approaches which leads to stacked sections of improved S/N-ratio. In addition, the CRS method provides a whole set of stacking parameters related to first-order and second-order spatial traveltime derivatives. Considering an isotropic near-surface layer with locally constant near-surface velocity, the stacking parameters can be related to the kinematic properties of two hypothetical wavefronts, namely the direction and curvature of the NIP and normal wave. The information provided by these so-called kinematic wavefield or CRS attributes can be used in a variety of subsequent processing steps.

Chapter 4

True-amplitude Kirchhoff migration

Seismic migration is routinely applied as part of the processing workflow to transform the preprocessed data into an interpretable structural image of the subsurface. By removing the effects of wave propagation from the seismic records, the spatial positioning of the reflection events is corrected and the lateral resolution is increased. For the construction of a structural image, only the kinematic aspects of the transformation process are involved as the amplitudes are not considered so far. In order to provide appropriate input for further amplitude-related analyses, the amplitude change due to geometrical spreading has to be compensated during the migration process. This is achieved by means of an additional weighting factor which makes the migration output *true-amplitude*.

In the last years, the relevance of true-amplitude migration has steadily increased because of the growing significance of AVO/AVA analyses for seismic interpretation. Nowadays, amplitude analyses are routinely applied in target regions where a preceding prestack migration is inevitable (see, e. g., Mosher et al., 1996, and references therein). In particular, prestack time migration provides a convenient tool for this purpose as it shows reduced sensitivity to errors in the velocity model compared to depth migration and is, thus, more likely to provide undistorted amplitudes. Precise dynamic information is essential for AVO/AVA analyses as a meaningful result strongly depends on the quality and reliability of the input amplitudes.

In this chapter, I will focus on the Kirchhoff migration approach which was first formulated by Schneider (1978) based on the early work of Hagedoorn (1954) on the diffraction-stack method. Common to all practical approaches of the Kirchhoff type is the use of a diffraction-stack migration scheme where the optional application of an appropriate weight function provides a true-amplitude output. Based on a zero-order ray approximation of the primary reflections to be imaged, Schleicher et al. (1993) proposed a modified approach that allows true-amplitude migration in arbitrary elastic media even if caustics are present in the wavefield[1]. The associated weight function, which is obtained from the approximate evaluation of the stacking integral, is independent of any reflector properties. In order to provide a general description of Kirchhoff migration and a derivation of the true-amplitude weighting factor, the Kirchhoff approach is first considered in the depth domain following the lines of Schleicher et al. (1993). Here, the derivations hold for arbitrary 3D isotropic models with smoothly curved interfaces provided that the smoothness of the model justifies the use of ray-theoretical approximations. Afterwards, the approximate time domain approach is derived assuming straight rays.

---

[1]excluding source, receiver, and image point

4.1 Basics

Like all migration methods, Kirchhoff migration requires the knowledge of the velocity distribution. Therefore, an appropriate macro-velocity model[2] has to be specified in advance. The time migration velocity model building is further addressed in the next chapter. The subsequent considerations assume that an appropriate time or depth macro-velocity model is available.

Measurement configuration

In the following, a horizontal, non-free measurement surface Σ_M is considered. If data are acquired at a free surface, the resulting effects have to be removed before migration, e.g., using conversion coefficients (Červený, 2001). Source-receiver pairs (S, R) are assumed to be densely distributed on Σ_M. Usually, their positions are specified in a parameterised form: all source-receiver pairs pertaining to a given measurement configuration are described by a 2D configuration vector $\boldsymbol{\xi} = (\xi_1, \xi_2)$ that varies within a planar region A referred to as seismic aperture.

Within A, the position of a seismic trace $U(S(\boldsymbol{\xi}), R(\boldsymbol{\xi}))$ corresponding to a specific source-receiver pair is denoted by $U(\boldsymbol{\xi})$. Thus, every point in the time domain can be described by its coordinates (ξ_1, ξ_2, τ) and is denoted as $N(\boldsymbol{\xi}, \tau)$. Correspondingly, every point in the depth domain is represented by its coordinates $(r_1, r_2, r_3 = z)$ with respect to the global Cartesian coordinate system $\hat{\mathbf{r}}$ and is denoted by $M(\mathbf{r}, z)$. Points lying on an actual reflector carry an additional subscript R.

An arbitrary shot or receiver can be expressed within the global coordinate system by means of 2D coordinate vectors $\mathbf{r}_S$ or $\mathbf{r}_R$, respectively, according to

$$\mathbf{r}_S(\boldsymbol{\xi}) = \mathbf{a}_S + \boldsymbol{\Gamma}_S \, \boldsymbol{\xi}, \tag{4.1a}$$

$$\mathbf{r}_R(\boldsymbol{\xi}) = \mathbf{a}_R + \boldsymbol{\Gamma}_R \, \boldsymbol{\xi}, \tag{4.1b}$$

where $\mathbf{a}_S$ and $\mathbf{a}_R$ are 2D global vectors that depend on the choice of the origin of the coordinate system which defines $\boldsymbol{\xi}$. The 2×2 matrices $\boldsymbol{\Gamma}_S$ and $\boldsymbol{\Gamma}_R$ account for the chosen measurement configuration. Most standard configurations can be described by means of constant configuration matrices, e.g., the common-shot configuration is given by $\boldsymbol{\Gamma}_S = \mathbf{0}$ and $\boldsymbol{\Gamma}_R = \mathbf{I}$, the common-offset configuration by $\boldsymbol{\Gamma}_S = \mathbf{I}$ and $\boldsymbol{\Gamma}_R = \mathbf{I}$, where $\mathbf{0}$ and $\mathbf{I}$ denote the 2×2 zero and identity matrices, respectively. In case of non-flat measurement surfaces and irregular profiles, $\mathbf{r}_S$ and $\mathbf{r}_R$ result from a projection of S or R onto the plane $z = 0$. The corresponding configuration matrices have to be determined for each shot-receiver pair independently.

True-amplitude signal

The seismic data, i.e., the recorded seismic traces, are supposed to consist of primary reflections $U(\boldsymbol{\xi}, \tau)$ that represent the principal component of the reflection events (in case of P-waves, the principal component reflection denotes the particle displacement in propagation direction). In order to correctly account for phase shifts which arise from supercritical reflections or caustics, it is useful to work with complex (analytical) traces. They are derived from the actual recorded data by taking the

---

[2]The term *macro-velocity* refers to the fact that only smooth large-scale features of the model are required.

Hilbert transform of each trace and adding it as imaginary part to the respective trace. In zero-order ray theory the analytic principal component of the particle displacement reads (Červený, 2001)

$$U(\boldsymbol{\xi}, \tau) = U_0(\boldsymbol{\xi}) \, F(\tau - \tau_{\mathrm{R}}) = \bar{R} \, \frac{\mathcal{A}}{\tilde{\mathcal{L}}} \, F(\tau - \tau_{\mathrm{R}}) \,. \tag{4.2}$$

Here, $F(\tau)$ represents the analytic wavelet of a point source which is assumed to be reproducible (thus there is no dependence on $\boldsymbol{\xi}$) shifted by the reflection traveltime τ_{R}. The ray amplitude $U_0(\boldsymbol{\xi})$ can be expressed in terms of the following quantities: $\bar{R}$ denotes the reciprocal (i.e., energy-flux normalised) plane-wave reflection coefficient, $\tilde{\mathcal{L}}$ is the normalised point-source geometrical spreading and $\mathcal{A}$ describes the total transmission loss. Furthermore, the amplitude may be affected by a variety of other processes, among which are absorption, source-receiver characteristics, and scattering. All of these effects also enter into $\mathcal{A}$. A detailed discussion of the factors that may affect seismic amplitudes can be found in Sheriff (1975).

In view of the fact that the true-amplitude signal should be a direct measure of the angle-dependent reflection coefficient, i.e.,

$$U_{TA}(\tau) \equiv \bar{R} \, F(\tau) \,, \tag{4.3}$$

in principle, both $\tilde{\mathcal{L}}$ and $\mathcal{A}$ have to be removed from the primary reflection during migration. Unfortunately, the calculation of $\mathcal{A}$ requires detailed knowledge of the properties of the subsurface. However, taking into account that for many realistic Earth models $\mathcal{A}$ is a slowly varying quantity compared to $\tilde{\mathcal{L}}$ and $\bar{R}$, this factor may be neglected as we are usually interested in relative rather than absolute amplitudes. Therefore, we will assume that primary reflection events can be described sufficiently well by

$$U(\boldsymbol{\xi}, \tau) = \bar{R} \, \frac{1}{\tilde{\mathcal{L}}} \, F(\tau - \tau_{\mathrm{R}}) \,. \tag{4.4}$$

The true-amplitude migration introduced in the following section aims at removing the geometrical spreading factor $\tilde{\mathcal{L}}$ from the data and yields the relative reflection amplitudes as a function of offset.

4.2 3D Kirchhoff depth migration

Common to all Kirchhoff-type migration schemes is the construction of stacking surfaces—the diffraction traveltime surface or Huygens surface τ_{D}—along which a (weighted) summation is performed. For a fixed point $M(\mathbf{r}, z)$ in the depth domain and varying source-receiver pairs $(S(\boldsymbol{\xi}), R(\boldsymbol{\xi}))$, the Huygens surface denotes the set of all points $N(\boldsymbol{\xi}, \tau = \tau_{\mathrm{D}})$ in the time domain for which τ equals the sum of the traveltimes from a source point $S(\boldsymbol{\xi})$ to M and from M to a receiver point $R(\boldsymbol{\xi})$, i.e.,

$$\tau_{\mathrm{D}}(\boldsymbol{\xi}, M) = \tau(S(\boldsymbol{\xi}), M) + \tau(R(\boldsymbol{\xi}), M) \,. \tag{4.5}$$

In a descriptive way, the Huygens surface can be considered as the kinematic image in the time domain of a point in the depth domain.

An alternative way to perform Kirchhoff migration is to smear out the amplitudes along the corresponding isochrons. For a fixed point $N(\boldsymbol{\xi}, \tau)$ in the time domain the isochron is given by all depth points M for which the diffraction traveltime $\tau_{\mathrm{D}}(\boldsymbol{\xi}, M)$ equals the traveltime τ of N. Thus, the isochron can be understood as the kinematic image in the depth domain of a point in the time domain.
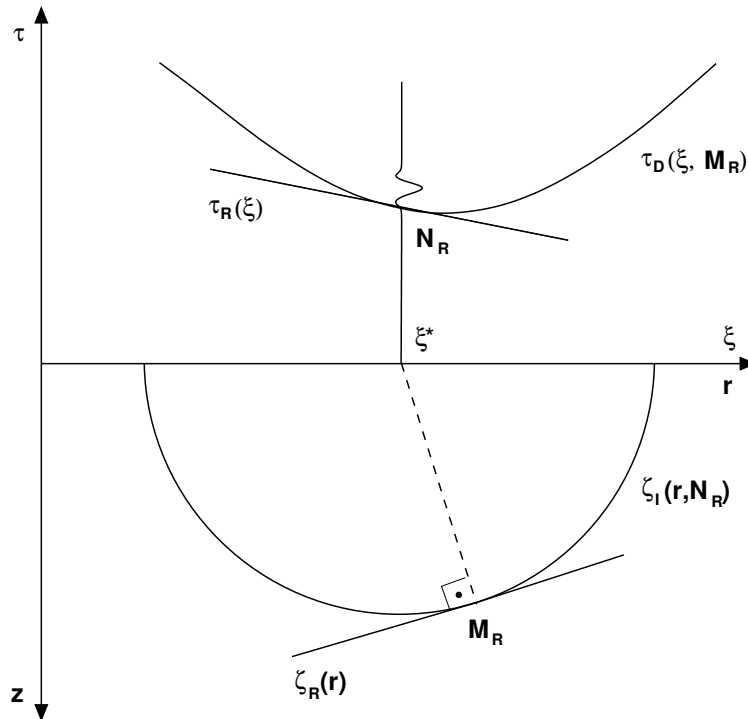
Figure 4.1: Hagedoorn's imaging condition or duality. The Huygens surface $\tau_D(\xi, M_R)$ of a reflection point M_R is tangent to the reflection traveltime surface $\tau_R(\xi)$ at point N_R in the time domain. In turn, the isochron $\zeta_I(r, N_R)$ is tangent to the reflector $\zeta_R(r)$ at point M_R in the depth domain.

Kirchhoff migration is based on the observation that the Huygens surface τ_D pertaining to an actual reflection point M_R and the reflection traveltime surface τ_R are tangent in the time domain at point N_R. In the same way, the isochron pertaining to a reflection event N_R and the reflector are tangent at M_R in the depth domain (see Figure 4.1). These tangency conditions were first observed by Hagedoorn (1954)[3] and are commonly referred to as Hagedoorn's imaging condition or dualities.

The main idea of Kirchhoff migration is to treat each point on a sufficiently dense grid[4] in the considered target area as a potential diffraction point in correspondence to Huygen's principle. The Huygens surface can be calculated independently for any of these points from the kinematic part of the Green's function using the known macro-velocity model. In the migration process, the seismic amplitudes encountered along the Huygens surface are summed up and the result is assigned to the corresponding depth point. According to Hagedoorn's imaging condition, the diffraction traveltime surface is tangent to the primary-reflection traveltime surface for an actual reflection point which leads to a non-negligible summation results due to constructive interference. Otherwise, the contribution ideally yields zero.

---

[3]Hagedoorn introduced the Huygens surface and the isochron as surface of maximum convexity and concavity. However, this terminology is not common.

[4]The discretisation interval depends on the the resolution of the reflection data.

Mathematically, the true-amplitude diffraction stack can be formulated as (Schleicher et al., 1993)

$$V(M) = -\frac{1}{2\pi} \iint\limits_A d\xi_1\, d\xi_2\, W_{DS}(\boldsymbol{\xi}, M)\, \frac{\partial U(\boldsymbol{\xi}, \tau)}{\partial \tau}\bigg|_{\tau=\tau_\mathrm{D}(\boldsymbol{\xi},M)}. \tag{4.6}$$

The individual factors can be described as follows: $U(\boldsymbol{\xi}, \tau)$ and $V(M)$ denote the migration input and output, respectively. Both quantities are chosen complex in order to handle phase shifts. As already mentioned, $U(\boldsymbol{\xi}, \tau)$ is expected to consist of one single primary reflection event. An extension to more than one event can simply be obtained by superposition as an LTI system is assumed. The correct recovery of the source pulse is ensured by applying the time derivative on U (Newman, 1975). The stacking surface is given by the Huygens surface $\tau = \tau_\mathrm{D}(\boldsymbol{\xi}, M)$ with the configuration vector $\boldsymbol{\xi}$ varying over the migration aperture A which coincides with the region of integration. From a theoretical point of view, the migration aperture should be infinite to avoid boundary effects caused by the truncation of the operator. This, however, does not hold for practical applications. The choice of the optimal migration aperture is further discussed in Chapter 6. In any case, limiting the migration aperture requires an appropriate tapering in the summation process. The weight function $W_{DS}(\boldsymbol{\xi}, M)$ which will be derived in the following ensures that the migration result is true-amplitude.

For the solution of integral (4.6) the corresponding expression in the frequency domain is required. For this purpose, an artificial time variable t is introduced in order to allow the application of a Fourier transformation. The value finally assigned to a certain depth point M will then correspond to the migration output at $t = 0$, the so-called imaging condition. Recalling equation (4.2) for the primary reflection event, the time-dependent stack reads

$$
\begin{aligned}
V(M, t) &= -\frac{1}{2\pi} \iint\limits_A d\xi_1\, d\xi_2\, W_{DS}(\boldsymbol{\xi}, M)\, \frac{\partial U(\boldsymbol{\xi}, t + \tau_\mathrm{D})}{\partial \tau} \\
&= -\frac{1}{2\pi} \iint\limits_A d\xi_1\, d\xi_2\, W_{DS}(\boldsymbol{\xi}, M)\, \frac{\bar{R}}{\tilde{\mathcal{L}}}\, \frac{\partial F(t + \tau_\mathrm{dif}(\boldsymbol{\xi}, M))}{\partial \tau}\,,
\end{aligned}
\tag{4.7}
$$

where τ_dif denotes the difference between the diffraction and the reflection traveltime,

$$\tau_\mathrm{dif} = \tau_\mathrm{D} - \tau_\mathrm{R}\,. \tag{4.8}$$

Applying the Fourier transformation yields

$$\hat{V}(M, \omega) = \hat{F}(\omega)\, \frac{-i\omega}{2\pi} \iint\limits_A d\xi_1\, d\xi_2\, W_{DS}(\boldsymbol{\xi}, M)\, \frac{\bar{R}}{\tilde{\mathcal{L}}}\, e^{i\omega\tau_\mathrm{dif}(\boldsymbol{\xi},M)} \tag{4.9}$$

with $\hat{V}(M, \omega)$ and $\hat{F}(\omega)$ being the Fourier transforms of $V(M, \tau)$ and $F(\tau)$, respectively.

The integral (4.9) can now be approximated by means of the Method of Stationary Phase that provides a solution to an integral of the form

$$I(\omega) = \iint\limits_A d\xi\, f(\boldsymbol{\xi})\, e^{i\omega\tau(\boldsymbol{\xi})} \tag{4.10}$$

for sufficiently high frequencies ω (for details see, e. g., Bleistein, 1984). This reveals that non-negligible contributions to $V(M)$ can only stem from so-called stationary points where the gradient
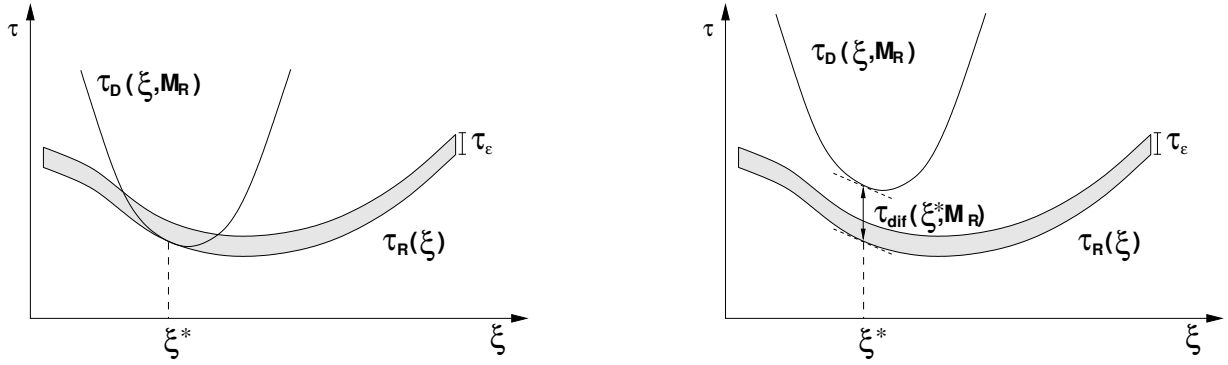
Figure 4.2: Possible stationary situations. Left: diffraction traveltime curve τ_D of an actual reflection point M_R. The curve is tangent to the reflection traveltime curve τ_R at the stationary point ξ^*. Right: diffraction traveltime curve of a point below M_R. Both traveltime surfaces have the same slope at ξ^*.

of the phase function with respect to ξ vanishes, or from the borders of integration. While the first situation constitutes the actual image, the contributions from the boundaries of A are unwanted and have to be suppressed by tapering. A description of the different artifacts that arise from boundary effects as well as strategies to avoid them can be found in Hertweck et al. (2003a).

For the following derivations, we assume that a stationary point ξ^* defined by

$$\nabla_\xi \tau_{\mathrm{dif}}(\xi, M)\Big|_{\xi=\xi^*} = \mathbf{0} \, , \tag{4.11}$$

exists within the aperture A (see Figure 4.2).

Expanding τ_{dif} into a Taylor series with respect to the stationary point yields according to equation (4.11)

$$\tau_{\mathrm{dif}}(\xi, M) = \tau_{\mathrm{dif}}(\xi^*, M) + \frac{1}{2}(\xi - \xi^*) \cdot \mathbf{H}_{\mathrm{dif}}\,(\xi - \xi^*) \, , \tag{4.12}$$

where $\mathbf{H}_{\mathrm{dif}}$ denotes the Hessian matrix given by

$$\mathbf{H}_{\mathrm{dif}} = \left(\frac{\partial^2 \tau_{\mathrm{dif}}(\xi, M)}{\partial \xi_i \partial \xi_j}\right)\Bigg|_{\xi=\xi^*} \, . \tag{4.13}$$

In the following, I assume that $\mathbf{H}_{\mathrm{dif}}$ is non-singular which implies $\det(\mathbf{H}_{\mathrm{dif}}) \neq 0$. Then, the analysis of equation (4.9) yields the approximate solution

$$\hat{V}(M, \omega) \simeq \hat{F}(\omega) W_{DS}(\xi^*, M) \frac{\bar{R}}{\tilde{\mathcal{L}} \, \sqrt{|\det(\mathbf{H}_{\mathrm{dif}})|}} \, e^{i\omega \tau_{\mathrm{dif}}(\xi^*, M) - \frac{i\pi}{2}(1 - \mathrm{Sgn}(\mathbf{H}_{\mathrm{dif}})/2)} \, , \tag{4.14}$$

with $\mathrm{Sgn}(\mathbf{H}_{\mathrm{dif}})$ being the signature of $\mathbf{H}_{\mathrm{dif}}$, i.e., the number of positive eigenvalues minus the number of negative ones. The actual expression for the general weight function is obtained by comparing equations (4.14) and (4.3): if we choose W_{DS} at the stationary point as

$$W_{DS}(\xi^*, M) = \tilde{\mathcal{L}} \, \sqrt{|\det(\mathbf{H}_{\mathrm{dif}})|} \, e^{\frac{i\pi}{2}(1 - \mathrm{Sgn}(\mathbf{H}_{\mathrm{dif}})/2)} \, , \tag{4.15}$$

then the migration output reduces to the spectrum of the true-amplitude wavelet

$$
\hat{V}(M, \omega) \simeq \left\{ \begin{array}{rcl} \bar{R}\,\hat{F}(\omega)\,e^{i\omega\tau_{\mathrm{dif}}(\boldsymbol{\xi}^*, M)} & : & \boldsymbol{\xi}^* \in A\,, \\ 0 & : & \boldsymbol{\xi}^* \notin A\,. \end{array} \right. \tag{4.16}
$$

Here, the phase shift factor accounts for the traveltime difference between the reflected and the diffracted wave at $\boldsymbol{\xi}^*$. Going back to the time domain and inserting the imaging condition $t = 0$ we obtain the desired migration result

$$
V(M) = V(M, 0) = \bar{R}\,F(\tau_{\mathrm{dif}}(\boldsymbol{\xi}^*, M))\,. \tag{4.17}
$$

Due to the fact that the source pulse is a function of finite duration τ_ϵ, the same result holds also for points M that are vertically dislocated from the specular reflection point M_R on the reflector as long as the corresponding traveltime difference $\tau = \tau_{\mathrm{dif}}(\boldsymbol{\xi}^*, M)$ is inside the interval $0 \le \tau \le \tau_\epsilon$. Thus, equation (4.17) can be rewritten in the following way:

$$
V(M) \simeq \left\{ \begin{array}{ll} \bar{R}F(\tau) = U_{TA}(\tau) & \text{at points } M \text{ for which } 0 \le \tau \le \tau_\epsilon, \text{ where } \tau = \tau_{\mathrm{dif}}(\boldsymbol{\xi}^*, M) \\ 0 & \text{else} \end{array} \right. \tag{4.18}
$$

The weight function as defined in equation (4.15) still depends on properties of the (unknown) reflector. A more suitable expression for practical application was derived by Schleicher et al. (1993) using two decomposition theorems. The first one states that the geometrical spreading factor $\tilde{\mathcal{L}}_{SR}$ along a reflected ray $S\,M_R R$ can be factorised into contributions from the two ray branches $\tilde{\mathcal{L}}_{S\,M_R}$ and $\tilde{\mathcal{L}}_{M_R R}$ and an additional factor $\tilde{\mathcal{L}}_F$ that accounts for the influence of the Fresnel zone at the reflection point (Hubral et al., 1992a,b)

$$
\tilde{\mathcal{L}}_{SR} = \frac{\tilde{\mathcal{L}}_{S\,M_R}\tilde{\mathcal{L}}_{M_R R}}{\tilde{\mathcal{L}}_F}\,. \tag{4.19}
$$

The individual factors can be expressed in the following way neglecting mode-conversion:

$$
\mathcal{L}_{S\,M_R} = \sqrt{\frac{\cos(\vartheta_S)\cos(\vartheta_{M_R})}{v_S\,v_{M_R}\,|\det \mathbf{N}_{\mathrm{SM}_R}|}}\,e^{-i\frac{\pi}{2}\kappa_S}\,, \tag{4.20a}
$$

$$
\mathcal{L}_{M_R R} = \sqrt{\frac{\cos(\vartheta_{M_R})\cos(\vartheta_R)}{v_{M_R} v_R\,|\det \mathbf{N}_{\mathrm{M}_R \mathrm{R}}|}}\,e^{-i\frac{\pi}{2}\kappa_R}\,, \tag{4.20b}
$$

$$
\mathcal{L}_F = \frac{\cos\alpha_{M_R}}{v_R}\frac{1}{\sqrt{|\det \mathbf{H}_f|}}e^{-i\frac{\pi}{2}\left[1 - \mathrm{Sgn}(\mathbf{H}_f)/2\right]}\,, \tag{4.20c}
$$

where $v_I, I = (S, M_R, R)$ is the velocity and $\vartheta_I, I = (S, M_R, R)$ the incident or emergence angle at S, M_R, and R, respectively. The KMAH-indices κ_S and κ_R account for caustics along the ray segments $S\,M$ and MR and the Fresnel zone matrix $\mathbf{H}_F$ describes the Fresnel zone in the plane tangent to the reflector at M_R (Hubral et al., 1992b, see also equation (2.57)).

The Fresnel zone matrix $\mathbf{H}_f$ can now be related to the Hessian matrix $\mathbf{H}_{\mathrm{dif}}$ using the following decomposition formula for $\mathbf{H}_{\mathrm{dif}}$

$$
\mathbf{H}_{\mathrm{dif}} = \left(\boldsymbol{\Gamma}_S^{\mathrm{T}}\,\mathbf{N}_{\mathrm{SM}_R} + \boldsymbol{\Gamma}_R^{\mathrm{T}}\,\mathbf{N}_{\mathrm{RM}_R}\right)\left(\mathbf{N}_{\mathrm{M}_R}^{\mathrm{S}} + \mathbf{N}_{\mathrm{M}_R}^{\mathrm{R}}\right)^{-1}\left(\boldsymbol{\Gamma}_S^{\mathrm{T}}\,\mathbf{N}_{\mathrm{SM}_R} + \boldsymbol{\Gamma}_R^{\mathrm{T}}\,\mathbf{N}_{\mathrm{RM}_R}\right)^{\mathrm{T}}\,, \tag{4.21}
$$

where $\mathbf{N}_{\mathrm{SM}_R}$, $\mathbf{N}_{\mathrm{RM}_R}$, $\mathbf{N}_{\mathrm{M}_R}^{\mathrm{S}}$, and $\mathbf{N}_{\mathrm{M}_R}^{\mathrm{R}}$ denote the Hessian matrices of the two ray branches $S\,M_R$ and $M_R R$ defined in the same way as $\mathbf{N}_{\mathrm{S}}^{\mathrm{R}}$, $\mathbf{N}_{\mathrm{R}}^{\mathrm{S}}$, and $\mathbf{N}_{\mathrm{SR}}$ in equation (2.52). $\boldsymbol{\Gamma}_S$ and $\boldsymbol{\Gamma}_R$ are the configuration

matrices introduced in equation (4.1). From equation (4.21), the determinant and signature of $\mathbf{H}_{\text{dif}}$ can be expressed as

$$\sqrt{|\det \mathbf{H}_{\text{dif}}|} \;=\; \frac{\left|\det\left(\boldsymbol{\Gamma}_S^{\text{T}} \mathbf{N}_{\text{SM}_R} + \boldsymbol{\Gamma}_R^{\text{T}} \mathbf{N}_{\text{RM}_R}\right)\right|}{\sqrt{\left|\det\left(\mathbf{H}_f\right)\right|}} \,, \tag{4.22a}$$

$$\text{Sgn}\left(\mathbf{H}_{\text{dif}}\right) \;=\; \text{Sgn}\left(\mathbf{H}_f\right). \tag{4.22b}$$

Inserting the decomposition formula (4.19) together with equations (4.22) into equation (4.15) yields the following expression for the true-amplitude weight:

$$W_{DS}(\boldsymbol{\xi}^*, M_R) = \sqrt{\frac{\cos(\vartheta_S)\cos(\vartheta_R)}{v_S\, v_R}} \; \frac{\left|\det\left(\boldsymbol{\Gamma}_S^{\text{T}} \mathbf{N}_{\text{SM}_R} + \boldsymbol{\Gamma}_R^{\text{T}} \mathbf{N}_{\text{RM}_R}\right)\right|}{\sqrt{\left|\det \mathbf{N}_{\text{SM}_R}\right|} \; \sqrt{\left|\det \mathbf{N}_{\text{RM}_R}\right|}} \, e^{-i\frac{\pi}{2}(\kappa_S + \kappa_R)}. \tag{4.23}$$

As all quantities in equation (4.23) only depend on the ray segments $S M_R$ and $M_R R$ rather than on properties of the reflector, the weight function can be generalised for arbitrary depth points M irrespective of whether M is an actual reflection point:

$$W_{DS}(\boldsymbol{\xi}, M) = \sqrt{\frac{\cos(\vartheta_S)\cos(\vartheta_R)}{v_S\, v_R}} \; \frac{\left|\det\left(\boldsymbol{\Gamma}_S^{\text{T}} \mathbf{N}_{\text{SM}} + \boldsymbol{\Gamma}_R^{\text{T}} \mathbf{N}_{\text{RM}}\right)\right|}{\sqrt{\left|\det \mathbf{N}_{\text{SM}}\right|} \; \sqrt{\left|\det \mathbf{N}_{\text{RM}}\right|}} \, e^{-i\frac{\pi}{2}(\kappa_S + \kappa_R)}. \tag{4.24}$$

The final weight function needs to be determined by means of dynamic ray-tracing. However, if only the modulus of equation (4.24) and not the phase is considered, all relevant quantities can be derived from traveltime information only. Gajewski et al. (2002) presented a migration approach that utilises a generalised moveout formula based on the hyperbolic expansion of the traveltime to interpolate coarsely-gridded traveltime tables onto the fine migration grid and simultaneously calculate the modulus of the true-amplitude weight function.

An alternative expression of the true-amplitude weight was given by Bleistein (1987) in terms of the Beylkin determinant (Beylkin, 1985a,b) omitting caustics. A variety of other expressions of the true-amplitude weight exist which only differ in terms of the physical properties used for description. A comparison can be found in, e. g., Hanitzsch (1997). However, practical applications often utilise an analytic approximation of equation (4.24). A summary and comparison of common simplifications can, e. g., be found in Zhang et al. (2000).

4.3 2.5D migration

In the 2.5D case, the migration integral as well as the true-amplitude weight function can be simplified due to the symmetry of the model (for details see, e. g., Martins et al., 1997; Bleistein et al., 2001). In the following it is assumed that the subsurface is invariant with respect to the crossline direction given by ξ_2. Considering a 2D in-line acquisition, shot and receiver positions depend only on ξ_1. As the ray connecting S and R remains in-plane, all possible reflections stem from points within the vertical plane defined by a constant $\xi_2 = y$. Therefore, ξ_2 selects the symmetry plane in which both the shot and receiver pair and the corresponding reflection point M_R are located.

In order to derive the 2.5D diffraction stack integral, we consider the corresponding 3D formula (4.6) where the diffraction stack is carried out over the ξ_1-ξ_2-plane. As in the 2.5D case the data does not vary with respect to ξ_2, the migration aperture A can be grasped as an infinite strip in this direction and the integral over ξ_2 can be solved analytically. The whole migration integral reduces to an in-plane stack, i. e., the stack is performed over a 2D data slice instead of a 3D data volume. In a descriptive way, this means that the stacking surface of the 3D case shrinks to a curve in 2.5D. Thus, the migration integral can be rewritten as

$$V(M) = \frac{1}{2\pi} \int_{a_1}^{a_2} d\xi_1 \, I_{DS}(\xi_1, \xi_2, M), \qquad a_1 \leq \xi_1 \leq a_2, \tag{4.25}$$

with I_{DS} given by

$$I_{DS}(\xi_1, \xi_2, M) = - \int_{-\infty}^{+\infty} d\xi_2 \, W_{DS}(\xi_1, \xi_2, M) \left. \frac{\partial U(\xi_1, \xi_2, \tau)}{\partial \tau} \right|_{\tau = \tau_D(\xi_1, \xi_2, M)}. \tag{4.26}$$

Evaluating the integral I_{DS} by means of the Method of Stationary Phase yields

$$I_{DS}(\xi_1, \xi_2, M) \simeq \sqrt{2\pi} \left(\left. \frac{\partial^2 \tau_D}{\partial \xi_2^2} \right|_{(\xi_1, 0, M)} \right)^{-\frac{1}{2}} W_{DS}(\xi_1, \xi_2, M) \, \partial_{t^-}^{\frac{1}{2}} U(\xi_1, 0, \tau) \Big|_{\tau = \tau_D(\xi_1, 0, t)}. \tag{4.27}$$

The derivative appearing in the 3D case reduces to an anti-causal half-time derivative denoted by $\partial_{t^-}^{\frac{1}{2}}$ which corresponds to a multiplication with $\sqrt{-i\omega}$ in the frequency domain. An additional factor $\left(\partial^2 \tau_D / \partial \xi_2^2 \right)^{-\frac{1}{2}}$ occurs which enters into the weight function.

Finally, we obtain the following integral for the 2.5D case:

$$V(M) = \frac{1}{\sqrt{2\pi}} \int_{a_1}^{a_2} d\xi \, W_{DS}^{2.5D}(\xi, M) \, \partial_{t^-}^{\frac{1}{2}} U(\xi, \tau) \Big|_{\tau = \tau_D(\xi, M)}, \tag{4.28}$$

where $(\xi_1, 0)$ was replaced by ξ. The region of integration is now given by the limits a_1 and a_2 and represents an in-plane aperture.

The 2.5D weight function can be obtained from its 3D counterpart

$$W^{2.5D} = W^{3D} \left(\frac{1}{\sigma_S} + \frac{1}{\sigma_R} \right)^{-\frac{1}{2}}, \tag{4.29}$$

where σ_S and σ_R denote the out-of-plane spreading factors of he ray segments SM and MR, respectively. Here, the fact was used that 3D point-source geometrical spreading factor $\tilde{\mathcal{L}}$ can be decomposed in the 2.5D case into an in-plane contribution $\hat{\mathcal{L}}$ equal to the 2D spreading and an out-of-plane contribution σ according to

$$\tilde{\mathcal{L}} = \hat{\mathcal{L}} \sqrt{\sigma}. \tag{4.30}$$

The out-of-plane spreading is given by the path integral $\sigma = \int v(s) \, ds$ with s being the arclength along the ray and v the velocity.

Furthermore, it can be shown that the first and the second derivative of τ_D with respect to ξ_2 yield

$$\left. \frac{\partial \tau_D}{\partial \xi_2} \right|_{\xi_2 = y} = 0 \qquad \text{and} \qquad \left. \frac{\partial^2 \tau_D}{\partial \xi_2^2} \right|_{\xi_2 = y} = \frac{1}{\sigma_S} + \frac{1}{\sigma_R}, \tag{4.31}$$

which allows to express $\partial^2 \tau_D / \xi_2^2$ in terms of the out-of-plane spreading factors.

4.4 Kirchhoff time migration

Time migration is conceived for situations where the subsurface only shows mild to moderate lateral velocity variations. Under such conditions, the overburden can be considered as locally homogeneous and may be characterised by an integral velocity. In case of an actual 1D medium, the integral velocity coincides with the root-mean-square velocity v_{RMS} (Dix, 1955):

$$v_{\mathrm{RMS}}^2 = \frac{1}{\tau_0} \int_0^{\tau_0} v^2(t)dt.$$ (4.32)

The determination of time migration velocities from stacking velocities and CRS attributes, respectively, is further discussed in Chapter 5.

In correspondence to the above mentioned assumptions, the diffraction traveltime function (4.5) is approximated using effective parameters of the overburden of the considered subsurface point $M(\mathbf{r}, z)$. In the simplest form, the migration operator reduces to the well-known double-square-root (DSR) equation which can be evaluated analytically (often termed "straight-ray approach"). For the 3D CO case, the DSR equation reads

$$\tau_{\mathrm{D}}(\boldsymbol{\xi}, M) = \sqrt{\frac{\tau_{\mathrm{vert}}^2/4 + (a_{S1} + \xi_1 - r_{M1})^2 + (a_{S2} + \xi_2 - r_{M2})^2}{v_{RMS}(\tau_{\mathrm{vert}})^2}} \\ + \sqrt{\frac{\tau_{\mathrm{vert}}^2/4 + (a_{R1} + \xi_1 - r_{M1})^2 + (a_{R2} + \xi_2 - r_{M2})^2}{v_{RMS}(\tau_{\mathrm{vert}})^2}},$$ (4.33)

where (r_{M1}, r_{M2}) denote the coordinates of the considered depth point M and shot and receiver locations are parameterised according to equation (4.1). The parameter τ_{vert} is the vertical two-way traveltime. As in practice the DSR equation is applied to common-offset gathers, it is more appropriate to recast equation (4.33) in midpoint $\mathbf{m}$, offset azimuth γ, and Euclidean offset $2h$ (see Figure 4.3a)):

$$\tau_{\mathrm{D}}(\mathbf{m}, M) = \sqrt{\frac{\tau_{\mathrm{vert}}^2/4 + (m_1 - h \cos\gamma - r_{M1})^2 + (m_2 - h \sin\gamma - r_{M2})^2}{v_{RMS}(\tau_{\mathrm{vert}})^2}} \\ + \sqrt{\frac{\tau_{\mathrm{vert}}^2/4 + (m_1 + h \cos\gamma - r_{M1})^2 + (m_2 + h \sin\gamma - r_{M2})^2}{v_{RMS}(\tau_{\mathrm{vert}})^2}},$$ (4.34)

with $\mathbf{m} = \frac{1}{2}(2\boldsymbol{\xi} + \mathbf{a}_S + \mathbf{a}_G)$.

The DSR equation is only exact for a constant velocity medium. The geometrical representation of the operator which is depicted in Figure 4.3b) resembles a hyperboloid for the ZO case. For CO, the operator is no longer hyperbolic but pseudo-hyperbolic with flattened apex, which led to the name Cheops pyramid.

For a constant velocity medium, the true-amplitude weight (4.24) can be entirely expressed in terms of the traveltimes τ_S for the ray segment SM and τ_R for MR and the vertical traveltime τ_{vert} (Zhang et al., 2000)

$$W_{DS}^{cv}(\boldsymbol{\xi}, M) = \frac{\tau_{\mathrm{vert}} \, v_{\mathrm{apex}}}{2 \, v_0} \left(\frac{\tau_S}{\tau_R} + \frac{\tau_R}{\tau_S} \right) \left(\frac{1}{\tau_R} + \frac{1}{\tau_S} \right).$$ (4.35)

Here, v_{apex} denotes the migration velocity at the apex location and v_0 is the near-surface velocity.
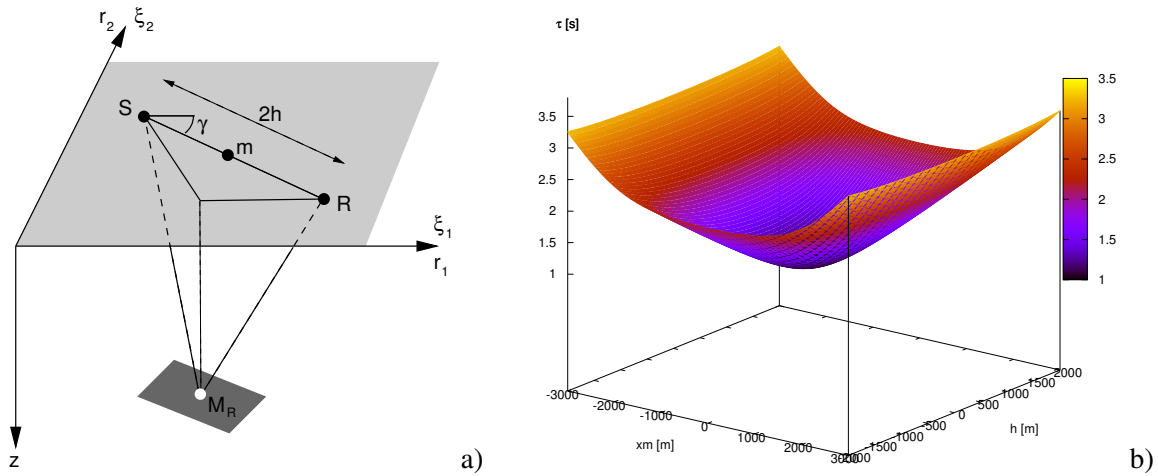
Figure 4.3: a) Sketch of the 3D geometry. The migration operator is usually parameterised in terms of midpoint coordinates **m**, Euclidean offset $2h$ and offset azimuth γ measured with respect to the ξ_1- axis. b) Time migration operator depicted for the 2D situation. The operator is also known as Cheops pyramid due to its characteristic shape.

More sophisticated time migration approaches utilise complex non-hyperbolic operators in order to account for ray-bending. Common extensions incorporate higher-order terms in the DSR equation which allows to handle heterogeneity and/or anisotropy to a certain extent. For a summary of frequently used methods see Robein (2003). However, this usually requires ray-tracing to determine τ_D and makes the approaches more expensive.

As the vertical time τ_{vert} associated with the actual depth location for a particular migration operator is not known, the migration output is assigned to the ZO operator apex described by τ_{apex}. In case of prestack migration, the procedure is carried out for each individual offset and angle bin. For laterally varying media, τ_{apex} significantly deviates from τ_{vert} which leads to a mispositioning of reflection events[5] and unfocused diffractions.

Despite its limitations, (Kirchhoff) time migration is frequently used in seismic processing as it has some distinct advantages over depth migration:

- Time migration shows reduced sensitivity to velocity model errors which leads to focused images even if the used velocity model is insufficiently determined. Moreover, the velocity model building for time migration is much simpler and can be largely automated.

- Using the straight-ray assumption, the migration operator as well as the corresponding weight function can be evaluated analytically without the need of ray-tracing. This leads to significant savings in computational time.

- An AVO/AVA-analysis is usually carried out based on prestack time migration as the migrated amplitudes are less biased by erroneous velocities.

---

[5]Apparent dips on a time image may be even inverted with respect to the true subsurface dips leading to so-called pull-ups and pull-downs which bias interpretation.

- A direct comparison of the migrated section and the stacking result can be preferable for inter-
  pretation.

However, for complex heterogeneous models, time migration strategies fail and depth migration is
inevitable.

4.5 Amplitude analysis

Seismic amplitudes—if properly treated throughout the processing sequence—can be utilised in an
amplitude analysis to infer petrophysical properties of the medium in order to further characterise
reservoir rocks.

Basis for the analysis of amplitude variation with offset (AVO) or incidence angle (AVA) is the ob-
servation that the partitioning of incident energy at a boundary and, correspondingly, the amplitude
of the reflected wave varies as function of incidence angle and medium parameters. The theoretical
framework of AVO/AVA analysis is given by the well-known Zoeppritz equations (Zoeppritz, 1919)
which describe the variation of the reflection coefficient with incident angle considering an incident
plane wave at a plane interface. In amplitude analyses, we are usually interested in the behaviour of
the unconverted P-wave reflection coefficient R_{PP} with incidence angle θ. As the exact solution of the
Zoeppritz equations is complicated and not intuitive, approximations are usually utilised in practical
applications. Most of these expressions are suited for small incidence angles and small variations of
layer parameters (small dip assumption), a situation which is usually encountered in seismic reflection
applications. One widely used approximation was proposed by Shuey (1985) and reads

$$R_{PP}(\theta) \approx R_{PP}(0) + G \sin(\theta)^2 . \tag{4.36}$$

Here, $R_{PP}(0)$ represents the normal incidence reflection coefficient. R_{PP} and the second parameter G
are related to the P-velocity v_P, S-wave velocity v_S and density ρ according to

$$R_{PP}(0) = \frac{1}{2}\left(\frac{\Delta v_P}{\langle v_P \rangle} + \frac{\Delta \rho}{\langle \rho \rangle}\right) \tag{4.37a}$$

$$G = \frac{1}{2}\frac{\Delta v_P}{\langle v_P \rangle} - 2\left(\frac{\langle v_S \rangle}{\langle v_P \rangle}\right)^2 \left(2\frac{\Delta v_S}{\langle v_S \rangle} + \frac{\Delta \rho}{\langle \rho \rangle}\right), \tag{4.37b}$$

where the Delta indicates the change of the parameter and the brackets $\langle \, \rangle$ the average of the parame-
ter across the interface. Equation (4.36) establishes a linear relationship between $R_{PP}(\theta)$ and $\sin(\theta)^2$.
Therefore, $R_{PP}(0)$ and G represent the intercept and gradient and may be estimated by linear regres-
sion. A stable linear-regression approach in the presence of noise can be found in Walden (1991).

Equation (4.36) is based on the assumption of plane interfaces. Curved interfaces are expected to
show a lensing effect which has to be compensated beforehand. This is best achieved by a prestack
time or depth migration. If amplitudes are extracted from a CIG, information belonging to a common
subsurface position, i. e., from a true CRP ray path, is obtained. As prestack migration is commonly
carried out in the common offset domain, the extracted amplitudes have to be mapped to the angle
domain first. In recent years, migration algorithms have been developed which perform migration
directly in the angle domain (see, e. g., Xu et al., 2001). These are, however, rather costly in terms of
computational requirements.

A visual representation of the AVO analysis which allows a simple classification of different AVO behaviours is obtained by plotting the intercept value versus the gradient. Such AVO crossplots are generated using the amplitudes extracted along a considered horizon or within a time window, where each AVO curve is represented by a single point. Additional colour-coding of the samples with respect to the traveltime allows to distinguish the horizons in a window-based crossplot. In this way, differences in AVO responses can be identified and may be related to variations in the lithology and / or fluid type. The possibility to detect clear and reliable trends in a crossplot strongly depends on the quality of the amplitudes and the noise level in the data. Random noise leads to an elliptical distribution of the samples (often termed "noise ellipse") as the gradient estimation is quite sensitive to noise.

A detailed treatment of AVO analysis can be found in Castagna and Backus (1993), see also references therein.

4.6 Summary

In this chapter, a descriptive explanation of the Kirchhoff migration process was presented based on the tangency of Huygens surface and reflection event in the time domain. In addition, the true-amplitude weight function was derived from the approximative evaluation of the migration integral by means of the Method of Stationary phase. Applied in the stacking process, the weight function provides migrated amplitudes which are free of geometrical spreading effects and thus become a direct measure of the angle-dependent reflection coefficient. A subsequent analysis of the amplitude variation with offset or reflection angle allows to gain information on the elastic properties of the subsurface.

Chapter 5

Time migration velocities from kinematic wavefield attributes

Kirchhoff time migration is usually parameterised in terms of RMS velocities defined at the apex of the migration operator. For 1D media, the apex location coincides with the stationary point and the RMS velocity equals the NMO velocity. Although time migration is strictly defined for 1D media, only, it is still applicable to media showing moderate lateral velocity variations. For these types of media, the parameterisation in terms of RMS velocities no longer holds. The migration velocities are defined at the apex time τ_{apex} which no longer coincides with the vertical time τ_{vert} and the associated integral velocity is referred to as time migration velocity v_{c}. This velocity is not a physical property but can rather be interpreted as a "best-fit" parameter that governs the migration operator and fits it to the reflection events in the data, i.e., it leads to flat image gathers after migration. It no longer equals the NMO velocity which is attached to the stationary point rather than to the apex location of the migration operator.

In conventional processing, time migration velocities are usually determined from stacking velocities. In order to correct for the difference between both velocities, the velocity model is iteratively refined.

An alternative way to determine time migration velocities for the 2D case was suggested by Mann et al. (2000) and Mann (2002). Based on the fact that the CRS operator allows to estimate an approximate diffraction response, the kinematic wavefield attributes defined at the stationary point for ZO can be mapped into the apex of the corresponding diffraction operator and serve as input for the determination of time migration velocities. Mann et al. (2000) utilised the direct relationship between the CRS reflection and diffraction operators to migrate a ZO sample by mapping its amplitude to the associated apex location without the use of an explicit migration velocity model. However, such a point-to-point mapping does not necessarily yield contiguous images of the reflection events. Therefore, it provides a first impression of the subsurface's structure but cannot be considered as a final image.

The same methodology can be used to derive an explicit time migration velocity model. The velocities obtained in this way parameterise the CRS-based diffraction operator rather than the DSR operator. Both operators coincide in the poststack case but deviate from each other if large offsets together with large midpoint displacements are considered. Nevertheless, the CRS-based migration velocity model provides a good approximation of the required velocities as long as offsets and midpoint displacements are moderate. This is sufficient in the context of this thesis, as (true-amplitude) time migration is mainly considered to generate images for further amplitude analysis where far offsets are omitted.
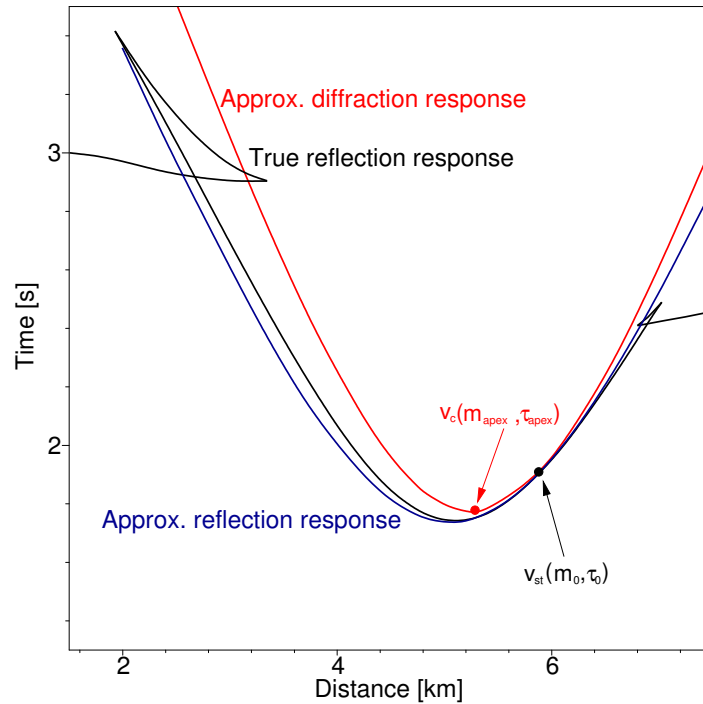
Figure 5.1: Time migration velocity and CRS operator. The migration velocity v_c is defined at the apex location of the migration operator (m_{apex}, τ_{apex}) which significantly deviates from the ZO location (m_0, τ_0) where the stacking velocity v_{st} is defined for dipping events. The CRS approach provides an approximation of the true reflection response (black curve, the approximation is shown in blue) as well as an approximation of the diffraction response (red curve) which defines the time migration velocity and the apex location (modified after Mann, 2002).

The following derivations of the time migration velocities from CRS attributes for the 2D case follow the lines of Mann (2002). A strategy to extend the approach to 3D was presented by Bergler (2004).

5.1 Conventional time migration velocity analysis

The aim of prestack time migration velocity analysis is to obtain a velocity v_c attached to the apex of the time migration operator (m_{apex}, τ_{apex}) that provides a migration operator which fits the reflection events in the prestack data (see Figure 5.1). Usually, stacking velocities are used as input for the velocity model determination. In principle, both the difference in location and velocity have to be considered in the migration velocity model building. This can be done explicitly by mapping the wavefield attributes defined at the stationary point into the apex of the migration operator, or implicitly by an updating scheme as in conventional approaches.

Conventional time migration velocity analysis is either carried out as an iterative approach based on residual moveout analysis (RMO) or utilises a scanning routine similar to stacking velocity analysis (see, e. g., Robein, 2003). The RMO routine usually starts with an initial velocity field which is set
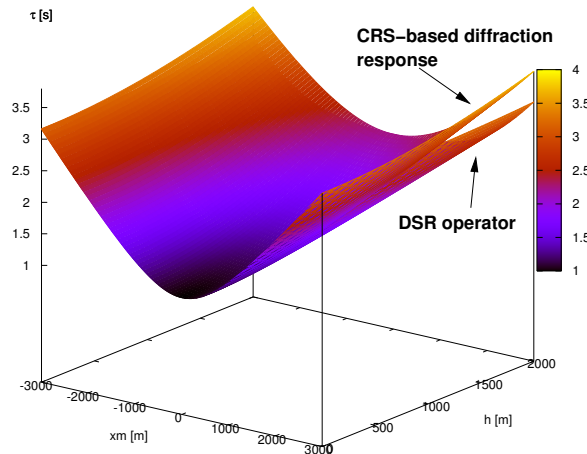
Figure 5.2: Double-square-root and CRS-based diffraction operator for a 2D homogeneous model. The operators only coincide in the planes defined by $m = 0$ and $h = 0$, otherwise they deviate from each other.

up using the stacking velocities determined by means of a conventional stacking velocity analysis. Selected image gathers are constructed using prestack time migration which usually show residual moveout. Afterwards, an inverse NMO correction is applied using the initial velocities. The gathers then enter into a classical stacking velocity analysis which yields an updated migration velocity model. As the velocity analysis is usually carried out on a rather coarse grid, the velocities have to be interpolated on the migration grid. The RMO chain may be iterated to refine the velocity field.

In contrast, the scanning approach tests for a set of velocities or velocity functions at the same time. The best result is determined on the basis of CIG flatness and interpretative criteria. The approach is rather compute-intensive as several full prestack time migrations have to be performed. However, it provides better results compared to the RMO routine if a wide range of different velocities is tested.

5.2 DSR vs. CRS diffraction operator

In order to determine the time-migration velocity values from CRS attributes, the wavefield attributes for one ZO location P_0 have to be mapped into the apex of the corresponding time migration operator which is also provided by the CRS approach (see Figure 5.1). This diffraction response approximates the true diffraction response up to second order. However, it only coincides with the DSR operator for either zero offset or a midpoint displacement equal zero. Otherwise, the DSR and the CRS-based diffraction operator deviate from each other as can be seen from Figure 5.2. The migration velocity obtained from the CRS attributes does therefore not coincide with the "best-fit" parameter required to build up the DSR operator.

The difference between both parameterisations is even more striking in 3D where the CRS diffraction response is parameterised in terms of a 2×2 matrix. In correspondence to the 3D stacking velocity, the migration velocity becomes azimuth-dependent for media with lateral variations. The DSR operator, however, is parameterised in terms of a single velocity. In the poststack case, the DSR operator can

55

be calculated using the migration velocity determined for the considered azimuth of the midpoint displacement. In prestack migration, the velocity matrix in the CRS-based diffraction operator is related to the azimuth of the midpoint displacement and the offset azimuth. In the DSR operator, these azimuths are coupled. Therefore, both dependencies cannot be considered at the same time. To allow consistency with the poststack case, only the azimuth of the midpoint displacement is considered for the determination of the azimuth-dependent migration velocity. The CRS-based diffraction operator could in principle be used to consider the azimuth-dependent velocity, but is in general less suited for prestack migration (which also holds for the 2D case).

Although the migration velocity derived from the wavefield attributes does not exactly provide the required "best-fit" time migration velocities, the CRS-based velocity model building is attractive as the obtained migration velocities are defined at their correct locations and provide a good estimate of the searched-for values. Velocity values are obtained for each (reliable) attribute set which can be extracted by means of the automatic picking procedure described in Section 3.2. The velocity model building itself is straight-forward and can be applied in a highly automated manner. In Chapter 7 and 8, the CRS-based time migration velocity model building is applied to both synthetic and real data examples where the consistency of the velocity models with the prestack data can be examined from the flatness of the common-image-gathers.

In the subsequent sections, the CRS-based time migration velocity model building is discussed for the 2D and 3D case. The approach utilises the CRS-based ZO diffraction operator to approximate the migration velocity together with the associated apex location. The generalisation of the model-building approach to the CRS-based finite-offset diffraction operator is not consistent with the straight-ray approach used for time migration and is not considered here.

5.3   2D CRS-based time migration velocity model building

As already mentioned in Chapter 3, the NIP wave is related to a hypothetical point source in depth. Therefore, it allows to approximate the diffraction response of a hypothetical diffractor located on the (unknown) reflector segment in depth as it is independent of the reflector's curvature. For a true diffractor, the radius of curvature of the normal wave $R_\mathrm{N} = 1/K_\mathrm{N}$ and the radius of the NIP wave $R_\mathrm{NIP} = 1/K_\mathrm{NIP}$ coincide. In order to simulate a diffraction response for a reflector with $R_\mathrm{NIP} \neq R_\mathrm{N}$, the radius of the normal wave is set to the value of R_NIP which is obtained for the corresponding true reflection event. The resulting diffraction traveltime τ_D reads

$$\tau_\mathrm{D}^2(\Delta m, h) = \left(\tau_0 + 2\frac{\sin\alpha}{v_0}\Delta m\right)^2 + \frac{2\tau_0 \cos^2\alpha}{v_0\,R_\mathrm{NIP}}\left(\Delta m^2 + h^2\right). \tag{5.1}$$

For $h = 0$, the approximate diffraction response coincides with the poststack time migration operator using the straight-ray assumption. Its apex location can be written as (Mann, 2002)

$$m_\mathrm{apex} = m_0 - \frac{R_\mathrm{NIP}\,\tau_0\,v_0\,\sin\alpha}{2\,R_\mathrm{NIP}\,\sin^2\alpha + \tau_0\,v_0\,\cos^2\alpha}, \tag{5.2a}$$

$$\tau_\mathrm{apex}^2 = \frac{\tau_0^3\,v_0\,\cos^2\alpha}{2\,R_\mathrm{NIP}\,\sin^2\alpha + \tau_0\,v_0\,\cos^2\alpha}. \tag{5.2b}$$

Expressing the CRS diffraction response (5.1) for $h = 0$ in apex coordinates (5.2) immediately yields the poststack time migration operator parameterised with a migration velocity v_c in terms of CRS

wavefield attributes:

$$\tau_{\mathrm{D}}^2(x) = \tau_{\mathrm{apex}}^2 + \frac{4\left(m - m_{\mathrm{apex}}\right)^2}{v_{\mathrm{c}}^2} \quad \text{with} \tag{5.3a}$$

$$v_{\mathrm{c}}^2 = \frac{2\,v_0^2\,R_{\mathrm{NIP}}}{2\,R_{\mathrm{NIP}}\,\sin^2\alpha + v_0\,\tau_0\,\cos^2\alpha} \,. \tag{5.3b}$$

Each set of (reliable) CRS attributes can be related to a migration velocity value and its corresponding location in the time domain. For the actual building of a time migration velocity model, the wavefield attributes are smoothed along the reflection events and then extracted by means of the automated picking algorithm. The migration velocity v_{c} and the corresponding apex location $(m_{\mathrm{apex}}, \tau_{\mathrm{apex}})$ can now be calculated and enter into a subsequent infill procedure: the migration velocities are interpolated and extrapolated using a distance weighted polynomial interpolation. This infill approach guarantees a smooth interpolation of the velocity values but has no sound physical justification.

An example for the 2D velocity model building taken from the synthetic dataset discussed in Chapter 7 is depicted in Figure 5.3. A significant difference between apex locations and stationary points can be observed for dipping reflection events, especially at the flanks of the dome-like structure. The corresponding migration velocities are shifted to lower values with respect to the stacking velocities.

5.4 3D CRS-based time migration velocity model building

Time migration velocities can be obtained from the 3D wavefield attributes in the same way as in the 2D case. For arbitrary 3D media, the stacking velocity as well as the time migration velocity associated with the CRS operator are azimuth-dependent[1]. Under the prerequisite that the dataset under consideration was acquired with an appropriate azimuth coverage to provide three stable independent components of the matrix $\mathbf{M}_{\mathrm{H}}^{\mathrm{M}}$, a time migration velocity matrix can be determined from which the velocity for each azimuth γ can be derived. Here, γ denotes the midpoint displacement azimuth as all considerations are restricted to the poststack case. An extension of the approach to finite offset is possible. However, then the migration velocity depends on both the azimuth of the midpoint displacement and the offset azimuth which cannot be considered separately in the DSR operator (4.34).

In case the subsurface does not show a distinct dependence on the azimuth or the survey design is not appropriate, an adapted strategy can be employed to derive a conventional time migration velocity model without azimuth dependence from the single element of matrix $\mathbf{M}_{\mathrm{H}}^{\mathrm{M}}$.

Setting $\mathbf{M}_{\mathrm{M}}^{\mathrm{H}} := \mathbf{M}_{\mathrm{H}}^{\mathrm{M}}$ and $\mathbf{h} = \mathbf{0}$ in equation (3.11) yields the 3D Kirchhoff poststack time migration operator assuming straight rays:

$$\tau_{\mathrm{D}}^2(\Delta\mathbf{m}, \mathbf{h}) = (\tau_0 + 2\mathbf{p}_m \cdot \Delta\mathbf{m})^2 + \frac{2\tau_0}{v_0}\left(\Delta\mathbf{m} \cdot \mathbf{M}_{\mathrm{H}}^{\mathrm{M}}\Delta\mathbf{m}\right). \tag{5.4}$$

Its apex location $(\mathbf{m}_{\mathrm{apex}}, \mathbf{h} = \mathbf{0}, \tau_{\mathrm{apex}})$ can be written as:

$$\tau_{\mathrm{apex}}^2 = \left(\tau_0 - 4\tau_0\,\mathbf{p}_m \cdot \tilde{\mathbf{M}}_{\mathrm{H}}^{\mathrm{M}}\,\mathbf{p}_m\right)^2 + 4\tau_0^3\,\mathbf{p}_m \cdot \tilde{\mathbf{M}}_{\mathrm{H}}^{\mathrm{M}} \cdot \mathbf{M}_{\mathrm{H}}^{\mathrm{M}}\,\tilde{\mathbf{M}}_{\mathrm{H}}^{\mathrm{M}}\,\mathbf{p}_m\,, \tag{5.5a}$$

$$\mathbf{m}_{\mathrm{apex}} = \mathbf{m}_0 - 2\tau_0\,\tilde{\mathbf{M}}_{\mathrm{H}}^{\mathrm{M}}\,\mathbf{p}_m\,, \tag{5.5b}$$

---

[1]In this thesis, the azimuth-dependency is considered as an effect of inhomogeneity rather than anisotropy.
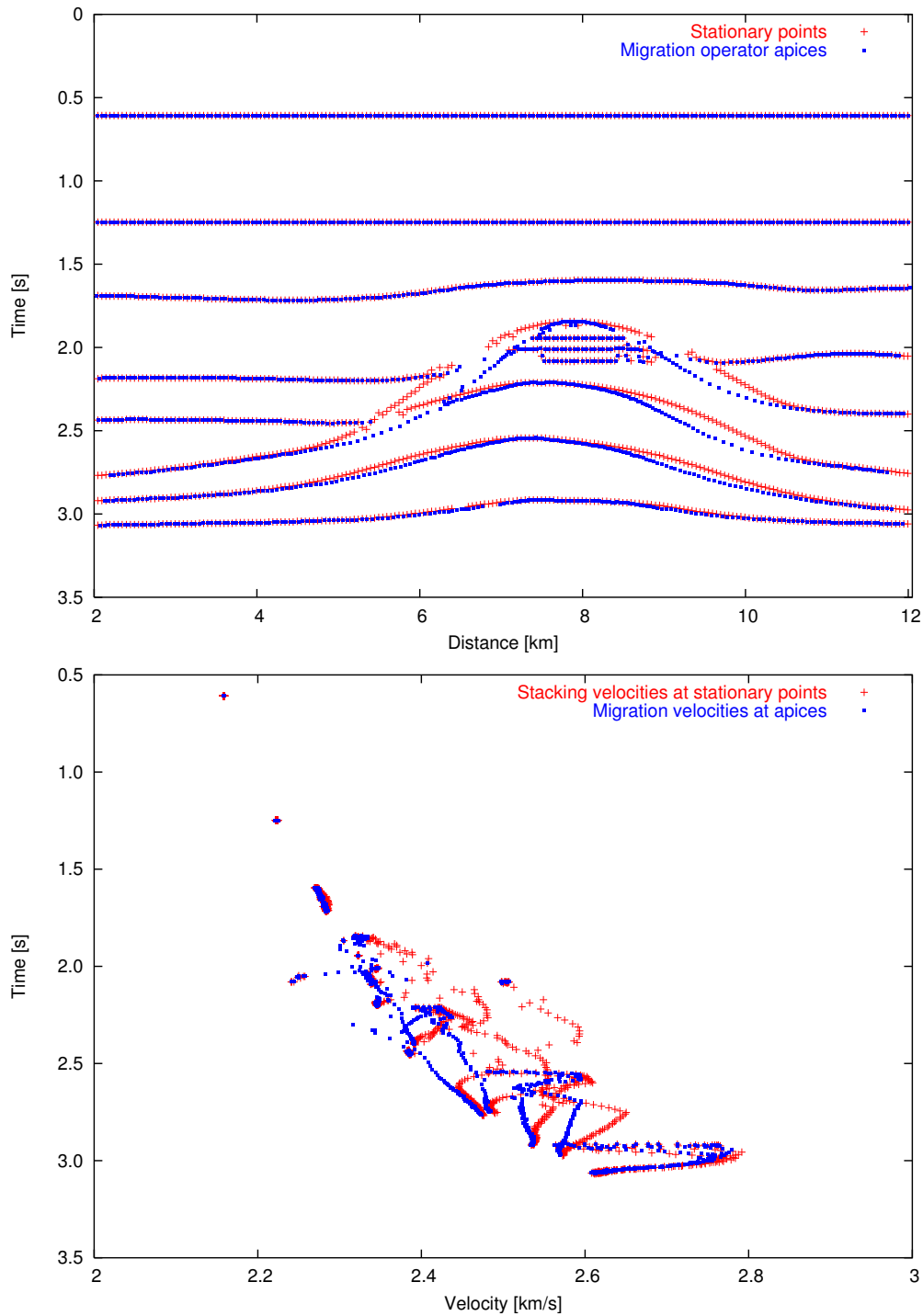
Figure 5.3: Determination of migration velocities from CRS attributes for a 2D synthetic dataset. The red crosses indicate picks and stacking velocities in the unmigrated time domain, the blue squares picks and time migration velocities in the migrated time domain calculated according to equations (5.3). The upper figure shows the stationary points vs. migration operator apices; the lower figure stacking velocities vs. migration velocities. Note the significant shift in location and velocity for dipping reflection events.

with $\tilde{\mathbf{M}}_H^M = (4\mathbf{p}_m\,\mathbf{p}_m^T + \tau_0\mathbf{M}_H^M)^{-1}$.

Expressing the CRS diffraction response (5.4) in apex coordinates (5.5) provides the poststack time migration operator parameterised in terms of CRS wavefield attributes:

$$\tau_D^2(\Delta\mathbf{m}) = t_{apex}^2 + 4\left(\mathbf{m} - \mathbf{m}_{apex}\right)^T \mathbf{V}_C^{-1}\left(\mathbf{m} - \mathbf{m}_{apex}\right) . \tag{5.6}$$

Here, the symmetric 2×2 matrix $\mathbf{V}_C = 4\,\tilde{\mathbf{M}}_H^M$ is related to the azimuth-dependent time migration velocity $v_c(\gamma)$ defined at the operator apex by

$$v_c(\gamma) = \left(V_{C11}\cos^2\gamma + V_{C12}\cos\gamma\sin\gamma + V_{C22}\sin^2\gamma\right)^{\frac{1}{2}} . \tag{5.7}$$

where V_{Cij} denotes the i, jth element of the matrix $\mathbf{V}_C$.

Using equation (5.6) together with (5.5) and (5.7) relates the CRS attributes to a location in the time domain and defines the corresponding time migration velocities for arbitrary azimuth directions, e. g., $\gamma = 0°, 45°$, or $90°$:

$$v_C(0°) = (V_{C11})^{\frac{1}{2}} , \tag{5.8a}$$

$$v_C(45°) = \left(V_{C12} + \frac{1}{2}\left(V_{C11} + V_{C22}\right)\right)^{\frac{1}{2}} , \tag{5.8b}$$

$$v_C(90°) = (V_{C22})^{\frac{1}{2}} . \tag{5.8c}$$

For the calculation of v_C, reliable attributes are extracted from the smoothed 3D attribute volumes by means of the CRS-based automatic picking. In principle, the kinematic wavefield attributes could be directly converted to the desired matrix elements. However, an interpolation of the matrix elements is unphysical as the matrix element V_{C12} does not show a smooth distribution. Therefore, the attributes are firstly used to derive azimuth-dependent time migration velocities for the azimuths $\gamma = 0°, 45°$, and $90°$. Each of these models is then inter- and extrapolated to cover the whole target area. The velocity models are then transformed back to matrix elements from which the migration velocity for a specified azimuth can be obtained according to equation (5.7).

5.5   Summary

In this chapter, the derivation of time migration velocities from kinematic wavefield attributes in the 2D as well as in the 3D case was discussed. In the model building, the temporal and spatial shift between the stationary point and the apex of the migration operator is considered. In the 3D case, the approach allows to handle azimuth-dependent migration velocities. However, this aspect cannot fully be exploited in the DSR operator. Albeit the obtained velocities parameterise the CRS diffraction response rather than the DSR operator, they provide a good approximation of the searched-for velocities. The CRS-based model building is efficient and can be highly automated compared to updating approaches often used for conventional time migration velocity determination.

Chapter 6

Minimum-aperture Kirchhoff time migration

The achievable image quality as well as the reliability of the migrated amplitudes in Kirchhoff migration strongly depend on the selection of the migration aperture. From a theoretical point of view, the aperture should be limitless for noise-free data to avoid artifacts caused by the abrupt truncation of the migration operator. In practical implementations, the aperture is always limited by the finite acquisition area and recording time. Usually, a taper is applied to reduce aperture-related boundary effects. A further restriction of the aperture can be advantageous with respect to both the efficiency of the migration process and the quality of the migration result.

The optimal choice of the migration aperture requires additional knowledge of the subsurface and is, thus, not possible in conventional Kirchhoff migration schemes. In general, a user-defined aperture is employed which linearly increases with depth or time of the image location. Both a strong underestimation and overestimation of the optimal aperture size leads to deteriorated and even meaningless migration results.

Minimum-aperture migration aims at restricting the aperture to the smallest possible size which still covers the part of the migration operator constructively contributing in the summation. Jäger (2005a) employed the CRS attributes in prestack and poststack Kirchhoff depth migration to estimate the size and location of the minimum migration aperture. His primary goal was to improve the migrated image by reducing migration artifacts and avoiding operator aliasing. In addition, the efficiency of the migration process is considerably increased. A drawback of the approach is its sensitivity to velocity model errors which also directly influences the stability of the minimum aperture determination. This point is not crucial as long as only kinematic aspects are considered, but is of importance if the amplitudes are to be used for further processing.

In the time domain approach considered here, the sensitivity to model errors is significantly reduced and the stability of the approach is increased. Due to the considered straight ray assumption, one deals with smooth, analytic migration operators with well-defined spatial derivatives and consistent, analytic true-amplitude weight factors. The focus of the approach lies on improving the quality of the migrated image and, in particular, of the amplitudes. The efficiency is of minor importance in time migration as the computational time is already significantly reduced compared to depth migration.
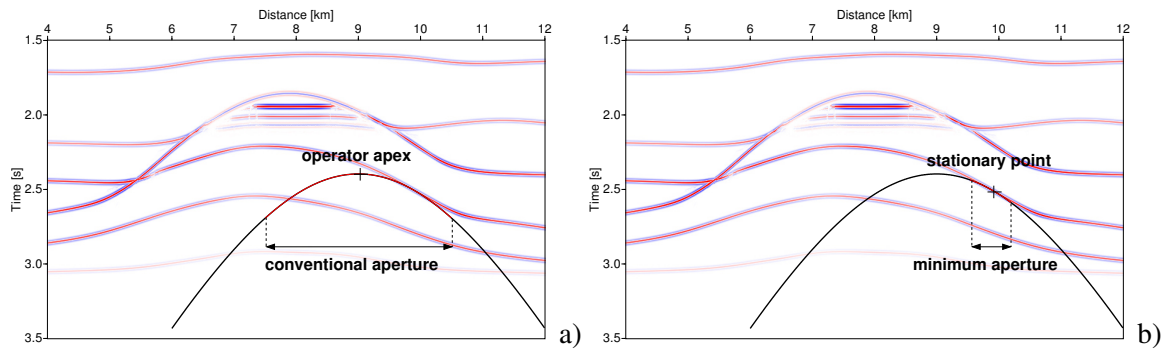
Figure 6.1: 2D poststack time migration operator with a) conventional aperture centred around its apex and with b) minimum aperture centred around the stationary point. The respective part of the operator within the aperture is depicted in red.

6.1 Aperture and amplitudes

As mentioned above, the size of the migration aperture strongly influences the quality and reliability of the migration amplitudes. Schleicher et al. (1997) showed that optimum amplitude behaviour is obtained if the migration aperture is restricted to the size of the projected Fresnel zone. The advantages of minimum-aperture migration with respect to the amplitudes are also obvious from Figure 6.1: in conventional migration the stationary point where the operator is tangent to the event and the projected Fresnel zone are unknown prior to migration. Thus, the aperture has to be centred around the operator's apex; its size is usually user-controlled.

Choosing the aperture too small leads to the loss of steep events in the migration result. If the aperture does not even fully cover the size of the projected Fresnel zone the amplitudes become meaningless as can be seen from Figure 6.2 where migrated amplitudes are depicted as a function of the aperture size. On the other hand, too large an aperture means that a lot of noise off the event and possibly other events contribute to the diffraction stack and deteriorate the amplitudes. In addition, the risk of operator aliasing is increased and antialias filters tend to falsify amplitudes: Zhang et al. (2001) showed that the application of anti-aliasing filters often affects the amplitudes of migrated gathers stronger than the selection of the migration weight function. In contrast, the minimum-aperture operator avoids these problems as its location and size fits the constructively contributing part of the reflection event, thus providing an improved input for a subsequent amplitude-versus-offset (AVO) analysis (Bancroft and Sun, 2003).

6.2 Minimum-aperture migration

The determination of the minimum migration aperture consists of two tasks: the constitution of the stationary point that defines the centre for the migration aperture and of the size of the projected Fresnel zone which controls its horizontal extension. The basic concept which holds for time and depth migration has been described by Jäger (2005a) for 2.5D prestack and poststack migration as
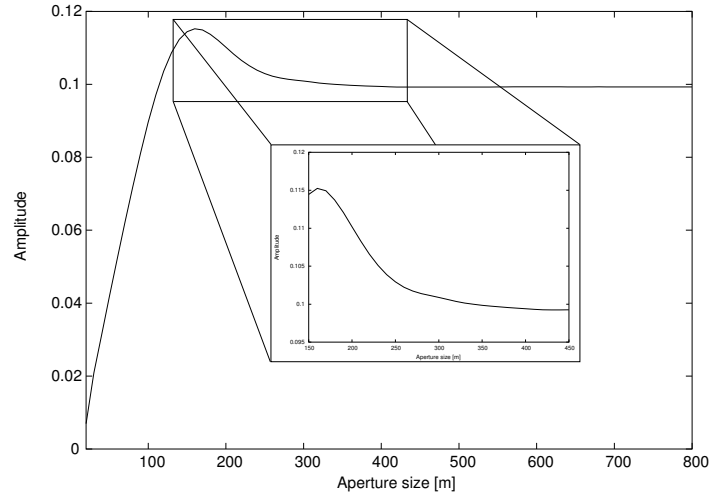
Figure 6.2: Effect of the migration aperture on the amplitudes for noise-free data. The projected Fresnel zone size is approximately 400 m. Apertures smaller than this size lead to meaningless amplitudes, the actual behaviour of the amplitudes in this case depends on the wavelet. In this example, the aperture is always centred around the stationary point.

well as for 3D poststack migration. The approach is reviewed here in a slightly different notation and the extension to the 3D prestack case is discussed.

6.2.1 Determination of the minimum aperture in 2.5D

Determination of stationary points

In Kirchhoff migration, the main contribution to the diffraction stack stems from the region where the reflection event is tangent to the migration operator, i.e., the vicinity of the stationary point. The condition of tangency can be conveniently expressed in terms of local slowness vectors $\mathbf{p}_D$ and $\mathbf{p}_R$ associated with the migration operator and the reflection event, respectively. Wherever in the prestack time domain these vectors coincide, we encounter a stationary point.

For zero offset, the slowness $\mathbf{p}_R$ is readily available from the CRS attributes. In the 2D case, it is sufficient to consider the horizontal slowness p_{Rx}:

$$p_{Rx} = \frac{1}{v_0} \sin \alpha \,. \tag{6.1}$$

For time migration with straight rays as considered here, the migration operator as well as its spatial derivatives like p_{Dx} are given by analytic expressions which allow an efficient implementation. In practice, the modulus of the difference between these two horizontal slownesses is calculated and the location of the minimum is regarded as stationary point P_0 for ZO. A minimum slowness difference threshold is defined to avoid the detection of minima which are not related to actual stationary points. By applying a further user-defined coherence threshold, the associated coherence values are used to decide whether the point is reliable.

By means of the approximated CRP trajectory (3.17), the location of the stationary point can be extrapolated to finite offsets. This provides an offset-dependent and, thus, more accurate reference for the centre of the migration aperture compared to the conventional approach which ignores the deviation between CMP and CRP gathers.

Estimation of the size of the projected Fresnel zone

The final information relevant for minimum migration apertures which can be obtained from the attributes is the size of the projected ZO Fresnel zone given in equation (3.19). In general, the Fresnel zone size is expected to vary with offset. Unfortunately, this effect is hard to quantify as the velocity model together with the dip and curvature of the reflector has to be considered. In principle, the curvature of the normal wave can be utilised to estimate this effect. But due to the inherent instability in the determination of this parameter, an approximation based on the normal wave curvature would be rather insecure.

However, forward-calculated examples suggest that for plane interfaces, the widening effect is small as can be seen from Figure 6.3: for two analytical models with different reflector depths the relative size of the projected Fresnel zone $W_F(h)/W_F(h = 0)$ is determined for three different reflector dips. As long as the the offset does not exceed the reflector depth, the relative widening is smaller than 10%. For practical applications, the ZO Fresnel zone size determined from the CRS attributes is always extended by a certain amount to account for the approximative manner of equation (3.19) as it is crucial not to underestimate the Fresnel zone for true-amplitude processing. In addition, the error in the approximation of the CRP trajectory has to be accounted for. The user-controlled widening factor depends on the quality of the CRS attributes and the reflector curvature. It turned out that a widening between 20% for not too strong reflector curvatures and up to 50% otherwise applied to the ZO projected Fresnel zone size usually covers all the mentioned effects. For the 2D examples discussed in Chapter 7, the ZO Fresnel zone was increased by a factor of 20% to 50% but kept constant with offset, an approximation which appears to be reasonably accurate to obtain reliable amplitudes for the considered models as can be seen from the comparison with the conventional results.

6.2.2 Determination of the minimum aperture in 3D

Determination of stationary points

The determination of the stationary point for offset zero can be performed analogously to the 2D case but now using the entire slowness vectors. In 3D, the slowness vector $\mathbf{p}_R$ associated with a ZO ray emerging at $(\mathbf{m}_0, \mathbf{h} = \mathbf{0}, t_0)$ with azimuth ϕ and dip α reads

$$\mathbf{p}_R(\mathbf{m}_0, t_0) = \frac{1}{v_0} (\cos\phi \sin\alpha, \sin\phi \sin\alpha, \cos\alpha) . \tag{6.2}$$

In the same way, the slowness vector $\mathbf{p}_D$ can be defined which is related to the migration operator $\tau_D(\mathbf{m}, M)$ for a depth point M. Evaluating $\mathbf{p}_D$ for location $\mathbf{m}_0$ yields

$$\mathbf{p}_D(\mathbf{m}_0, t_0) = \left(\left. \frac{\partial \tau_D}{\partial m_x} \right|_{\mathbf{m}=\mathbf{m}_0}, \left. \frac{\partial \tau_D}{\partial m_y} \right|_{\mathbf{m}=\mathbf{m}_0}, \sqrt{\frac{1}{v_0^2} - p_{D,x}^2 - p_{D,y}^2} \right) . \tag{6.3}$$
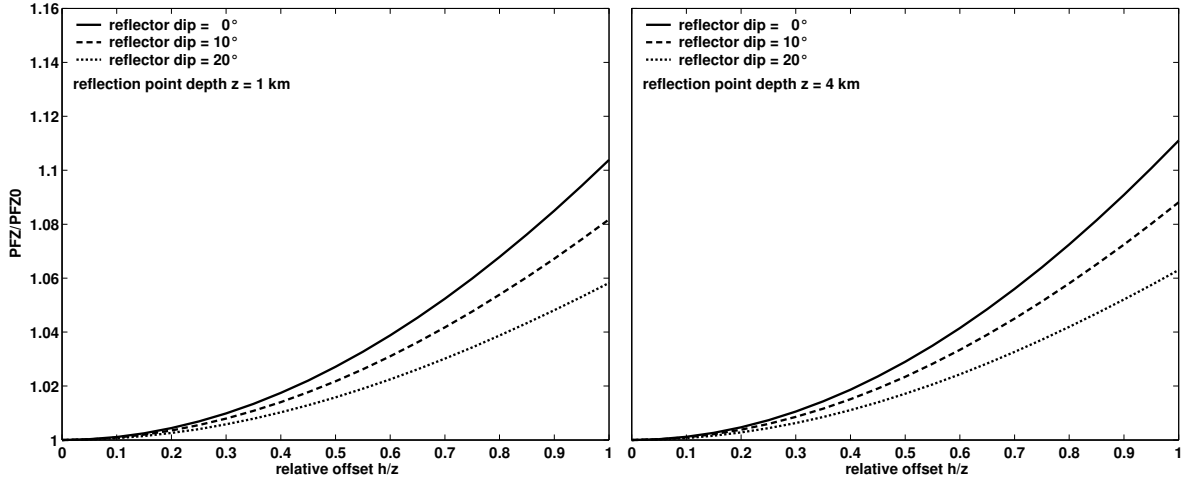
Figure 6.3: Relative size of the projected Fresnel zone $W_F(h)/W_F(h = 0)$ over relative offset h/z for plane interfaces with dips of $0°$, $10°$, and $20°$ beneath a homogeneous overburden. The considered reflection point is located at a depth of $z = 1000\,\text{m}$ (left) and $z = 4000\,\text{m}$ (right).

If the reflection event is tangent to the operator, the vectors $\mathbf{p}_D$ and $\mathbf{p}_R$ point in the same direction, i. e., the inner product between both normalised vectors is one. Thus, the stationary point can be found by determining the minimum of $1 - v_0^2\,|\mathbf{p}_D \cdot \mathbf{p}_R|$ for all samples encountered along the migration operator. Similar to the 2D case, a minimum slowness difference and coherence threshold is employed in practical applications to avoid false results associated with unreliable attributes.

In order to extrapolate the stationary point to finite offset, its offset-dependent displacement has to be considered. Unfortunately, the CRS-based approximation of the CRP trajectory cannot be fully generalised to 3D (see Section 3.3). For 1D media and a given offset azimuth γ, all rays pertaining to a common midpoint are situated in the vertical plane defined by γ. Thus, for a fixed offset azimuth, only a 3D subset of the 5D data space has to be considered, i. e., the 3D case is reduced to 2D. Thus, the direction of the dislocation of the stationary point is defined by the offset azimuth. As the wavefield attributes show no dependency on the offset azimuth for 1D media, the 2D approximation of the CRP trajectory can be fully employed to evaluate the absolute value of the dislocation.

For media with only small lateral velocity variations, the above considerations still hold approximately. In order to consider the same concept, the 2D CRP trajectory is estimated using the NIP wave radius and the dip evaluated in the direction given by the offset azimuth γ. This approach provides the general direction and approximate size of the dislocation rather than an exact position of the stationary point for finite offsets. Therefore, the estimated PFZ size for ZO should always be extended by a certain degree to compensate for the approximation. For general media, no such approximation in terms of the CRS attributes is available. In this case, the displacement of the stationary point can only be compensated by a heuristic widening of the aperture with increasing offset to ensure that the projected Fresnel zone is fully covered. As no dislocation of the stationary point can be considered here, the widening has to be significantly larger compared to the approach based on the CRP trajectory. With decreasing difference between minimum and conventional aperture, the approach becomes less attractive. Therefore, an application in the depth domain where arbitrary media are considered requires a different strategy, e. g., based on slant stacks in the common offset sections.
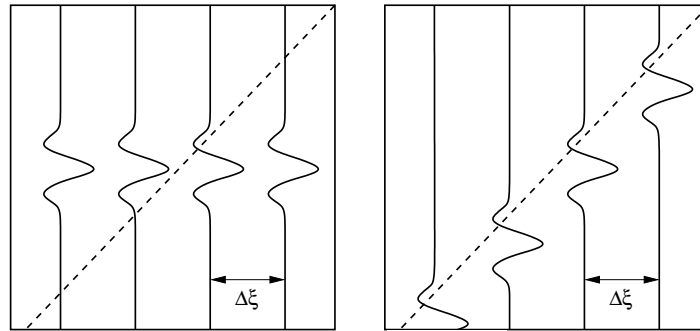
Figure 6.4: Left: operator aliasing occurs when the migration operator undersamples the wavelet outside the tangency region between migration operator and reflection event. In this case, the summation yields a non-negligible result. Right: no operator aliasing is encountered in regions where the operator is tangent to the reflection event.

Estimation of the size of the projected Fresnel zone

In 3D, the size of the ZO projected Fresnel zone can be approximated from the curvature matrices $\mathbf{K}_{\mathrm{NIP}}$ and $\mathbf{K}_{\mathrm{N}}$ using formula (3.18). The equation describes an ellipse in the midpoint plane which is centred at the stationary point ξ^*. The radii of the principal axes and their orientation can be immediately obtained by transforming the matrix $\left[\mathbf{H}(\mathbf{K}_{\mathrm{NIP}} - \mathbf{K}_{\mathrm{N}})\mathbf{H}^{\mathrm{T}}\right]$ into the principal axes system. The eccentricity and orientation of the ellipse resembles the azimuth dependency of the subsurface's properties. In conventional migration, a circular aperture is usually employed if no further information is available.

6.3   Migration aperture and operator aliasing

One advantage of minimum-aperture migration is the avoidance of operator aliasing. Unlike data-driven aliasing caused by improper temporal and spatial sampling of the input data, operator aliasing is related to the imaging process itself. Operator aliasing occurs when the moveout of the migration operator between two neighbouring traces exceeds half of the wavelet length. In this case, the operator undersamples the wavelet and, thus, aliases frequencies (see Figure 6.4). The resulting artifacts can severely degrade the migrated image.

Operator aliasing emerges in the steeper part of the migration operator as it depends on the operator dip. A widespread criterion to determine the maximum unaliased frequency f_{max} for 2D Kirchhoff migration reads

$$f_{\mathrm{max}} = \frac{1}{2\left|\frac{d\tau}{d\xi}\right|\Delta\xi}, \tag{6.4}$$

where $d\tau/d\xi$ denotes the local dip of the migration operator and $\Delta\xi$ the trace spacing. In 3D, f_{max} should be determined for the direction diagonal to the ξ_1- and ξ_2-axis as it better represents higher frequencies (for details see Abma et al., 1999, and references therein). Equation (6.4) strictly holds for horizontal reflection events, only. Otherwise, the maximum unaliased frequency depends on the dip difference between migration operator and reflection event (Baina et al., 2003).

Different approaches exist to handle operator aliasing in conventional Kirchhoff migration. In principle, restricting the dip of the migration operator avoids the effect but leads to a loss of steeply dipping events. Other techniques to suppress operator aliasing utilise trace interpolation or low-pass filtering. Both approaches are computational intensive and anti-alias filter additionally affect the migrated amplitudes. A comparison of different methods for operator anti-aliasing in Kirchhoff migration can be found in Abma et al. (1999).

In minimum-aperture migration amplitudes are only summed up in regions where the migration operator is tangent to the reflection events. Therefore, the problem of operator aliasing does not arise: the dip difference between both operators is always close to zero.

6.4 Further aspects of minimum-aperture migration

Reliability of stationary points and PFZ size

In Kirchhoff migration, each point on the output grid is treated independently. In the same way, the location of the stationary point and the size of the projected Fresnel zone are determined for each output location independently. Thus, the method strongly relies on the reliability and smoothness of the kinematic wavefield attributes. A stable determination and appropriate preconditioning of the CRS attributes is inevitable.

In general, the estimation of dip and azimuth by means of the CRS stack is expected to be rather stable which, therefore, allows a reliable determination of the stationary point. In contrast, the radius of the normal wave is usually the most unstable attribute. This may lead to unreasonable values for the size of the projected Fresnel zone. The effect on the migrated image is usually rather small, but the amplitudes clearly suffer. If stable attributes for the normal wave are not available, a plane normal wave approximation can be utilised for the projected Fresnel zone by setting $\mathbf{K}_N := \mathbf{0}$ in equation (3.18). However, this approach may lead to an underestimation of the Fresnel zone size for strongly curved reflectors. By means of the event-consistent smoothing introduced in Section 3.2, outliers and unphysical fluctuations which would deteriorate the minimum-aperture migration result can be removed from the attribute sections.

The number of locations for which a stationary point is found in the minimum-aperture approach is controlled by the user-given coherence threshold. Ideally, a reliable stationary point can be detected for each sample on an actual reflection event. In real data applications, this situation is rather unrealistic and stationary points are mostly detected on strong reflection events. Decreasing the coherence threshold increases the number of detected stationary points, but may cause artifacts as unreliable attributes are considered. In practice, a compromise between coverage and reliability of the stationary points has to be found. This point will be further considered in the real data examples shown in Chapters 7 and 8.

Transition from limited to conventional aperture

In real data applications, the target area cannot be expected to be completely covered with stationary points. In this case, the conventional aperture can be utilised at all locations where no stationary point was found to avoid gaps in the migrated image. This proceeding leads to local jumps in the aperture

size. However, if the conventional aperture is chosen sufficiently large to fully cover the size of the projected Fresnel zone, the results from the different aperture definitions differ only with regard to the noise level. Of course, prerequisite is that the location of the stationary point and the projected Fresnel zone size in the minimum-aperture approach are determined from reliable wavefield attributes.

Ambiguities in the input and output domains

Special situations arise if reflection events intersect each other or become tangent to each other in the unmigrated stacked domain. The first case is well known as conflicting dip situation, whereas the second might be termed conflicting curvature situation. In principle, both cases can be handled in CRS processing by allowing multiple attribute sets for a given ZO location. The main problem is to identify such locations. Due to the inherent instability of the normal wave curvature, conflicting curvatures situations can hardly be detected in a reliable way. For conflicting dip situations, the usually very stable dip parameter allows to identify such locations to a certain extent.

In case of successfully detected conflicting dip situations, the multiple attribute sets can be fully exploited by the limited-aperture migration approach: the search for the stationary point is simply performed for all available attribute sets. In general, each attribute set will yield a different stationary point related to different migration output locations. Although this aspect is not negligible, the explicit handling of conflicting dip situations in CRS processing is often omitted in practical applications as the choice of appropriate processing parameters is rather difficult.

In correspondence to the ambiguities in the input domain, we can also encounter ambiguities in the output domain, i. e., a migration operator with several stationary points. In the extreme case, an unlimited number of stationary points exists if a diffraction response is considered that coincides with the migration operator. In principle, similar numerical concepts as in the CRS conflicting dip handling can be applied in the minimum-aperture migration to identify multiple stationary points. However, this also immediately implies that the same instability and tendency to introduce artifacts can be expected. Therefore, the current implementation of the limited-aperture migration only considers one stationary point per ZO migration operator.

6.5   Summary

In this chapter, a time domain approach for minimum-aperture migration based on the kinematic wavefield attributes was presented. In order to restrict the migration operator to the region where it is tangent to the reflection event, the location of the stationary point, its variation with offset, and the size of the projected Fresnel zone have to be known. While in 2.5D all required information is directly available from the CRS attributes, the concept cannot be fully generalised to 3D. For media showing mild to moderate lateral velocity variations as usually considered in time migration, an adapted strategy similar to the 2.5D case can be utilised. However, an extension to more general situations is not possible in the scope of the CRS-based approach.

Chapter 7

Minimum-aperture Kirchhoff time migration: 2D results

As part of this thesis, a true-amplitude Kirchhoff time migration was implemented for minimum-aperture as well as conventional migration. Both migration algorithms utilise the straight-ray approximation and the consistent constant velocity weight. In this and the subsequent chapters, the minimum-aperture migration is tested on 2D and 3D synthetic and real data examples and the results are compared to the results obtained by migration with conventional user-controlled aperture. Since the same implementation was used in both migration schemes, the image quality and reliability of the migration amplitudes provided by the minimum-aperture and the conventional approach can be directly compared. Both the synthetic and the real datasets resemble typical examples for the application of time migration. While in the real data application the main focus is on the image quality, the synthetic data additionally allows to test the quality of the dynamic results and, thus, the potential of the minimum-aperture approach for AVO analysis.

7.1   Synthetic data example

The synthetic prestack dataset was generated by means of dynamic ray tracing using the model shown in Figure 7.1. A marine acquisition geometry was employed with a shot spacing of 20 m and a receiver spacing of 10 m; the maximum full offset is 2000 m. The target region for the amplitude analysis is the horizontally layered structure beneath the uppermost dome-like interface. The elastic parameters are chosen such as to mimic a sequence of gas/oil/water contacts, see Table 7.1.

Intercept and gradient for the contacts were calculated according to the Shuey approximation of the Zoeppritz equation given in equation (4.36). The primary P-waves were modelled by means of a wave-front construction method using a zero-phase Ricker wavelet with a dominant frequency of 40 Hz. The temporal sampling in the dataset is 4 ms. Edge diffractions and transmission losses were not considered in the modelling. A representative common-offset section of the forward-modelled data is displayed in Figure 7.2a). Coloured noise with two different S/N ratios was added to the prestack data.

Layer	v_P [m/s]	v_S [m/s]	ρ [kg/m^3]
Gas	2500	1575	2180
Oil	2900	1720	2130
Water	3100	1790	2330
Basement	3050	1525	2255

Contact	R_0	G
Gas/oil	0.103	-0.100
Oil/water	0.038	-0.027
Water/basement	-0.024	0.196

Table 7.1: Elastic parameters of the target zone (top): P-wave velocity v_P, S-wave velocity v_S, and density ρ. Corresponding AVA parameters (bottom): intercept R_0 and gradient G.
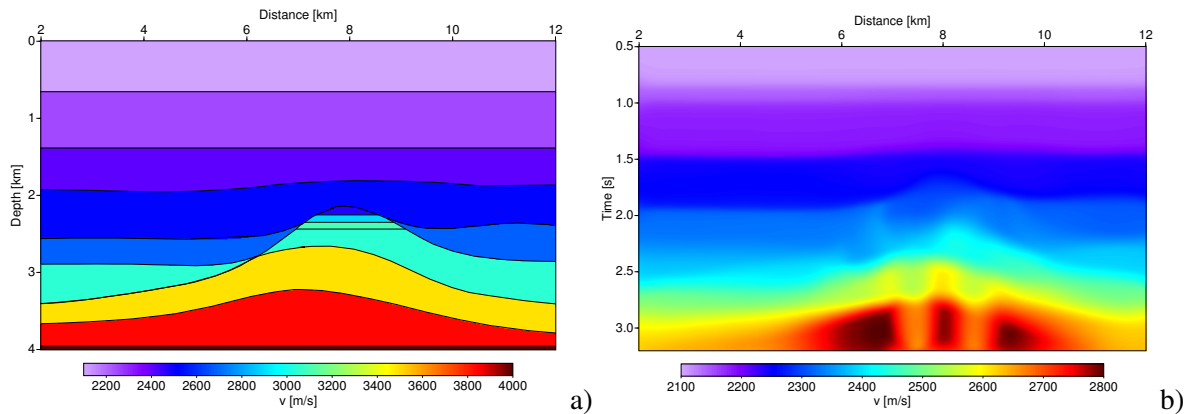
Figure 7.1: a) Interval P-wave velocity model used to generate the synthetic data and b) time migration velocity model determined from CRS wavefield attributes. Note the different scales.
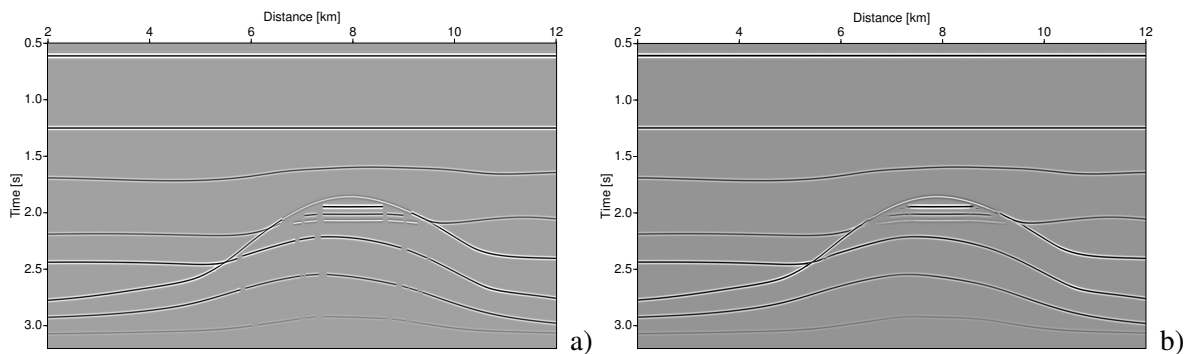
Figure 7.2: a) Representative common-offset section ($h = 100$ m) extracted from the synthetic prestack data. Modelling artifacts like gaps and jumps in the amplitudes are visible in the lower part of the seismogram. b) ZO stacked section obtained by means of the CRS stack. The gaps are partly closed by the stacking process.
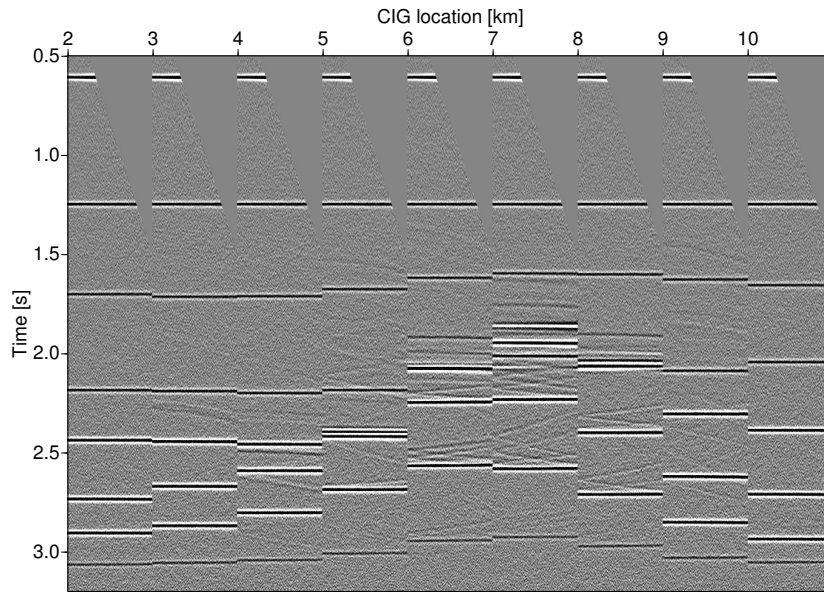
Figure 7.3: Several common-image gathers extracted from the time-migrated prestack data. Maximum full offset is 2000 m. The horizontal axis denotes the CIG locations.

7.1.1 CRS stack and model building

The CRS stack was applied to the dataset with the lower S/N-ratio to simulate the ZO section (Figure 7.2b)) which entered into the poststack migration. Due to the applied spatial stacking operator, the gaps visible in the forward-modelled seismogram are partly closed. In addition, a set of CRS wavefield attribute sections and the associated coherence section (not displayed) were obtained. For the further applications in the velocity model building and the minimum-aperture migration, the wavefield attributes were smoothed using the event-consistent smoothing routine (see Section 3.2).

Based on the coherence values, (reliable) sets of attributes were extracted on the reflection events and converted to time migration velocities and apex locations (see Figure 5.3 and the corresponding comment for details). The interpolated smooth time-migration velocity model is shown in Figure 7.1b). The model is kinematically consistent with the data as can be seen from the set of common-image gathers (CIGs) displayed in Figure 7.3: no residual moveout is visible.

7.1.2 Poststack migration

With the attribute-based migration velocity model, the poststack time migration was performed twice: on the one hand in a conventional way with user-controlled aperture, on the other hand with the minimum aperture given by the projected Fresnel zone. The user-given aperture was chosen such that the steep flanks of the dome-like structure were imaged. In both migration schemes, a cosine-square taper was applied between the first and the second projected Fresnel zone to avoid artifacts otherwise caused by the abrupt truncation of the operator. The midpoint displacement of the stationary point with respect to the apex of the migration operator is displayed in Figure 7.4a). Locations where no stationary point was detected are masked. The midpoint displacement depends solely on the dip of
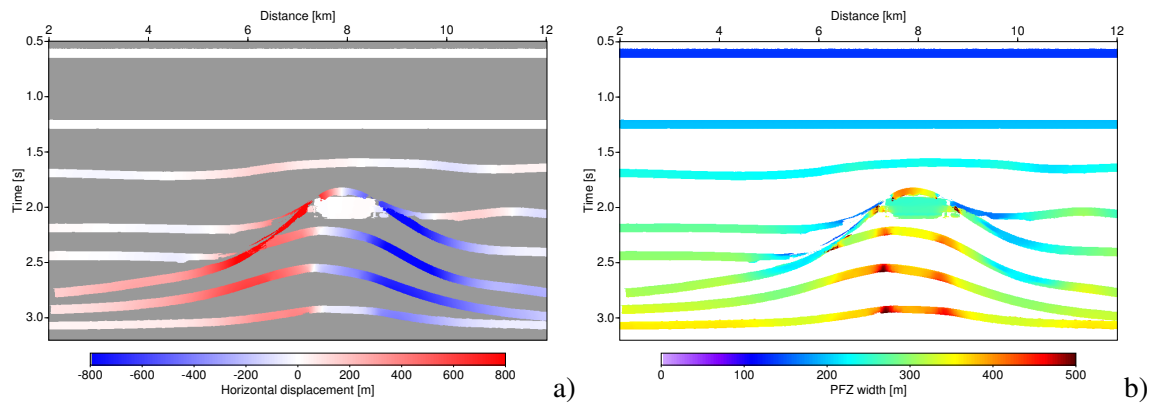
Figure 7.4: a) Horizontal displacement of the stationary points with respect to the operator apex. b) Size of the projected first ZO Fresnel zone estimated from the CRS attributes. Only locations with identified stationary points were considered.

the reflection event and reaches its maximum value at the steep flanks of the dome. The associated size of the projected Fresnel zone is shown in Figure 7.4b). The estimated ZO Fresnel zone size was increased by 50%. As expected, the size of the projected Fresnel zone increases with increasing traveltime and increasing curvature of the reflection events, where the latter has to be considered as signed property with positive sign for events appearing concave when viewed from the acquisition surface.

The poststack migration results are shown in Figure 7.5. The minimum-aperture migration was only performed at locations where stationary points were detected. This removes many of the artifacts due to modelling deficiencies but can, in turn, cause gaps, e. g., in conflicting dip situations or on weak events where no reliable attributes are available. In practice, the user-given aperture would be used at all other locations to obtain a fully covered image without gaps.

7.1.3 Prestack migration

In the same way as in the poststack case, two prestack migrations were carried out on the full prestack datasets. The migrated images obtained for the dataset with the higher noise level are shown in Figure 7.6. The aperture size was chosen as in the corresponding poststack migration, an offset-dependent widening of the aperture was not considered. In case of the minimum-aperture migration, the location of the stationary point was extrapolated to finite offsets using the approximated CRP trajectory. As in the poststack case, the minimum-aperture migration was only performed for detected stationary points.

Again, a significant reduction of the artifacts can be observed in the minimum-aperture result (Figure 7.6 b)) whereas some gaps are introduced in the reflection events where no stationary point could be detected. These gaps could be closed by applying the user-given aperture at all locations where no stationary point was found.

Finally, the amplitudes along the migrated reflection events of the target reflectors were extracted for both prestack migrated datasets. The offsets were mapped to reflection angles θ assuming horizontal
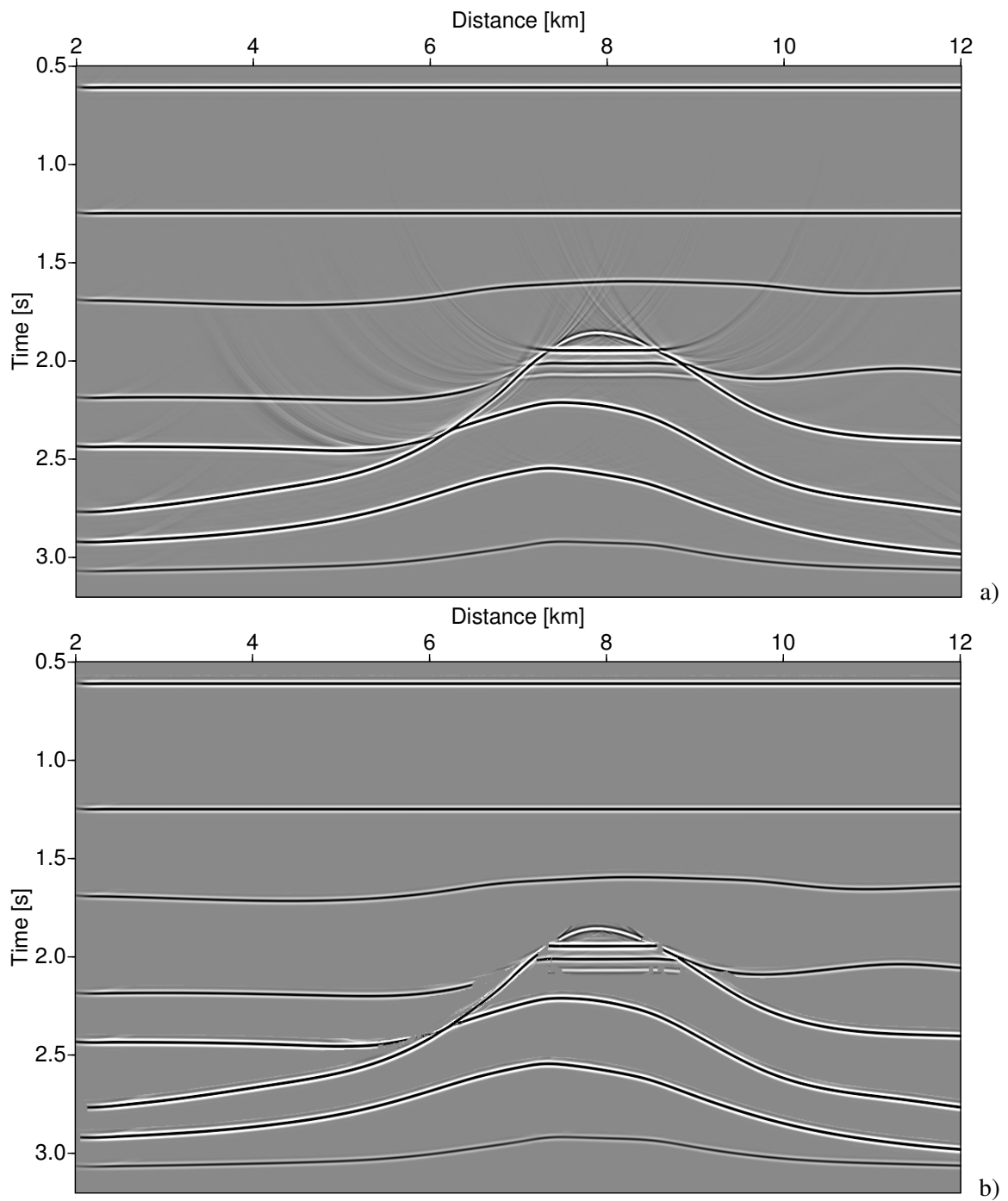
Figure 7.5: Poststack migration results migrated with (a) conventional user-defined aperture and (b) CRS-based minimum-aperture. In the latter case, only locations with identified stationary points were considered. Migration artifacts are strongly reduced in the minimum-aperture result.
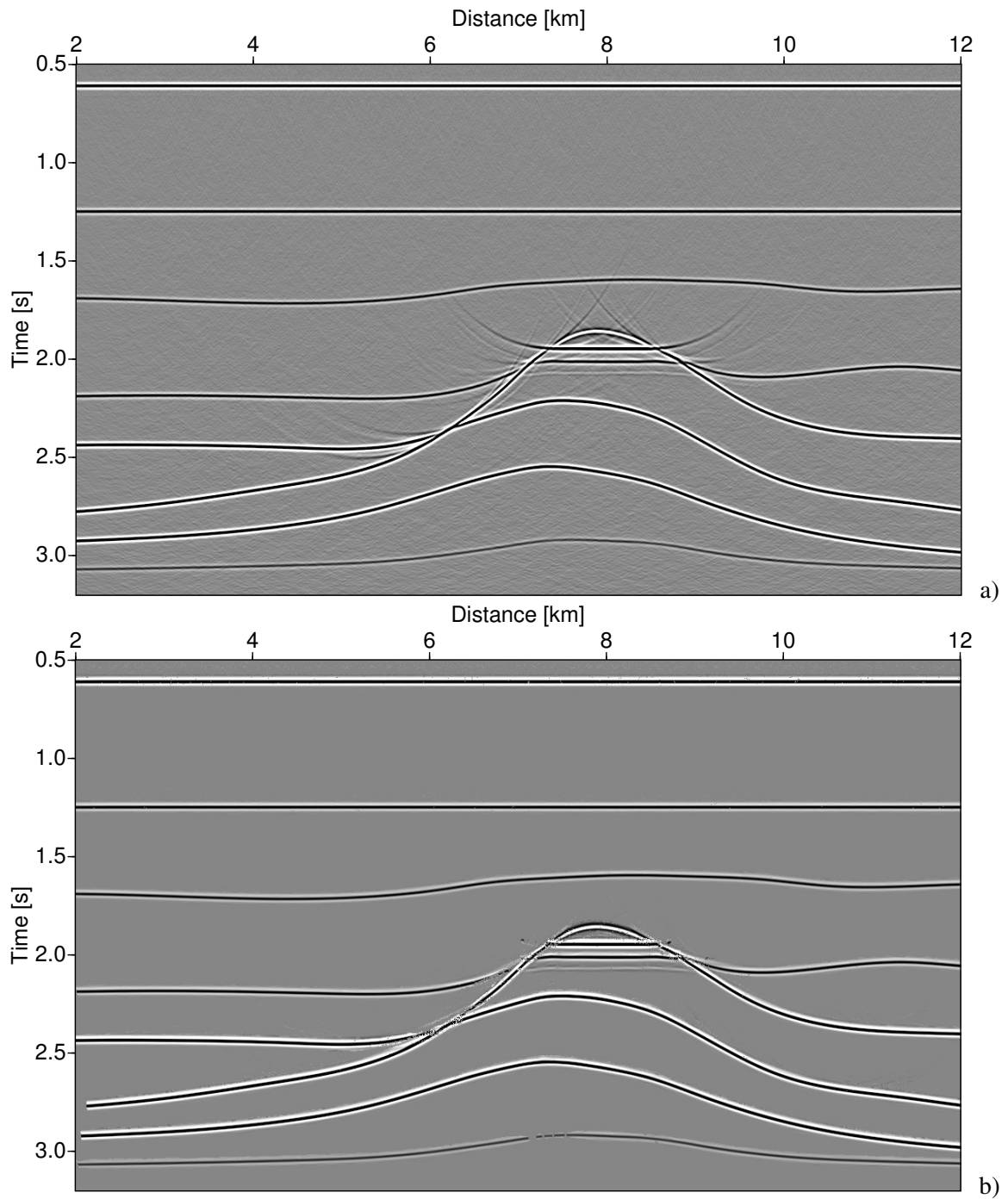
Figure 7.6: Stacks of the time-migrated prestack data with (a) conventional user-defined aperture and (b) CRS-based minimum-aperture. Again, the migration was only performed for locations where a stationary point was detected.

reflectors with a homogeneous overburden. Reflection angles over $35°$ were not considered. Figure 7.7 shows the AVA curves for one selected common-image gather for both aperture definitions applied to the data with low noise level. In addition, the minimum-aperture migration was applied to the same data without noise to obtain reference values. The conventional results basically suffer from migration artifacts intersecting the target reflection events. In Figure 7.8 the same results are shown for a higher noise level. Here, we observe far less scattering of the amplitude values in the CRS-based limited aperture results.

For each target reflection event and noise level, the extracted amplitudes were used to generate horizon-based AVA crossplots (Figures 7.9 and 7.10) based on a stable linear regression method (Walden, 1991). Again, the noise-free dataset was utilised to obtain reference values. In general, the migration results for the noisy data show an elliptic distribution of the points around these reference values depending on the S/N ratio of the considered reflection event (which decreases from top to bottom). If migration artifacts or different events contribute to the diffraction stack as, e. g., in case of the uppermost target reflector, the overall trend in the AVA curve is biased. In this case, a wrong trend can be introduced in the crossplot or the linear regression might even totally fail. Due to the decreased noise-level in the amplitudes, the CRS-based results show less dispersion and give an overall better estimation of the forward-calculated reference values shown in Table 7.1. The deviation in the intercept R_0 can be explained by the utilised straight ray approximation which enters into the calculation of the true-amplitude migration weights.

7.2 Real data example

The 2D seismic land dataset used for the case study was acquired by an energy resource company in a fixed-spread geometry. The seismic line had a total length of about 12 km. The utilised source signal was a linear upsweep from 12 to 100 Hz of 10 s duration. Shot and receiver spacing are both 50 m and the temporal sampling interval is 2 ms. Standard preprocessing was applied to the field data including the setup of the data geometry, trace editing, deconvolution, geometrical spreading correction, field static correction, and bandpass filtering. As the amplitudes were not preserved during these processes, the data is not suited to recover reflection amplitudes. Hence, the migrated amplitudes can only be interpreted in a qualitative way.

7.2.1 CRS stack and model building

The CRS stack was carried out on the preprocessed dataset; conflicting dip situations were not considered. In an initial step, the three kinematic wavefield attributes were searched for independently. The obtained attributes were smoothed and used as starting values in a local three-parameter optimisation. Afterwards, a second event-consistent smoothing was applied to remove remaining outliers and to precondition the attribute sections for the following steps. The simulated ZO section is displayed in Figure 7.11. The coherence section together with the smoothed attributes α, R_{NIP}, and $K_N = 1/R_N$ is shown in Figure 7.12. Attributes associated with low coherence values are masked out in the sections.

For the determination of the time migration velocity model, the smoothed attributes associated with the reflection events were extracted and converted to time migration velocities. The interpolated velocity model is displayed in Figure 7.13a), the pick locations are shown as overlay. No reliable picks
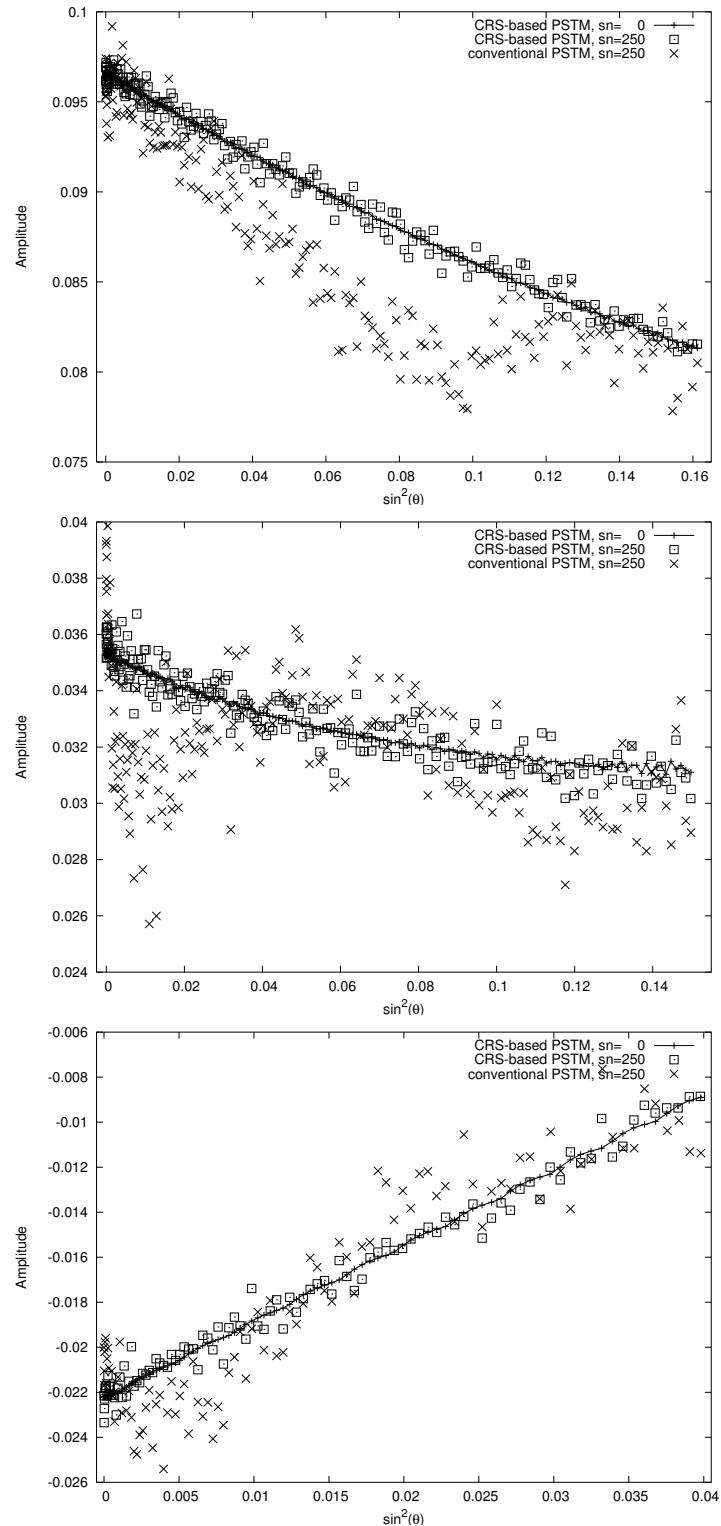
Figure 7.7: AVA curves for a selected CIG along the target reflection events for the dataset with low noise level. In particular the uppermost AVA curve suffers from migration artifacts in the conventional result. The reference values were obtained by CRS-based migration of noise-free data. Only under-critical reflection angles were considered.
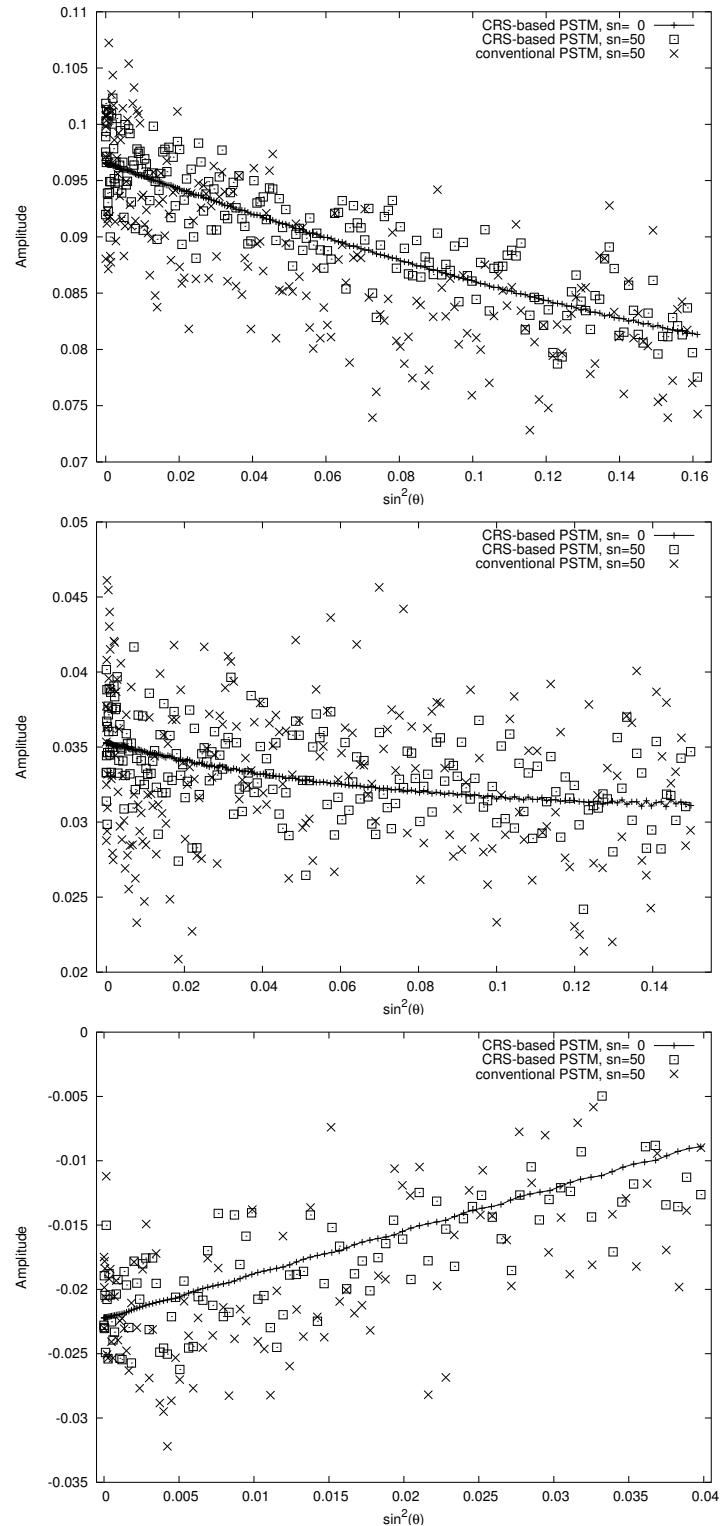
Figure 7.8: AVA curves for a selected CIG along the target reflection events for the dataset with high noise level. The amplitude variance in the CRS-based result is far lower compared to the conventional result. The reference values were obtained by CRS-based migration of noise-free data. Again, the reflection angles are restricted to under-critical values.
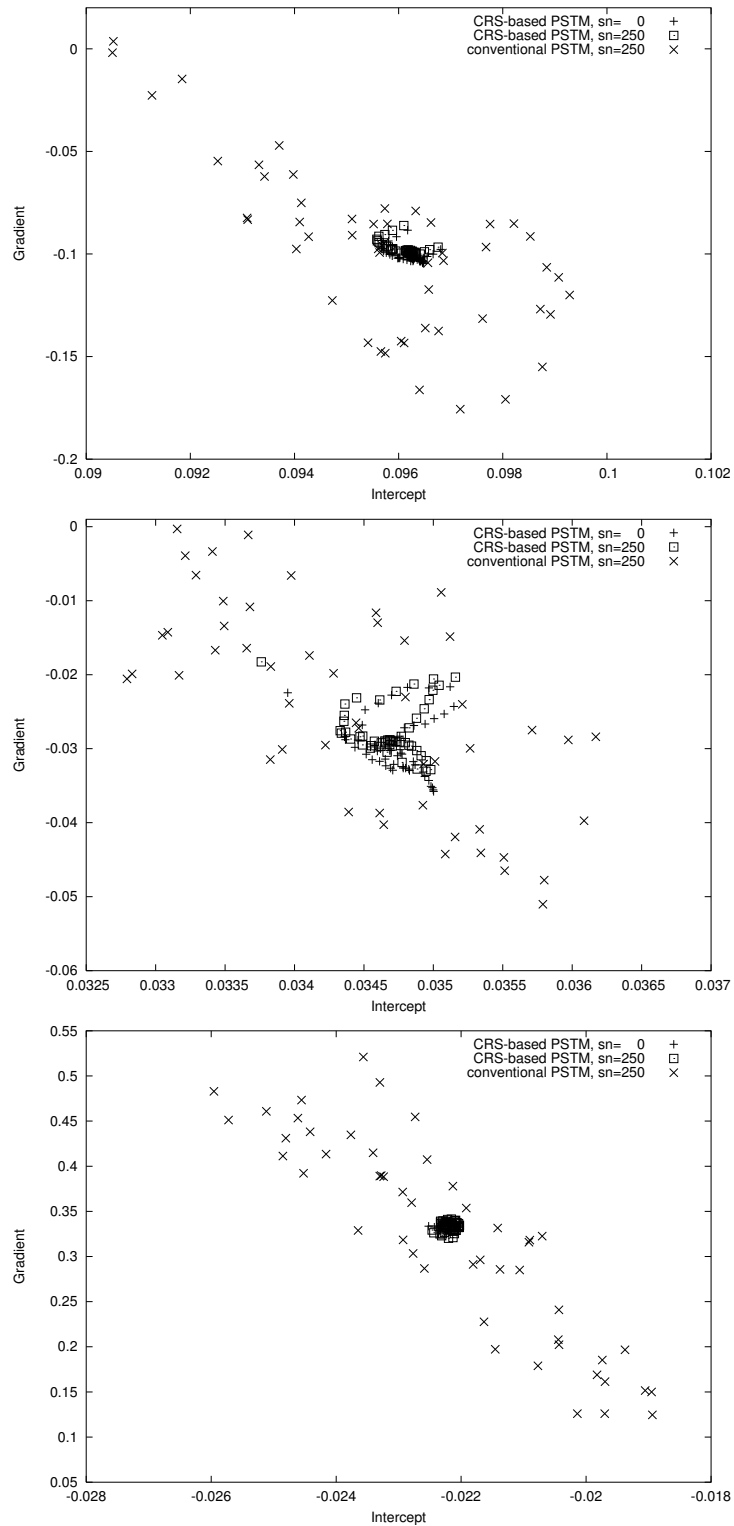
Figure 7.9: Horizon-based AVA intercept vs. gradient crossplots for the three target reflection events extracted from the dataset with low noise level. Again, the noise-free result serves as reference. The forward-calculated counterpart is given in Table 7.1. Note the different scales of the axes chosen to achieve maximum display resolution.
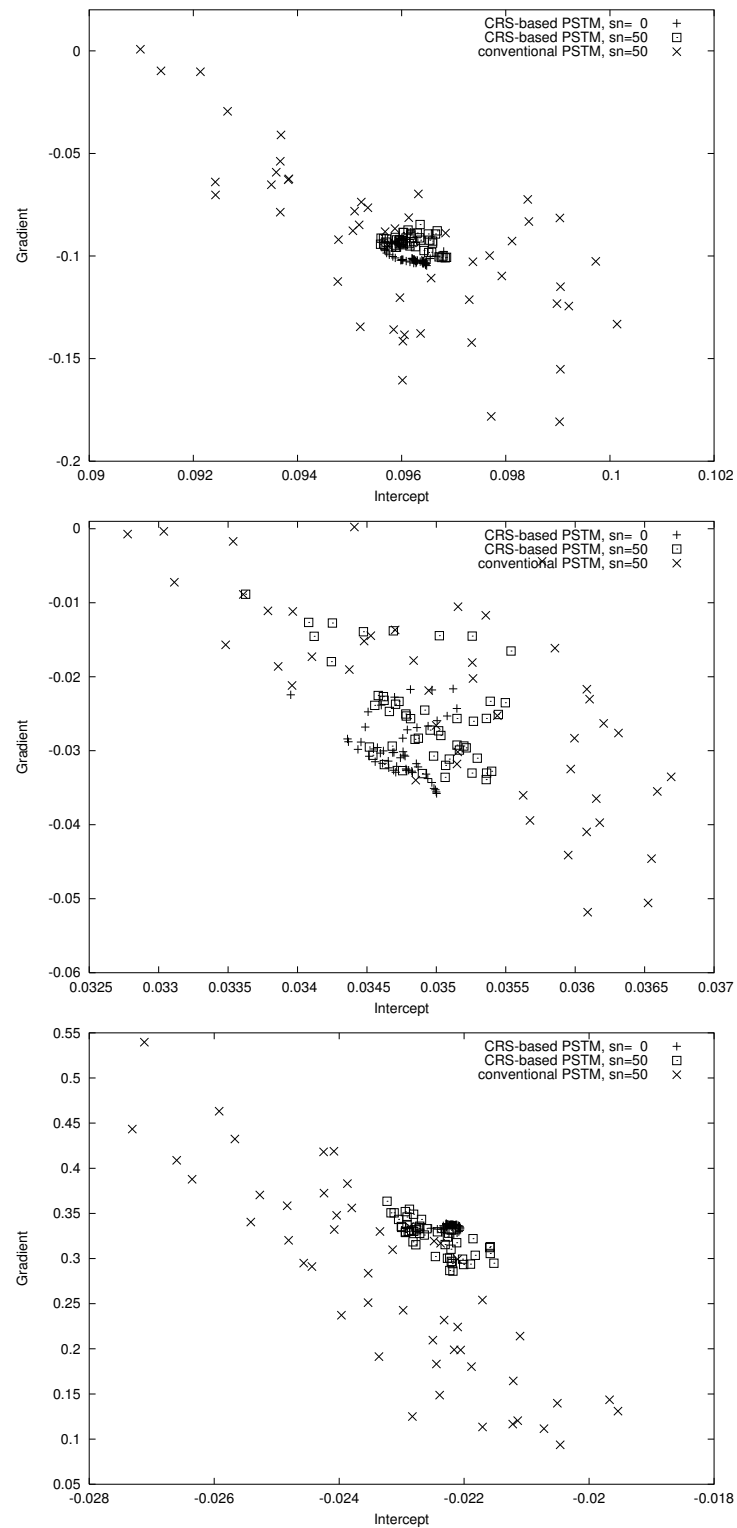
Figure 7.10: Horizon-based AVA intercept vs. gradient crossplots for the three target reflection events extracted from the dataset with high noise level. The noise-free result provides the reference values. Again, different scales of the axes were chosen for display.
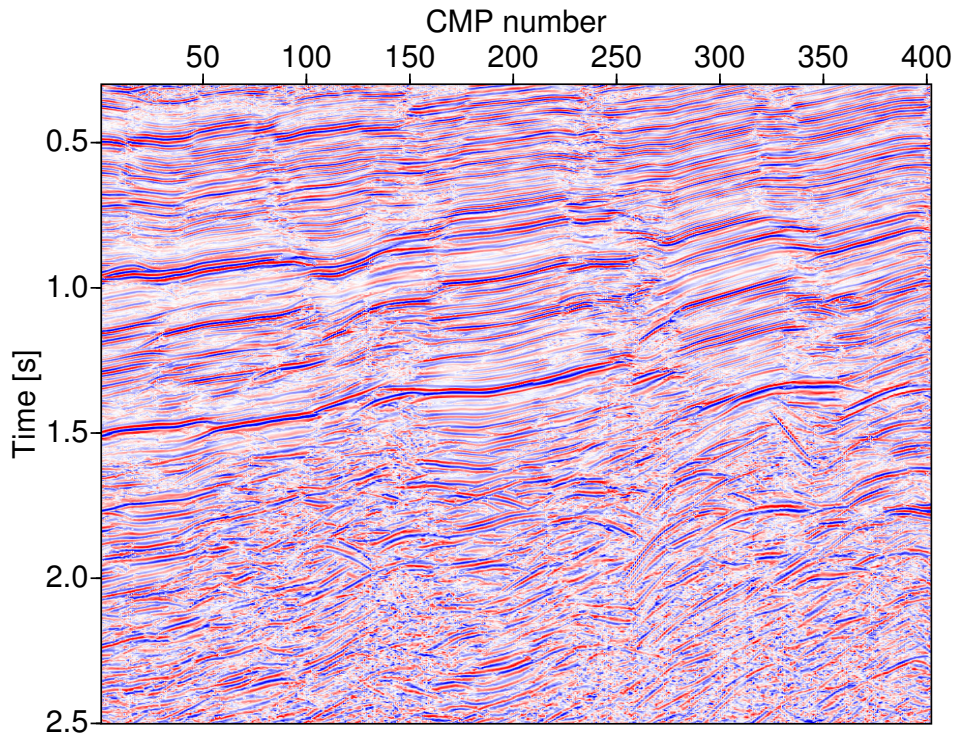
Figure 7.11: CRS-stacked ZO section. An automatic gain control was applied to amplify deep events.

could be extracted for traveltimes beyond 2 s. The subsurface shows approximately a 1D velocity distribution and, thus, is well suited for time migration. Selected common-image gathers are depicted in Figure 7.13b). The residual moveout in the gathers is most likely related to the utilised straight ray approximation. Hereby, the ray bending caused by the strong vertical velocity gradient is not taken into account.

7.2.2 Poststack migration

The minimum-aperture poststack migration was carried out on the ZO stacked section using the smoothed attribute sections. The target zone has a spatial sampling of 10 m and a temporal sampling of 2 ms. For real data applications, the quality and the reliability of the minimum-aperture result depend on the choice of an appropriate coherence threshold. In Figure 7.14, close-ups of migrated ZO sections obtained for three different coherence thresholds are depicted together with the associated mask sections that indicate locations were stationary points are detected. Decreasing the coherence threshold leads to an increase in the number of detected stationary points. The high coherence threshold in the uppermost examples only applies to the dominant reflectors, in all other locations the conventional aperture has to be used to avoid an image without gaps. These regions are characterised by an increased noise level. Choosing a coherence threshold of 0.01 leads to an almost complete coverage with stationary points. For this data example, no artifacts caused by unreliable attributes are visible. Nevertheless, the migrated image shows deteriorated reflection events as the attributes associated with the very low coherence values could not be smoothed properly. For the poststack and
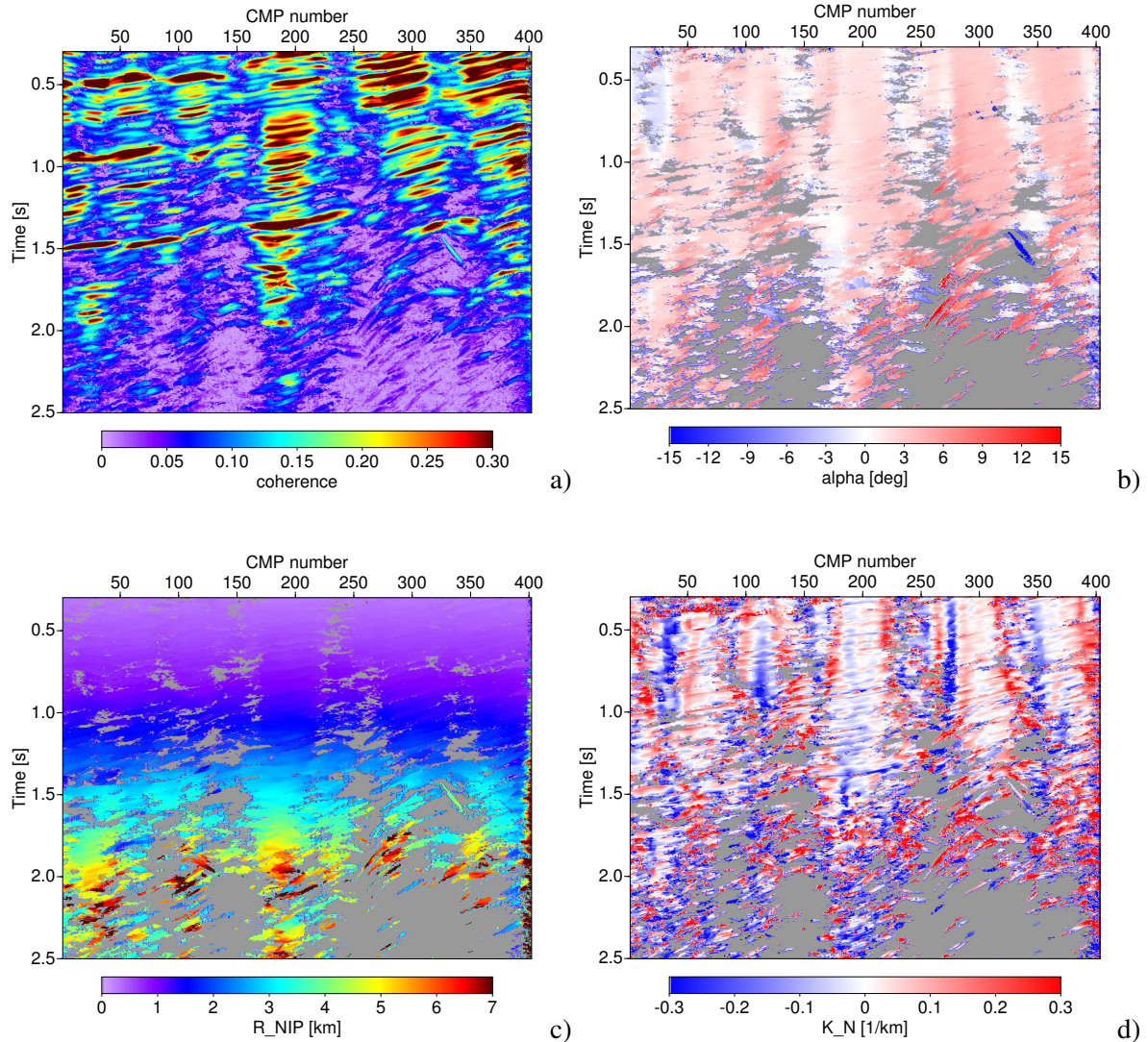
Figure 7.12: a) Coherence section and sections of the kinematic wavefield attributes (b) α, (c) R_{NIP}, and (d) $K_{\mathrm{N}} = 1/R_{\mathrm{N}}$. An event-consistent smoothing was applied to the attribute sections to remove outliers. Unreliable attributes associated with low coherence values are masked out.

prestack migration discussed in the following, the coherence threshold was set to the medium value of 0.05 which coincides with the threshold utilised in the event-consistent smoothing.

The horizontal displacement of the stationary points with respect to the operator apex for ZO is shown in Figure 7.15a), the associated half-width of the projected ZO Fresnel zone in Figure 7.15b). Both attributes are only displayed at locations where stationary points were detected. With the chosen coherence threshold of 0.05, a stable determination of stationary points and the corresponding projected Fresnel zone size was possible for almost the whole target zone. At all other locations, the conventional aperture (described below) was applied. In correspondence to the subsurface structure, the horizontal displacement increases up to 500 m in the lower part of the dataset where the reflection events become steeper. The Fresnel zone size, which was enlarged by 20% with respect to the values
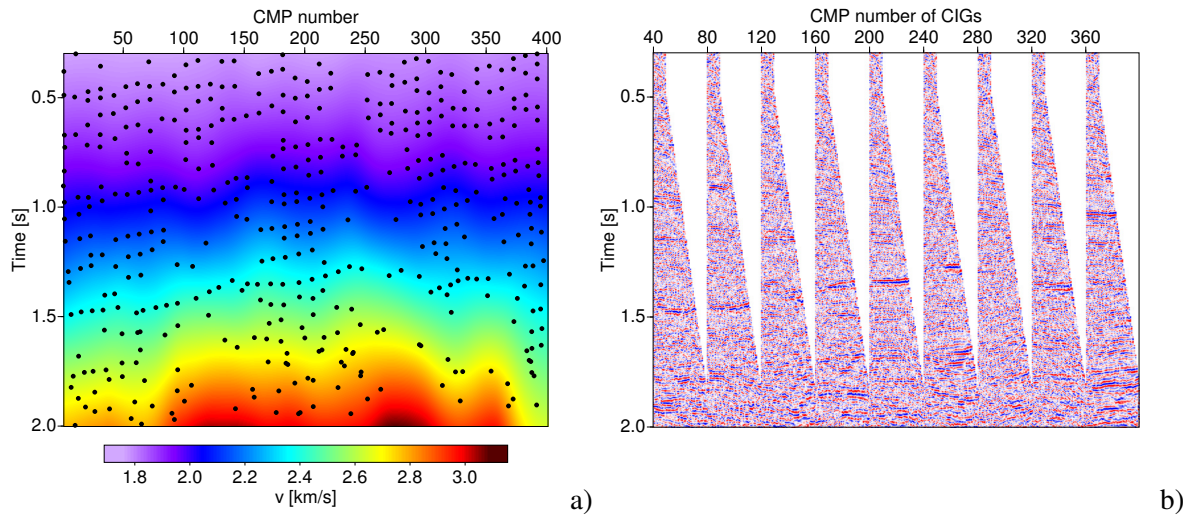
Figure 7.13: a) Smoothed time migration velocity model derived from the wavefield attributes. The black dots indicate pick locations. b) Selected common-image gathers extracted from the migrated prestack data. The maximum full offset is 2000 m. The CMP numbers indicate the CIG locations.

determined from the CRS attributes, increases with increasing traveltime up to 800 m. The high values for the Fresnel zone size determined beyond 1.5 s are related to (fragments of) diffraction events which, theoretically, have an infinite projected Fresnel zone. In conflicting dip situations, only the attribute set associated with the stronger event was available and was used in the determination of the minimum aperture (see, e. g., the reflection event between CMP 300 and 350 which shows positive horizontal displacement). The migrated section is displayed in Figure 7.16. Here and in the following migration results, an automatic gain control was applied for display.

A second poststack migration was conducted in a conventional way with a user-controlled aperture centred around the operator apex (Figure 7.16). The aperture increases linearly from 100 m at 0.3 s to 2000 m at 2.0 s. In both conventional and minimum-aperture migration, the same taper was applied to avoid artifacts related to the boundary of the migration aperture. The minimum-aperture migration result shows a better image quality and more contiguous events compared to the conventionally obtained poststack migration result. The noise level is significantly reduced at all locations where a stationary point could be detected and faults are better defined. The operator aliasing present in the shallow part of the conventional migration result is avoided in the minimum-aperture result as the summation is restricted to the tangency region between migration operator and reflection event. Evidently, the application of an anti-alias filter would clearly improve the conventional result. Note that the transition between conventional and minimum aperture in Figure 7.16 is only characterised by a different noise level.

7.2.3 Prestack migration

In Figure 7.17a) and Figure 7.17b), the corresponding prestack migration results are depicted. For both migration approaches, the aperture was kept constant with offset due to the small curvature of the reflection events. Whereas the conventional aperture is still centred around the operator apex for
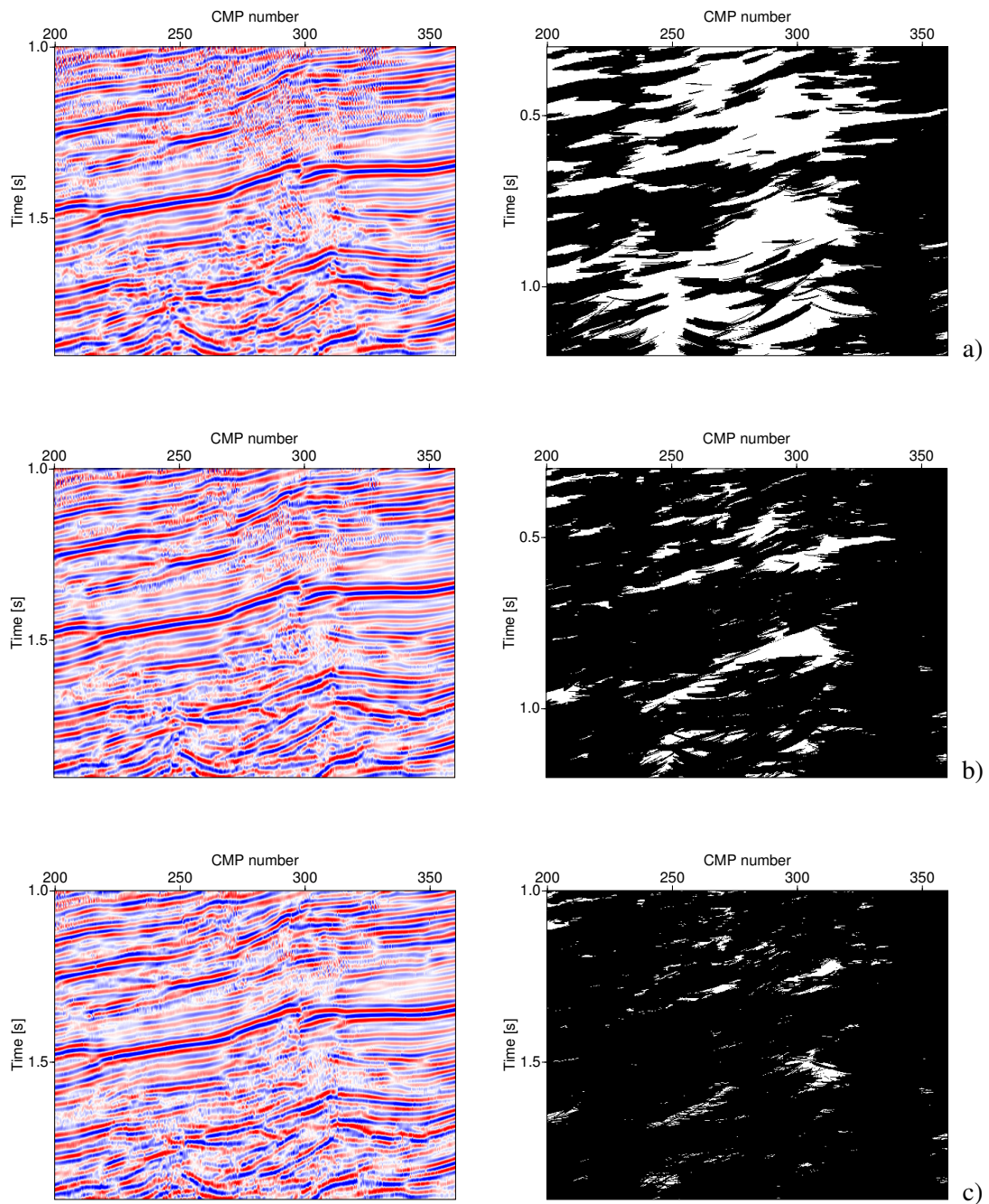
Figure 7.14: Minimum-aperture results obtained for coherence thresholds of 0.1, 0.05, and 0.01 (top to bottom). Close-ups of the migrated poststack sections are depicted in the left column. The associated mask sections are shown on the right, detected stationary points are indicated in black. At all other locations, the conventional migration aperture was employed; these regions are clearly associated with an increased noise level. Decreasing the coherence threshold leads to an increasing number of detected stationary points, but may lead to a distorted image when unreliable or fluctuating attributes are used.
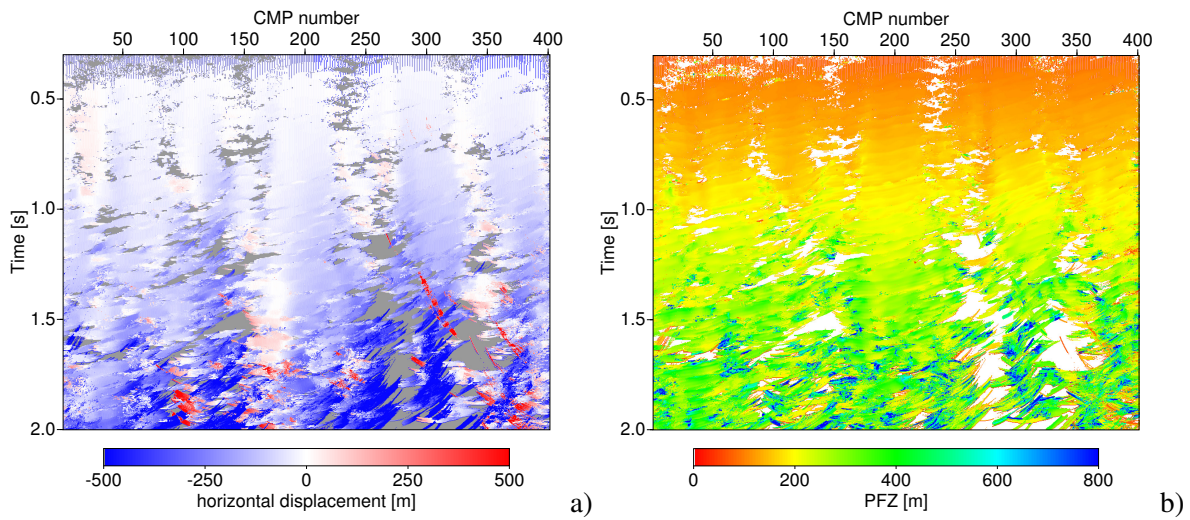
Figure 7.15: a) Horizontal displacement of the stationary point with respect to the migration operator apex. b) Half-width of the estimated projected Fresnel zone. Due to the high quality of the CRS attributes for these data, stationary points and the corresponding Fresnel zone size could be determined for almost the entire section.

all offsets, the CRS-based approximation of the CRP trajectory is utilised to extrapolate the location of the stationary point to finite offsets starting from the detected location for ZO.

Compared to the poststack results, more detailed subsurface structures can be observed but also an increased noise level. The latter is due to the fact that the CRS-stacked section used for the poststack migration already has a significantly increased signal-to-noise ratio. Nevertheless, the differences between the conventional and the minimum-aperture migration results show a similar behaviour as in the poststack case: a better definition of the faults and more distinctive reflection events in many areas can be seen in the minimum-aperture result. Again, operator aliasing is present in the conventional result and the migrated image shows a higher overall noise level.

Finally, amplitudes were extracted from both prestack migration results for the strong reflection event at 1.3 s between CMP nos. 150 and 250. A representative AVO curve is depicted in Figure 7.18. The fluctuations in the curves are due to the noise level in the input data. However, the summation of noise outside the tangency region is omitted in the migration process which also reduces the scattering in the migrated amplitudes.

7.3 Summary

In this chapter, the potential of the 2D minimum-aperture time migration approach was tested on a synthetic as well as on a real dataset. In both cases, the kinematic wavefield attributes obtained by means of the CRS stack entered into the derivation of the time migration velocity model and the determination of the minimum migration aperture. By restricting the migration aperture, operator aliasing is omitted, migration artifacts are suppressed, and noise outside the tangency region does not contribute to the summation. Compared to conventional approaches with user-given, apex-centred
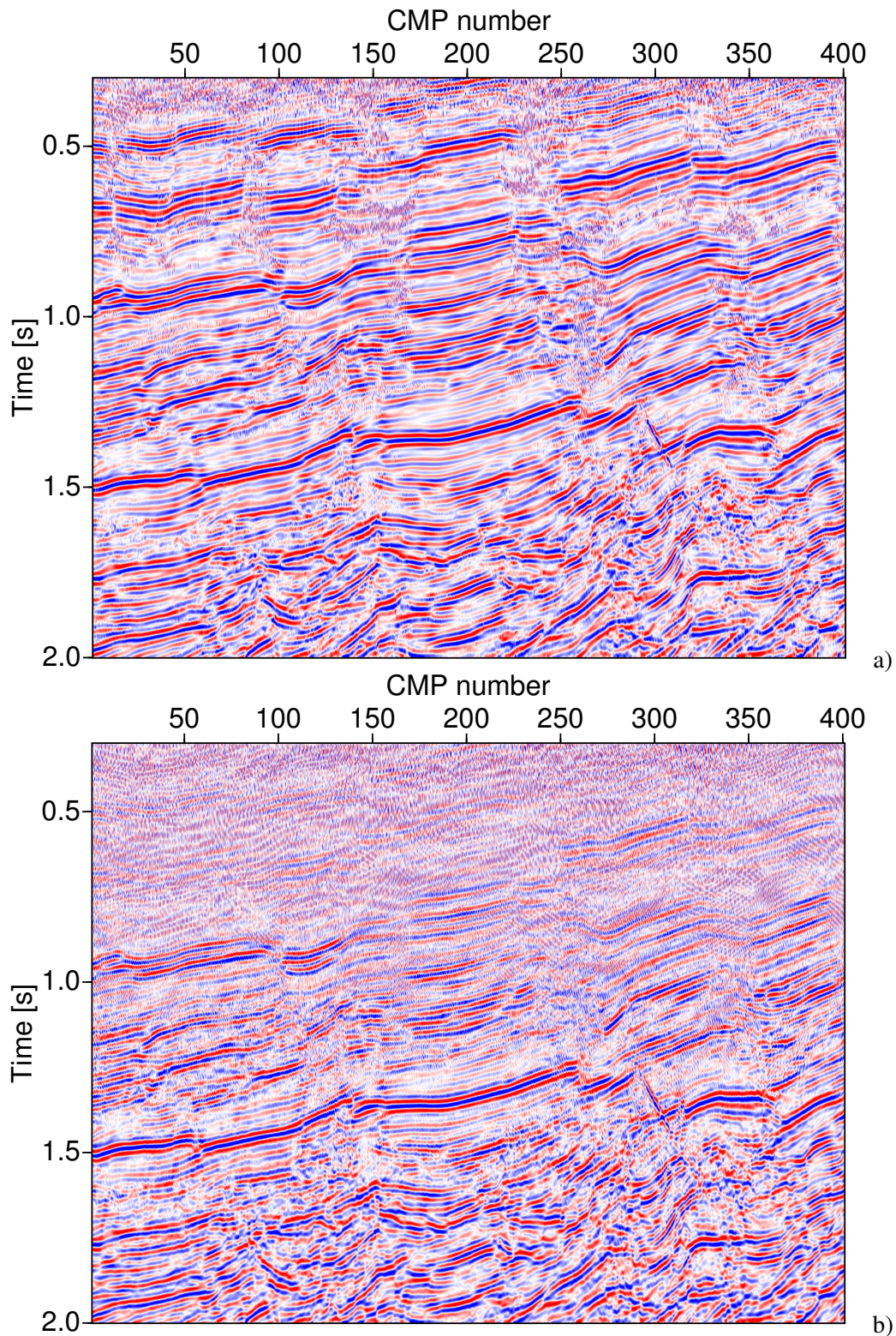
Figure 7.16: Result of the Kirchhoff poststack migration with (a) minimum aperture and (b) conventional aperture which linearly increased with traveltime. In the minimum-aperture result, the shallow events are no longer obscured by operator aliasing. The image quality in the lower part has improved and fault locations are better resolved.
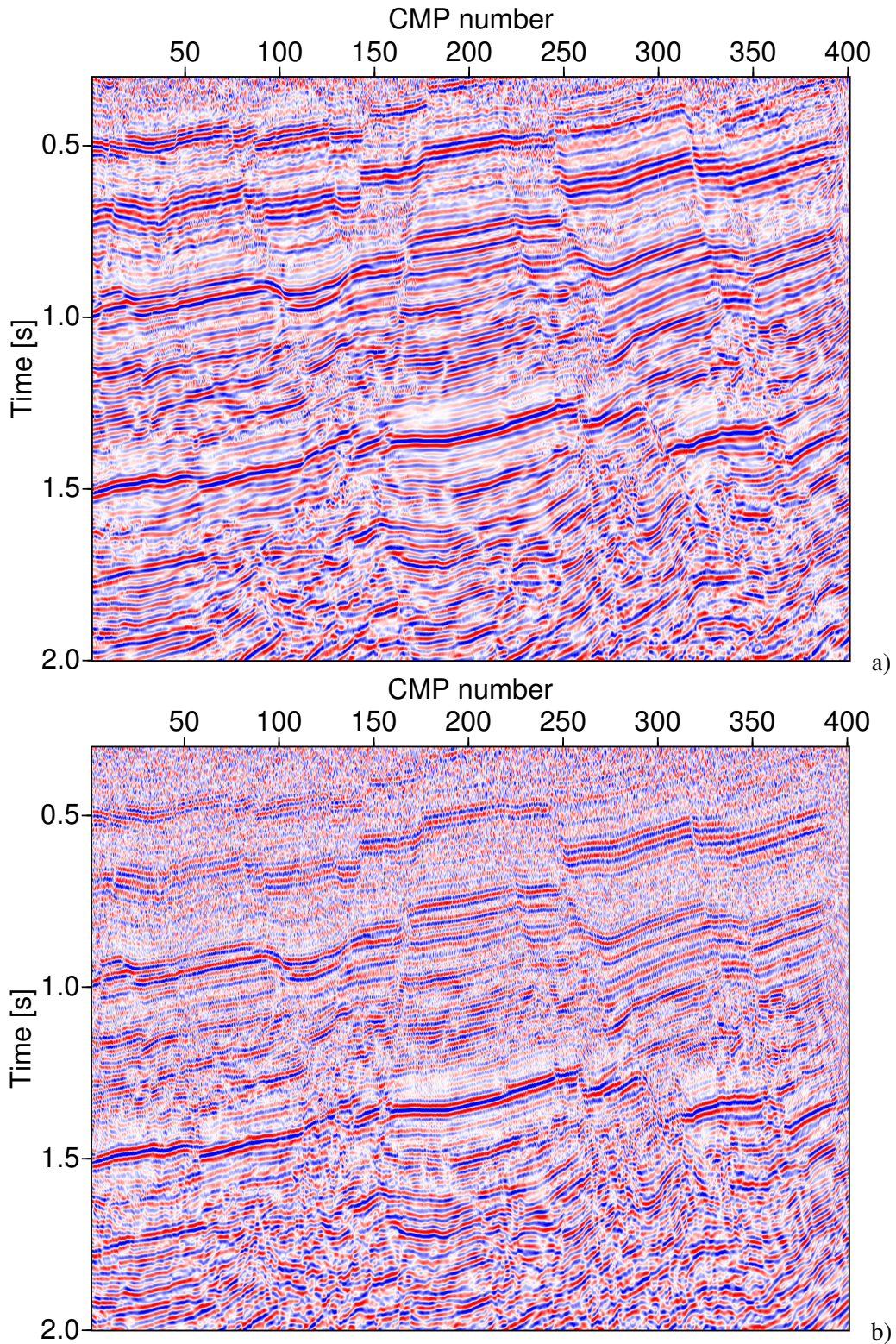
Figure 7.17: Stacked sections obtained from the prestack migration result with (a) minimum aperture and (b) conventional aperture. Again, the minimum-aperture result shows an improved image quality and more pronounced faults.
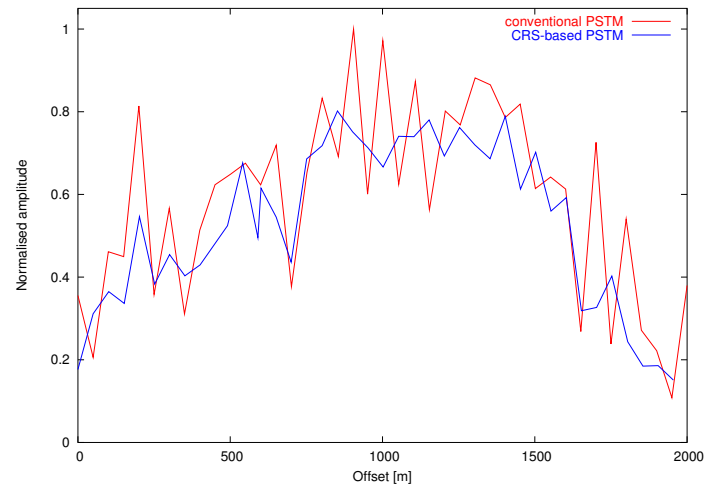
Figure 7.18: Normalised amplitudes extracted from the conventional (red) and the minimum-aperture (blue) prestack migration result at CMP no. 200. The amplitudes obtained by the minimum-aperture migration show a significantly reduced noise level.

migration apertures, the minimum-aperture migration leads to improved migrated sections and yields more reliable and less scattered amplitudes. Applications of the amplitudes like AVA analysis by means of crossplots clearly benefit from the reduced variance of the amplitudes.

Chapter 8

Minimum-aperture Kirchhoff time migration: 3D results

In this chapter, the minimum-aperture Kirchhoff time migration is applied to a 3D synthetic as well as a 3D real dataset. As in the 2D case, an additional Kirchhoff migration with user-defined conventional aperture was carried out for comparison.

In both examples, the prestack dataset used for migration shows an irregular trace distribution. This leads to a good azimuth coverage for prestack migration, but requires appropriate handling for true-amplitude migration to avoid acquisition footprint in the migrated image as well as in the amplitudes. One common method to compensate for irregular trace spacing in 3D is to weight the traces by the size of the Voronoi cell instead of a constant factor $\Delta\xi_1 \times \Delta\xi_2$ (see, e. g., Jäger, 2005b). This approach holds as long as the size of the Voronoi cells does not vary too strongly. In this case, an interpolation of the input traces is required.

The second effect related to the acquisition geometry which affects the true-amplitude result is the required binning with respect to absolute offset and offset azimuth. In the migration code used here, a constant bin spacing is utilised in both cases. This leads to an over-proportional weighting of the larger offsets as can be seen from the rose plot generated for the synthetic dataset depicted in Figure 8.2. This effect superposes and possibly even obscures the AVO effect in the data. By weighting each amplitude by the number of traces contributing to the summation, the amplitudes can be equalised with respect to each other. More sophisticated binning routines are based on flexible bin sizes to enforce a constant number of traces in each bin.

Both the irregular acquisition geometry and the constant bin size bias the true-amplitude result. However, the handling of both effects in the migration code goes beyond the scope of this thesis. Thus, at the current stage the amplitudes obtained by means of the 3D migration routines only allow a qualitative rather than a quantitative interpretation.

8.1   Synthetic data example

To demonstrate the potential of the 3D true-amplitude CRS-based Kirchhoff time migration synthetic pre- and poststack datasets were generated for the model shown in Figure 8.1. Here and in the following figures, an inline and crossline section from the centre of the model are depicted, respectively. The
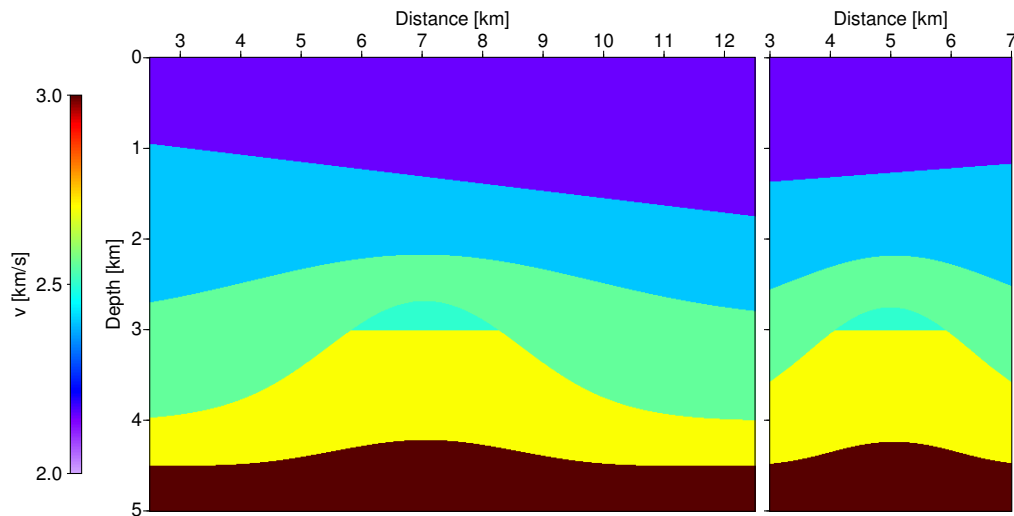
Figure 8.1: Inline (left) and crossline (right) section of the original interval velocity model used for modelling.

inline section was chosen such that the model is almost symmetric with respect to this inline plane except for the first reflector. This quasi symmetry allows for simple plausibility checks in the following. The target region for amplitude analysis is the lower interface of the gas-bearing layer beneath the dome-like structure.

The prestack dataset used for migration was generated on an irregular grid with an average midpoint spacing of 40 m. The irregular spacing was mandatory to provide a good azimuth coverage for prestack migration. The latter is shown in the rose plot in Figure 8.2. This requirement together with the limitations of the employed modelling tool led to a dataset far larger than originally anticipated. Therefore, the dataset had to be thinned out significantly. As the size of the remaining prestack dataset still exceeds 40 gigabytes, a full 3D processing of the data was not possible. Unfortunately, these technical restrictions cause aliasing in the migrated images which superimposes the searched-for AVO responses. In the following, this effect is demonstrated for one section in a selected azimuth bin.

A second prestack dataset with a regular midpoint spacing of 100 m in x- and y- direction was generated as input for the CRS stack. As the simulated ZO volume is not suitable for poststack migration due to the large trace spacing, an additional poststack dataset was generated on a $20 \times 20 \, m^2$ grid.

For all three datasets the primary P-waves were modelled by means of a wavefront construction method using a zero-phase Ricker wavelet with a dominant frequency of 40 Hz. The temporal sampling rate in the dataset is 4 ms in the poststack and 6 ms in the prestack data. Again, edge diffractions were not considered in the modelling which leads to gaps in the lower most reflector. Coloured noise was added to all datasets.

8.1.1 CRS stack and model building

The 3D CRS stack was carried out on the regular prestack dataset to provide the attribute volumes (not displayed) for the velocity model building and the minimum-aperture migration. The kinematic
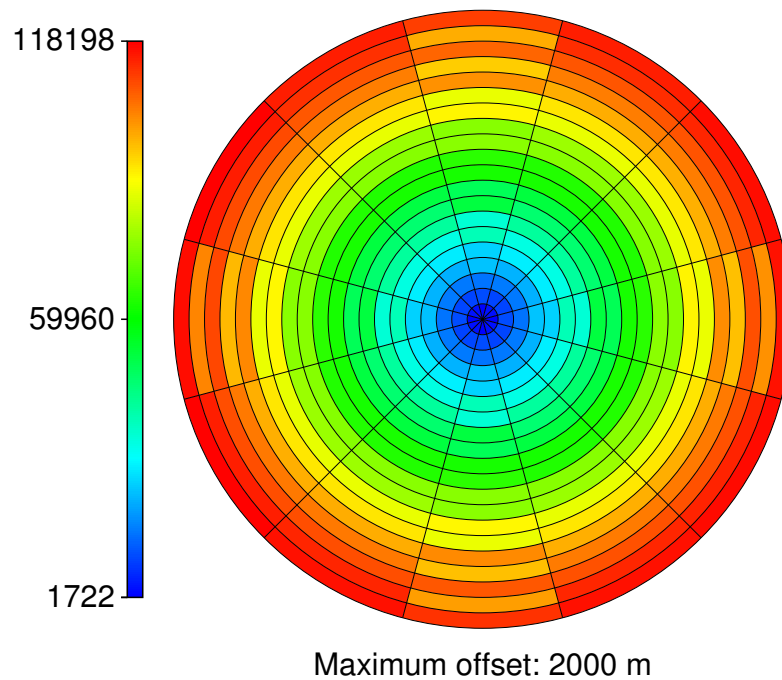
Figure 8.2: Rose plot showing the number of traces in the offset and azimuth bins for the irregular prestack dataset. The utilised offset binning was $100\,\mathrm{m}$ and the azimuth binning was $30°$.

wavefield attributes dip, azimuth, and normal wave curvature show a significant azimuth-dependency, whereas the NIP wave emerges with almost spherical wavefronts. This is due to the fact that the NIP wave experiment does not explicitly depend on the reflectors' structures but only on their overburden. For the considered model, the structural variations along the normal rays are small. However, the varying dip and azimuth of the emerging normal rays lead to an azimuth-dependency of the migration velocity which is considered in the model building.

The attribute volumes were smoothed in an event-consistent manner. Based on the coherence values, an automatic picking process was employed to extract reliable attributes for the velocity model building. By means of these attributes, the time migration velocities for azimuth $\gamma = 0°$, $\gamma = 45°$, and $\gamma = 90°$ were calculated. In a subsequent infill procedure, these values have been inter- and extrapolated on the target region by means of a distance-weighted polynomial interpolation. For the time migration, these models have to be transformed back to the matrix elements using equations (5.8). From the latter, the migration velocity is determined for each considered azimuth in the time migration code. The smooth time migration velocity models for azimuth $0°$ and $90°$ are shown in Figure 8.3, a similar model was obtained for $45°$. The velocity models resemble the azimuth-dependency of the stacking velocity: due to the symmetry with respect to the inline section, this section shows only small lateral variations for azimuth $0°$.[1] Some representative common-image gathers extracted from the inline and crossline volumes are depicted in Figure 8.4. Unfortunately, the CIGs suffer from aliasing, but the reflection events can still be observed as almost perfectly flat.

---

[1]Note that the azimuth-dependent migration velocity appears with interchanged azimuth directions due to the matrix inverse in equation (5.7).
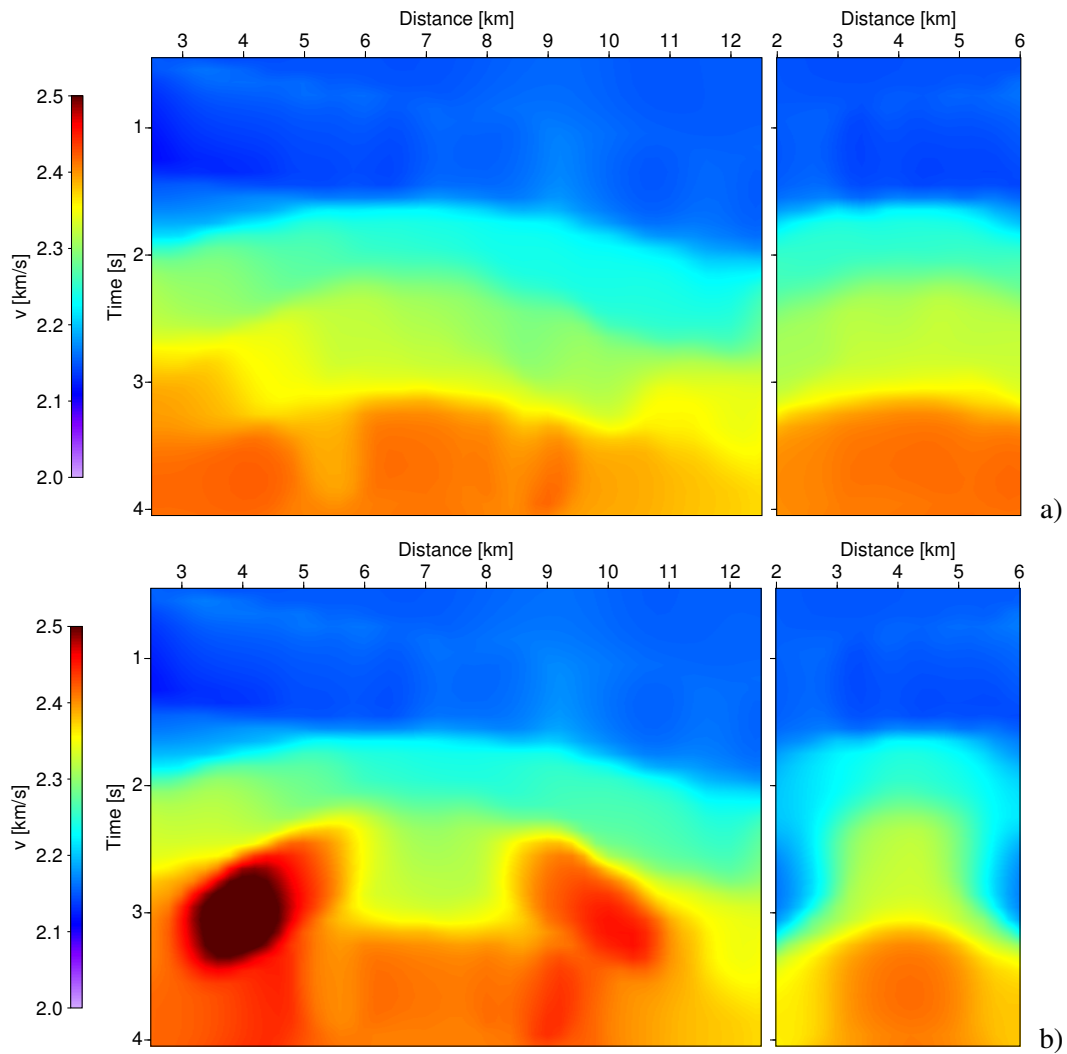
Figure 8.3: Time migration velocity models for azimuths a) 0° and b) 90°. Depicted is an inline and crossline section of the respective velocity model. See main text for details.

8.1.2 Poststack migration

The 3D poststack migration was performed twice, once using the limited aperture approach (Figure 8.5) and once with the conventional aperture (Figure 8.6) which was chosen wide enough to image the flanks of the dome. The minimum-aperture migration was only performed at locations where stationary points were detected. As in 2D, we observe gaps in the reflection events at points where no reliable attributes were available like in conflicting dip situations, e. g., at the intersection of the target reflector with the dome. In practice, the user-given aperture is used at all other locations to obtain a fully covered image without gaps.

In the conventional migration, missing diffraction events and modelling artifacts led to strong migration artifacts which degrade the result. In the limited aperture migration, the migrated image is clearer as the migration artifacts are strongly reduced, except in the conflicting dip situations. The dome-like
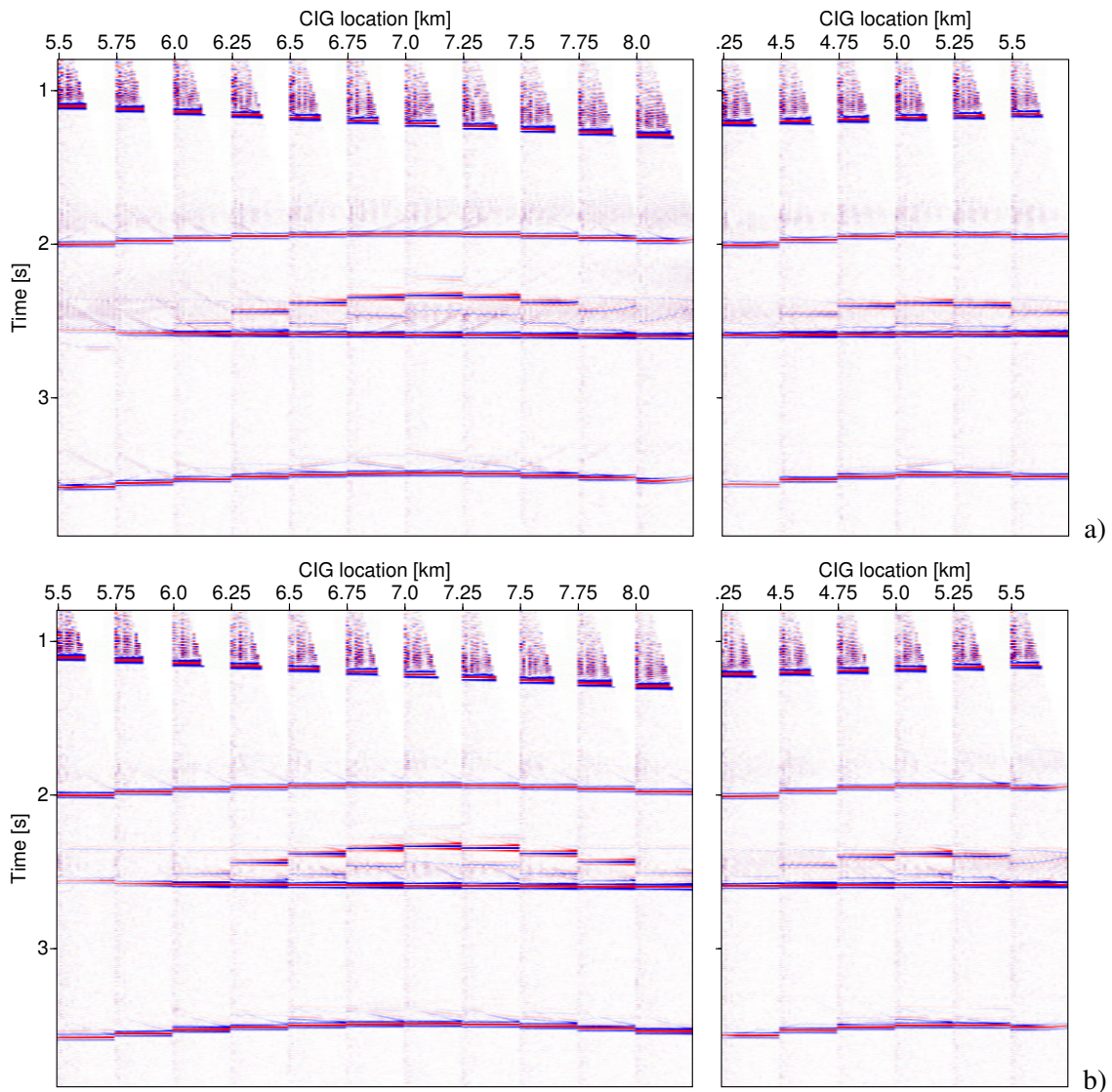
Figure 8.4: Common-image gathers extracted every 250 m from the prestack migrated azimuth bin for a) 0° and b) 90°. The CIGs extracted from the inline and crossline are depicted on the left and right, respectively. The maximum offset is 2000 m.

structure is not fully imaged in both crossline sections due to the limited acquisition geometry.

The displacement of the stationary point relative to the apex of the migration operator is depicted in Figure 8.7. The absolute values range up to approximately 1500 m at the steeply dipping flanks of the dome. The fluctuations of the values are in the order of the CRS grid spacing as the stationary point is detected using the nearest neighbour in the CRS volumes. Thus, the fluctuations directly reflect the discrete nature of the CRS results. Due to the model's quasi symmetry with respect to the inline, I observe very small y-components of the displacement vector of the stationary point for this line.

Figure 8.8 shows the corresponding size and orientation of the principal axes of the migration aperture. The projected Fresnel zone size shows a clearly elliptical shape. As the inline section coincides with
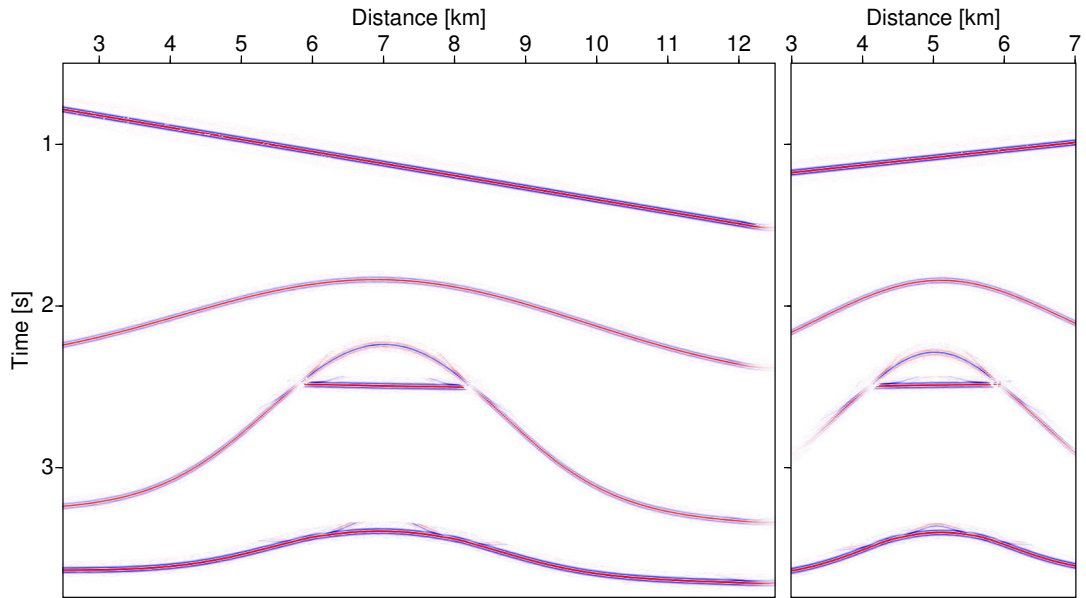
Figure 8.5: Inline (left) and crossline (right) section of the minimum-aperture migration result. The migration artifacts visible in the conventional result are significantly reduced.
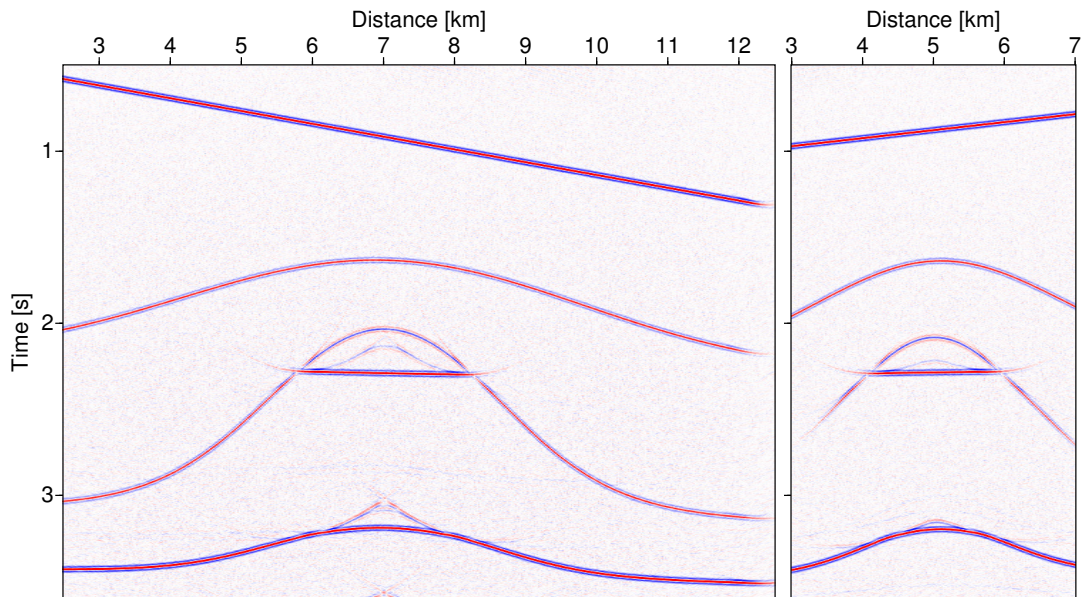
Figure 8.6: Inline (left) and crossline (right) section of the conventional poststack migration result.
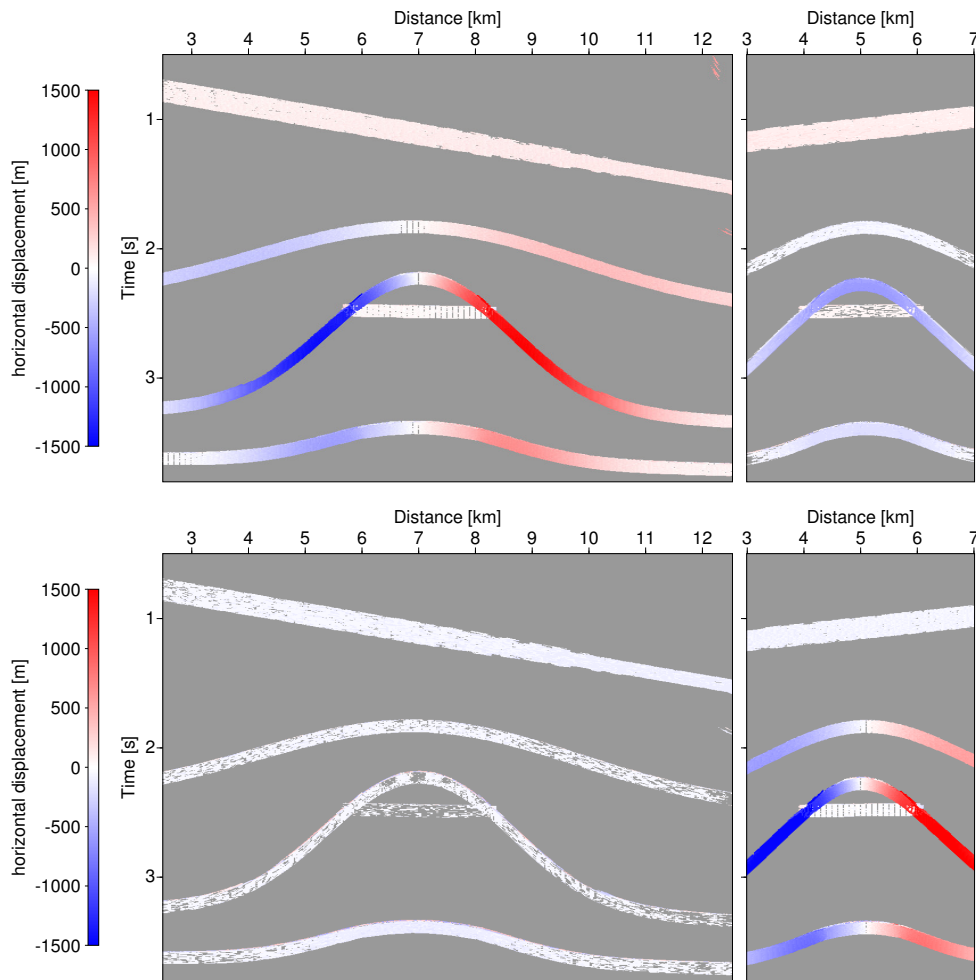
Figure 8.7: Horizontal displacement of the stationary point with respect to the apex of the migration operator for the *x*- (top) and *y*-direction (bottom), respectively. The left column shows the inline section while the right column depicts the respective displacements for the crossline section. The small y-component of the displacement in the inline section is due to the quasi-symmetry of the model.

the symmetry plane of the model concerning the lower reflectors, the major axis of the minimum aperture ellipse coincides with one of the model's axes. Thus, the calculated orientation of almost constantly 90° may serve as a plausibility criterion. In general, the orientation of the major axis varies laterally as can be seen from the crossline section. As the conventional approach has to account for the displacement and the Fresnel zone size simultaneously, the migration aperture has to be considerably increased. This leads to a ratio of about one to four for CRS-based to conventional aperture.

The amplitudes along the target reflector were extracted from both the conventional and the minimum-aperture results (Figure 8.9). The values for the ZO amplitude are slightly below the theoretical value of $R_0 = 0.055$. The CRS-based result shows a significantly reduced noise level as the data was only stacked along the relevant parts of the migration operators.
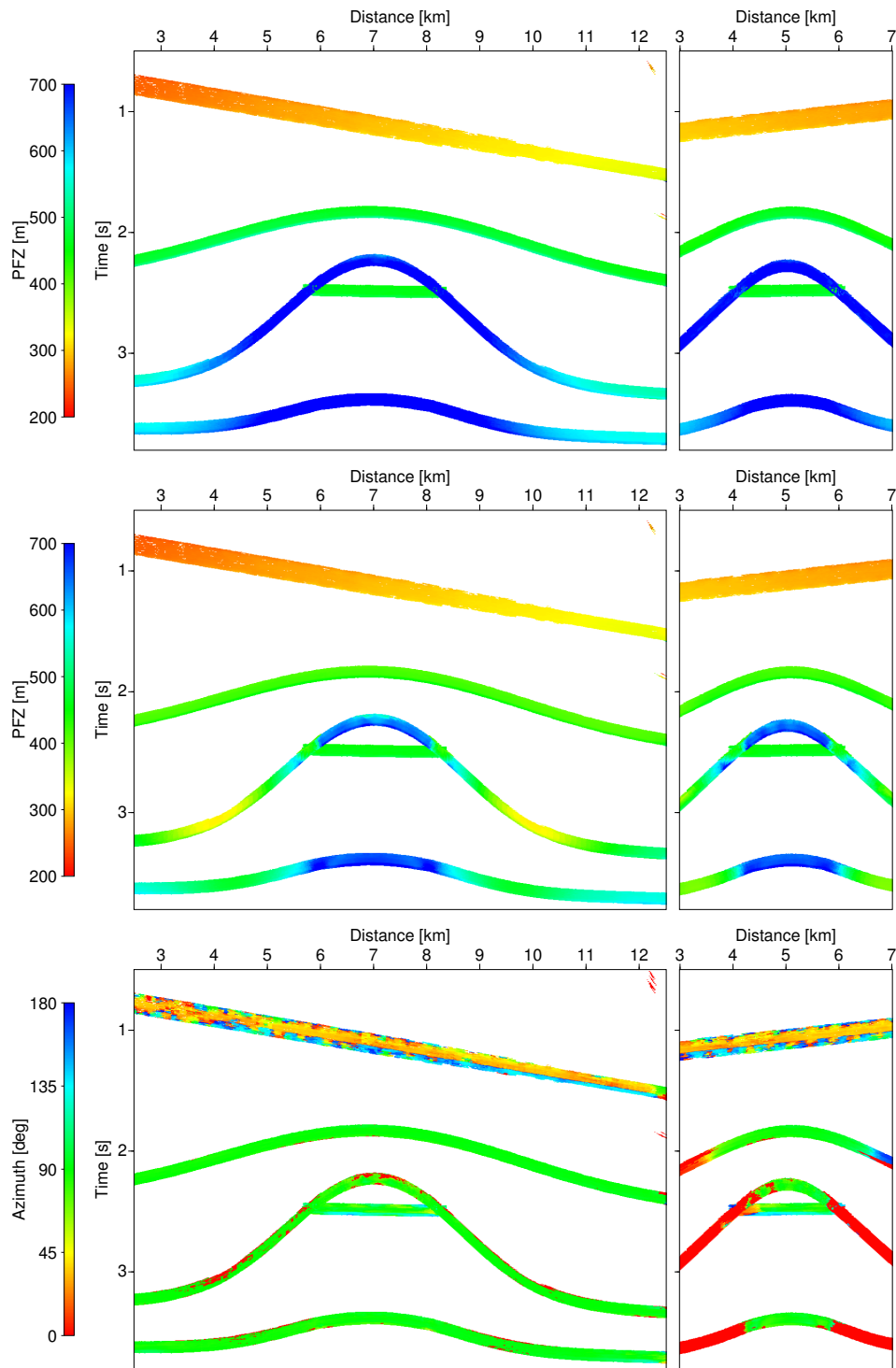
Figure 8.8: Principal major (first row) and minor (second row) axes of the elliptical minimum aperture. The third row depicts the orientation of the major axis with respect to x-axis. Displayed are the respective values for the inline (left) and crossline section (right). The almost constant value of 90° for the orientation in the inline section is due to the model's quasi-symmetry.
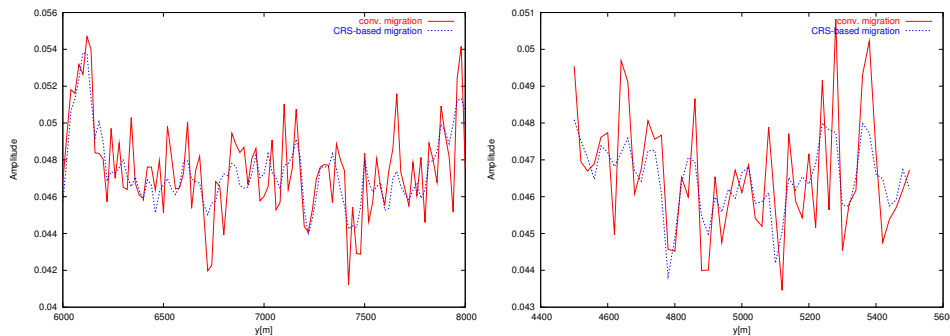
Figure 8.9: Amplitudes extracted from the conventional (red solid line) and CRS-based poststack migration result (blue dashed line) for the target reflector for the inline (left) and crossline (right) section. The amplitude variance in the CRS-based result is far lower compared to the conventional result.

8.1.3 Prestack migration

For the prestack migration I used the same processing parameters as for the poststack case described above. In addition, the CRP trajectory was used to extrapolate the stationary points to finite offsets. Furthermore, a linear widening of the aperture size with offset of 20% per 1000 m offset was considered.

In contrast to the poststack case, technical limitations required a coarser spacing of the modelled traces. As can be seen in the two representative migrated CO sections in Figure 8.10, strong aliasing degrades the migrated images. Amplitudes extracted along reflection events in these sections exhibit a behaviour totally dominated by the aliasing effects. Nevertheless, the amplitudes extracted along the target reflector (Figure 8.11) exhibit a lower noise level with the CRS-based aperture. As the migration artifacts vary with offset, I expect a significant footprint of the aliasing in the AVO curves, too. This can indeed be seen in Figure 8.12: the AVO curves for conventional as well as limited-aperture migration suffer from strong artifacts which almost totally obscure the different noise levels achieved with the two different migration schemes.

Modelling studies showed that with the available computing facilities and within the given time frame, it is not possible to generate synthetic data of reasonable size with sufficient coverage and trace density for the considered model. Therefore, a meaningful interpretation of the prestack results failed due to migration artifacts. Anyway, a general reduction of the noise level of the amplitudes could be achieved.

8.2 Real data example

The real onshore dataset presented in the following was made available within the scope of the project *High resolution images of subsurface CO2 storage sites in time and depth by the CRS methodology* described in Trappe et al. (2005).

This dataset was acquired onshore with an irregular acquisition geometry providing a full azimuth coverage. Parts of the data expose a footprint of surface topography which has not been removed
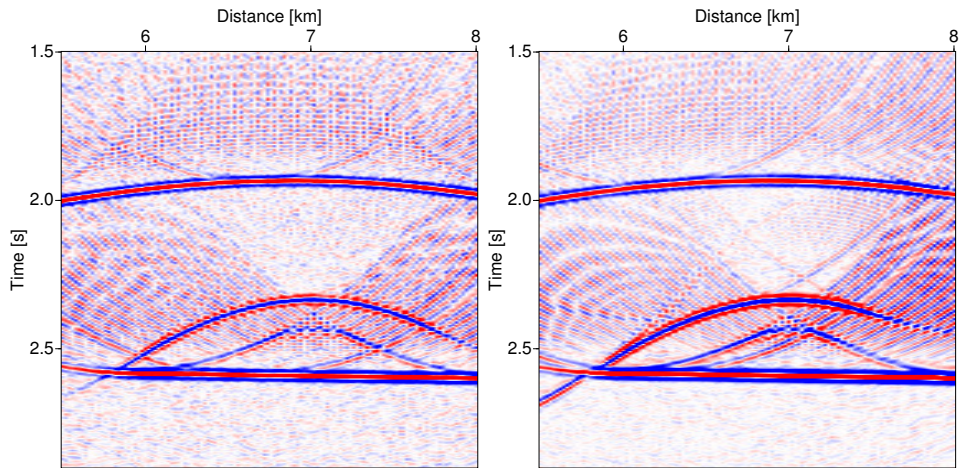
Figure 8.10: Details of the migrated inline CO sections for offset 500 m (left) and 1500 m (right) extracted from the prestack migrated data obtained with conventional aperture. The images are strongly contaminated by aliasing effects.
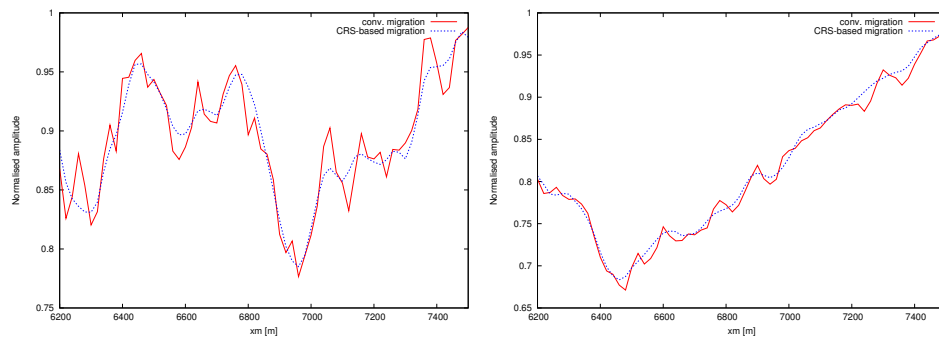
Figure 8.11: Amplitudes extracted from the conventional (red solid line) and CRS-based prestack migrated inline sections (blue dashed line) for the target reflector. Shown are the results for offsets 500 m (left) and 1500 m (right). Note the reduced noise level in the CRS-based results.
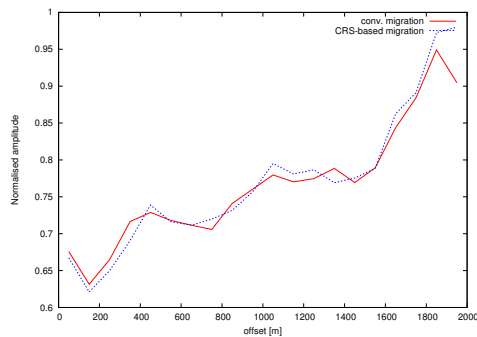
Figure 8.12: AVO curves extracted from the conventional (red solid line) and CRS-based prestack migrated inline sections (blue dashed line) for the target reflector at $x = 6500$ m.
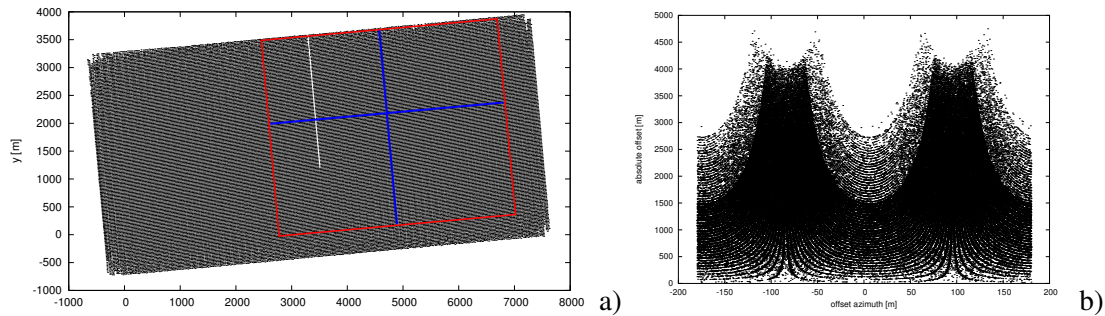
Figure 8.13: a) The lateral distribution of midpoints covers a rectangular area which is rotated by approximately 5.2° with respect to the global coordinate system. b) Distribution of absolute offsets as function of offset azimuth. Every 10th trace is displayed.

in the provided prestack data. The total recording time is 4 s with a temporal sampling rate of 4 ms. Figure 1.1a) shows the lateral distribution of the source/receiver midpoints. They cover an almost rectangular area which is rotated by about 5.2° with respect to the global coordinate system. The average distance between the midpoints is 25 m in both x- and y-direction. The red rectangle indicates the data subset used in the framework of this thesis. This area was selected as it shows only a minor influence of the topography. Similar as for the synthetic data example, I present the results for a selected inline and crossline represented by the blue lines in Figure 8.13a).

The distribution of the offset azimuth versus the absolute offset of all traces is visualised in Figure 8.13b). The maximum absolute offset varies with azimuth between 2700 and 4700 m. A offset and azimuth binning as performed for the 3D synthetic dataset leads to an insufficient trace coverage: in the majority of bins the midpoint distribution is highly irregular and often suffers from clustering. Therefore, an azimuth binning was not considered for migration. Fortunately, the CRS wavefield attributes reveal little azimuth dependency such that the avoidance of azimuth binning is justified for these data.

8.2.1 CRS stack and model building

As the dataset shows a full azimuth coverage, the CRS stack could be performed with eight parameters. The determination of the kinematic wavefield attributes was split into three independent searches according to the procedure described in Müller (2003) followed by a local eight-parameter optimisation. Due to limited computer facilities, a small search-aperture in midpoint direction had to be chosen leading to a decreased stability in the determination of the normal wave curvatures. An event-consistent smoothing was applied to the attribute volumes.

An inline and crossline section of the simulated ZO volume is shown in Figure 8.14a). The subsurface structure shows little lateral variations which predestines the data for time migration. Figure 8.14b) and 8.14c) shows an inline and crossline section of the dip volume and the associated coherence sections, respectively.

In Figures 8.15a) and b), the stacking velocities for x- and y-direction calculated from the smoothed wavefield attributes are depicted. The velocities reveal only a minor azimuth-dependency except for
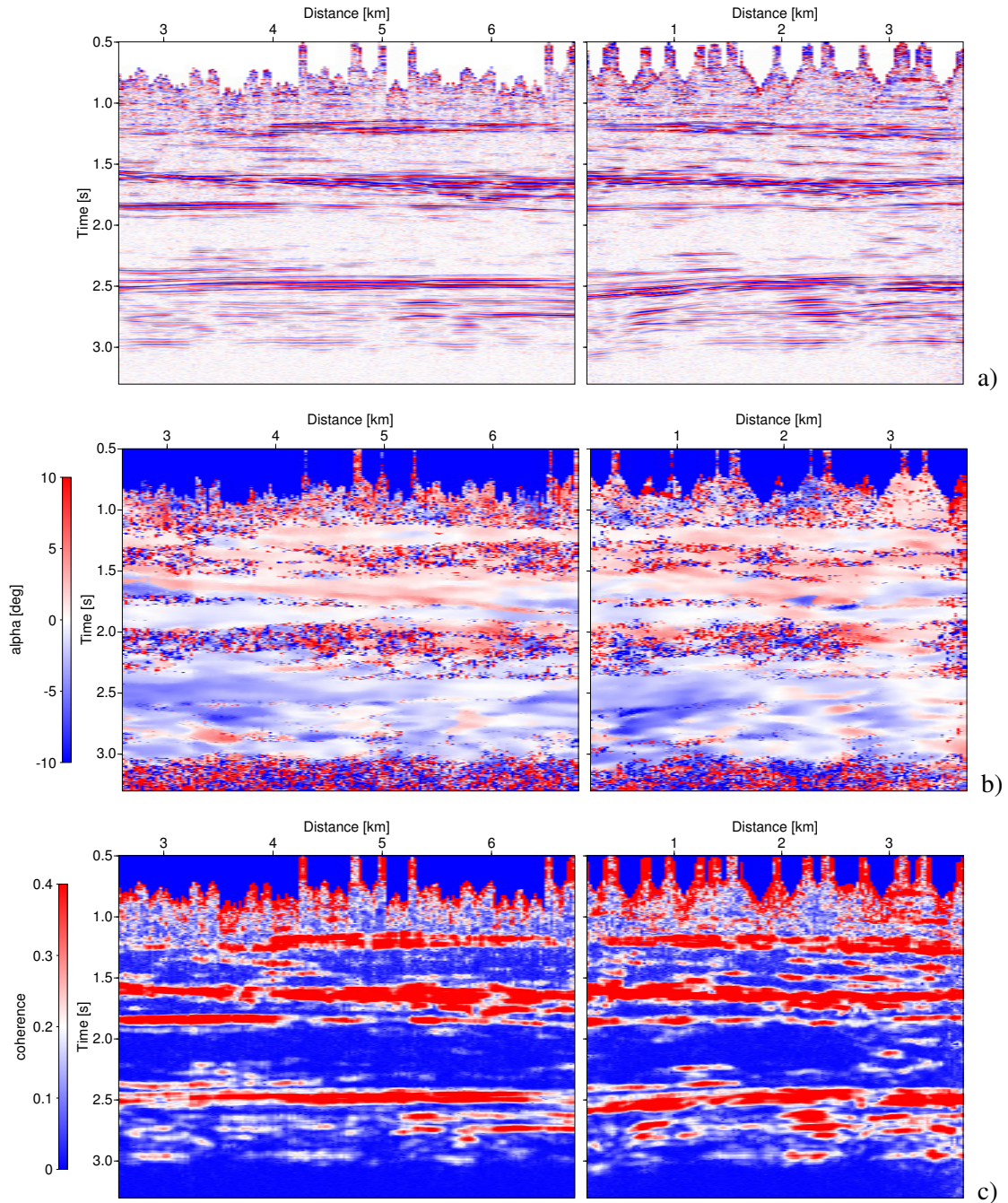
Figure 8.14: a) Inline (left) and crossline (right) sections of the simulated ZO volume. b) Inline (left) and crossline (right) sections showing dip and c) associated coherence sections.

a few locations, e. g., in the crossline section at $x = 2.2$ km and $\tau = 3$ s. These lateral locations can be clearly associated with undulations of the top-surface topography which falsify the attributes. The impact of the topography on the stacking velocity is better resolved in the deeper part of the sections where the moveout is smaller. For the determination of the time migration velocity model, the smoothed attributes associated with the reflection events were extracted. Locations showing an increased azimuth-dependency of the wavefield attributes were omitted. The picked values were converted to time migration velocities and interpolated and extrapolated on the target volume. The obtained time migration velocity model is depicted in Figure 8.15c). The migration velocity model is consistent with the prestack data as can be seen from the common-image gathers in Figure 8.16.

8.2.2 Poststack migration

The minimum-aperture poststack migration was carried out on the simulated ZO volume. The stability of the determination of dip and azimuth allowed to choose a low coherence threshold so that stationary points were found on nearly all visible reflection events. Due to the instability of the determined normal wave curvature, the calculated size of the projected Fresnel zone shows abnormal variations of the values on the reflectors. Due to the small dips and curvatures of the reflectors, the projected Fresnel zone size is expected to be nearly constant on a reflector and to slowly increase with traveltime. Therefore, a plane normal wave (PNW) approximation was utilised in the determination of the projected Fresnel zone size by setting $\mathbf{K}_N := \mathbf{0}$. As the reflectors do not show strong curvatures, the approximation is supposed to lead to reasonable apertures.

The effect of the smoothing and the PNW approximation on the minimum-aperture migration result is shown in Figure 8.17. The first row depicts subsets of the minimum-aperture migrated crossline section obtained with unsmoothed attributes (left), smoothed attributes (middle), and smoothed attributes together with the PNW approximation (right). The second and third row show the corresponding x-component of the displacement of the stationary points and the major principal axis of the minimum-aperture ellipse. Amplitudes were extracted from all three migration results and are depicted in Figure 8.18. The unsmoothed attributes lead to outliers and a certain amount of scattering in the location of the stationary point as well as in the aperture size. This clearly influences the migrated image and in particular the migrated amplitudes (red line in Figure 8.18). Using the smoothed attributes stabilises the found stationary points and improves the migrated image. The determined Fresnel zone size shows less scattering due to the smoothing of the NIP wave curvature, but the values still vary strongly. Although the effect is hardly visible in the migrated image, the amplitudes clearly suffer. Using the PNW approximation, reasonable values are obtained for the size of the projected Fresnel zone. Depending on the sign of the curvature of the normal wave, the values are slightly above or below the average values with the determined normal wave curvature. Therefore, the estimated size of the projected Fresnel zone is increased by 50%. Now, the extracted amplitudes are showing a smooth distribution of the values.

Figures 8.19 and 8.20, the displacement of the stationary points and the size and orientation of the minimum aperture are displayed for the inline and crossline sections. The horizontal displacement is generally small due to the small dip of the reflectors. The estimated minimum aperture is almost circular. The minimum-aperture migrated image is shown in Figure 8.21a). The migration was only carried out at locations with detected stationary points. A second poststack migration was carried out with a user-controlled aperture centred around the operator apex. The aperture was chosen to linearly increase with increasing traveltime from 500 m at 0.5 s to 900 m at 2.9 s in both x- an y-direction. The same taper was applied in both migrations.
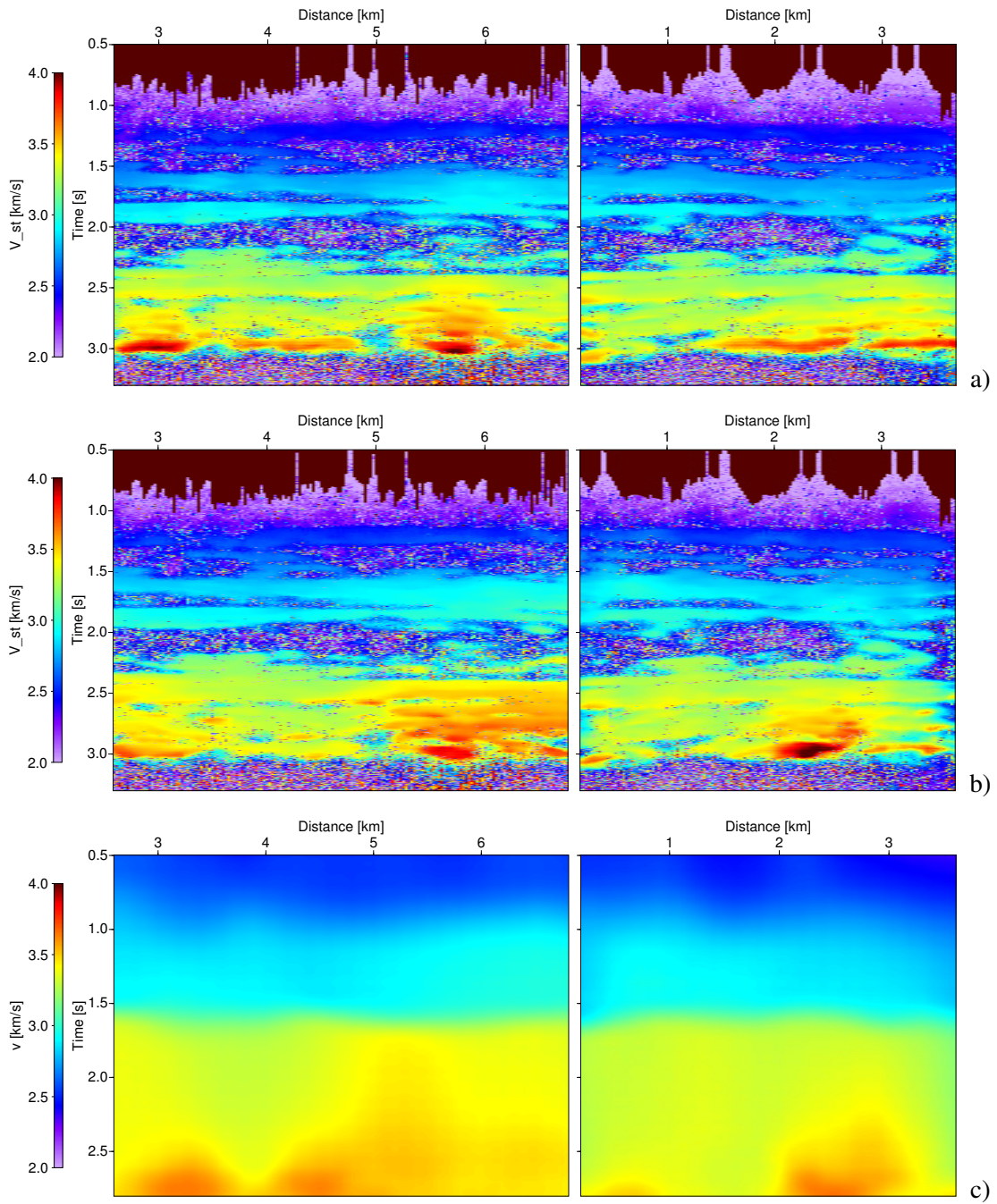
Figure 8.15: Inline (left) and crossline (right) sections showing the stacking velocity a) in *x*-direction and b) in *y*-direction obtained after event-consistent smoothing of the CRS attributes. c) The time migration velocity model obtained from the CRS attributes.
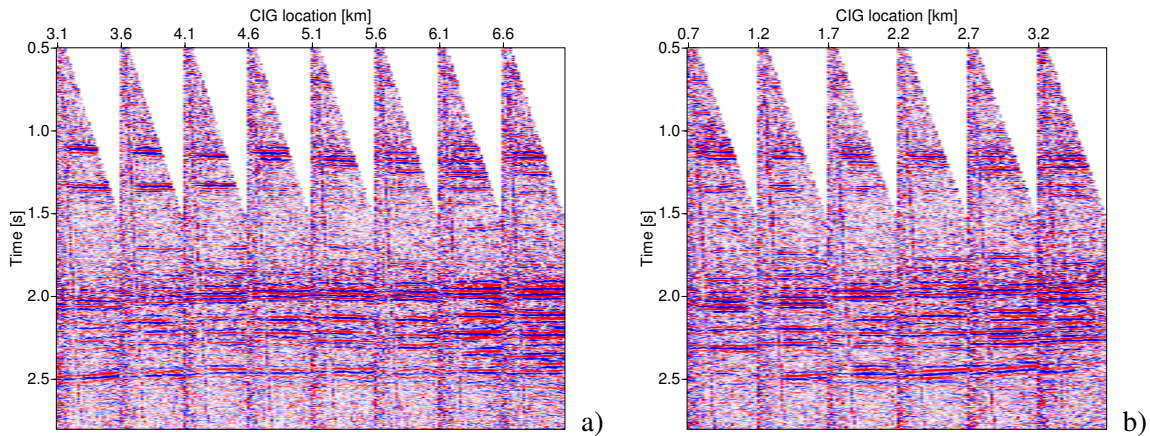
Figure 8.16: Common-image gathers extracted every 500 m from the prestack migrated a) inline and b) crossline section. The maximum offset is 2500 m.

The comparison between the migrated image obtained with the minimum-aperture approach and conventional migration reveals only small differences. Because of the good signal-to-noise ratio in the data, both migrations perform well and provide a clear image. Due to the small displacement of the stationary point from the operator apex, the differences between both migration schemes lies mainly in the size of the migration aperture. Here, the PNW approximation in the minimum-aperture approach and the necessary widening of 50% further reduced the difference in aperture size. However, the minimum-aperture migration avoids the operator aliasing which is present in the shallow part of the conventional result and reduces migration artifacts. The impact of the minimum aperture is more evident in the dynamic results: the amplitudes extracted from the minimum-aperture result shows reduced scattering as can be seen from Figure 8.22.

8.2.3 Prestack migration

In the same way as in the poststack case, two prestack migrations were applied to the full prestack dataset. The minimum-aperture migration was carried out at all locations where a stationary point was found in the poststack case. Due to the almost horizontal structure, the displacement of the stationary point with offset is expected to be negligible. Therefore, the aperture size is only slightly increased by 10% per 1000 m offset. The aperture size for the conventional migration was chosen as in the corresponding poststack migration. Both prestack results were scaled by the number of traces contributing to the summation in the conventional migration to avoid an overweighting of the higher offsets. The prestack-migrated stacked sections are displayed in Figure 8.23. Again, both migration schemes perform well on this dataset. The minimum-aperture migration provides a clearer image showing a reduced noise level and less migration artifacts, especially in the shallower parts. Note that in practice, the user-given aperture would be used at all locations where no stationary point was detected to obtain a fully covered image without gaps.

In order to compare the dynamic results, amplitudes were extracted from the minimum-aperture and conventional migration results for the strong reflection event slightly below 2 s. Representative AVO curves obtained for the inline and crossline section are depicted in Figure 8.24. Both migration
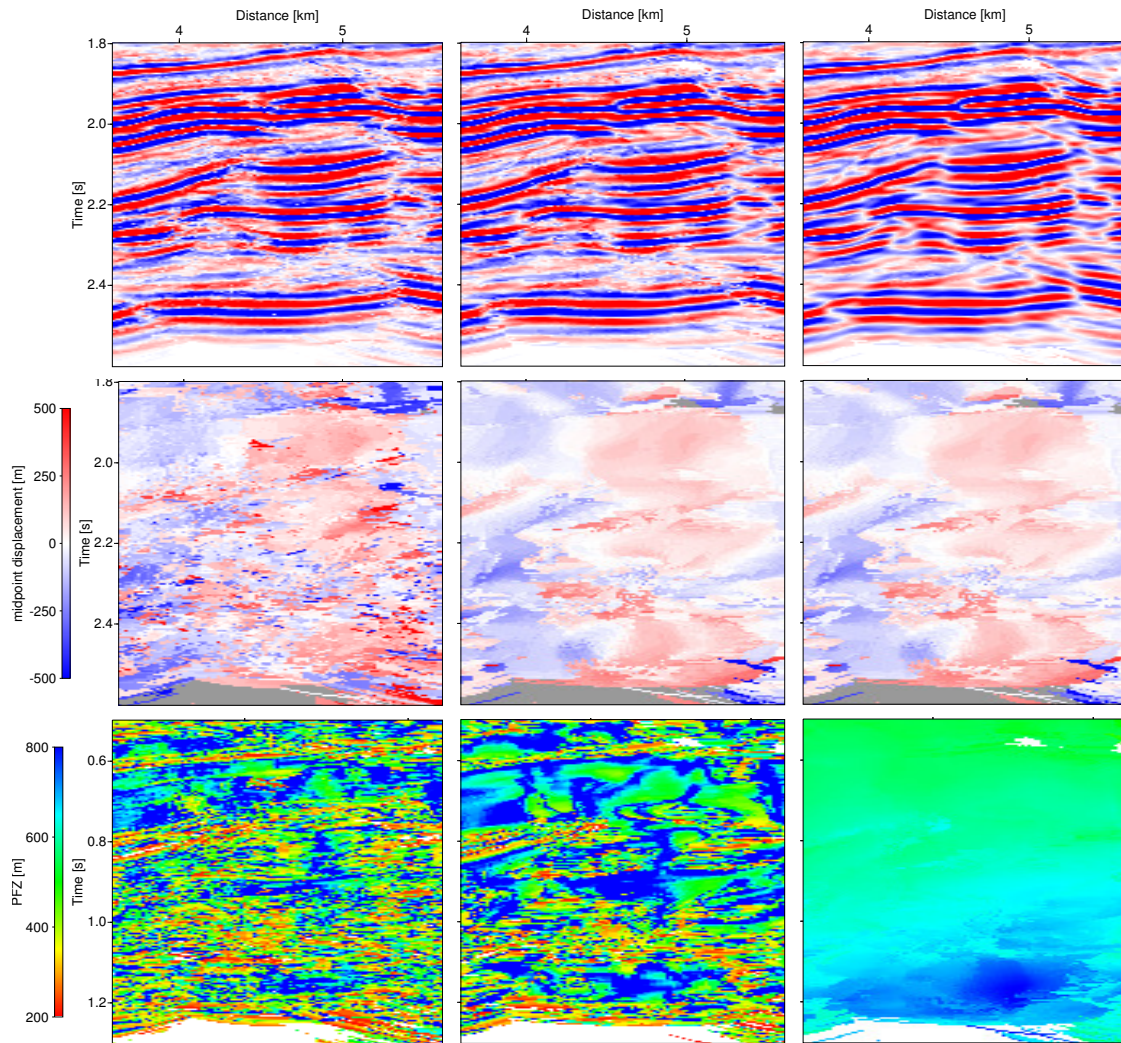
Figure 8.17: Effect of smoothing and of the plane normal wave approximation on the minimum-aperture migration result. The first row depicts subsets of the minimum-aperture crossline section obtained with unsmoothed attributes (left), smoothed attributes (middle), and smoothed attributes together with the plane normal wave approximation (right). The second and third row show the corresponding x-component of the displacement of the stationary points and the major axis of the minimum aperture ellipse. The midpoint displacement sections in the middle and right columns coincide as this property is not affected by the PNW approximation. Note that the values shown here for the major axis are already increased by 50%.

schemes provide similar AVO curves. Due to the equalisation of the offset-dependent amplitudes, these curves no longer resemble a physical AVO behaviour. In addition, the AVO behaviour is further degraded due to the highly irregular trace distribution leading to strong fluctuations in the amplitudes which superimpose the effects caused by the different noise levels in the migrated results. Figure 8.25 shows amplitudes extracted from the inline CO section for 2100 m offset. Here, the reduced noise level of the amplitudes obtained by the minimum-aperture migration is clearly visible.
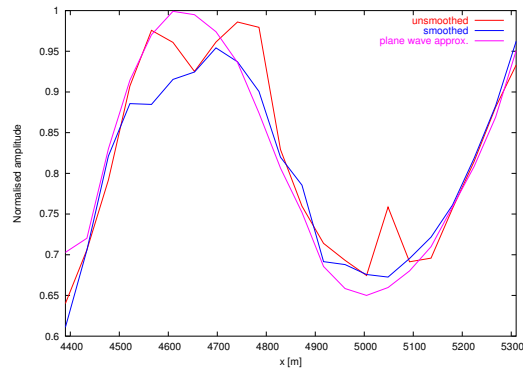
Figure 8.18: Effect of smoothing and of the plane normal wave approximation on the migrated amplitudes. Depicted are amplitudes extracted from the minimum-aperture result using unsmoothed attributes (red), smoothed attributes (blue), and smoothed attributes together with the PNW approximation (purple). See main text for details.
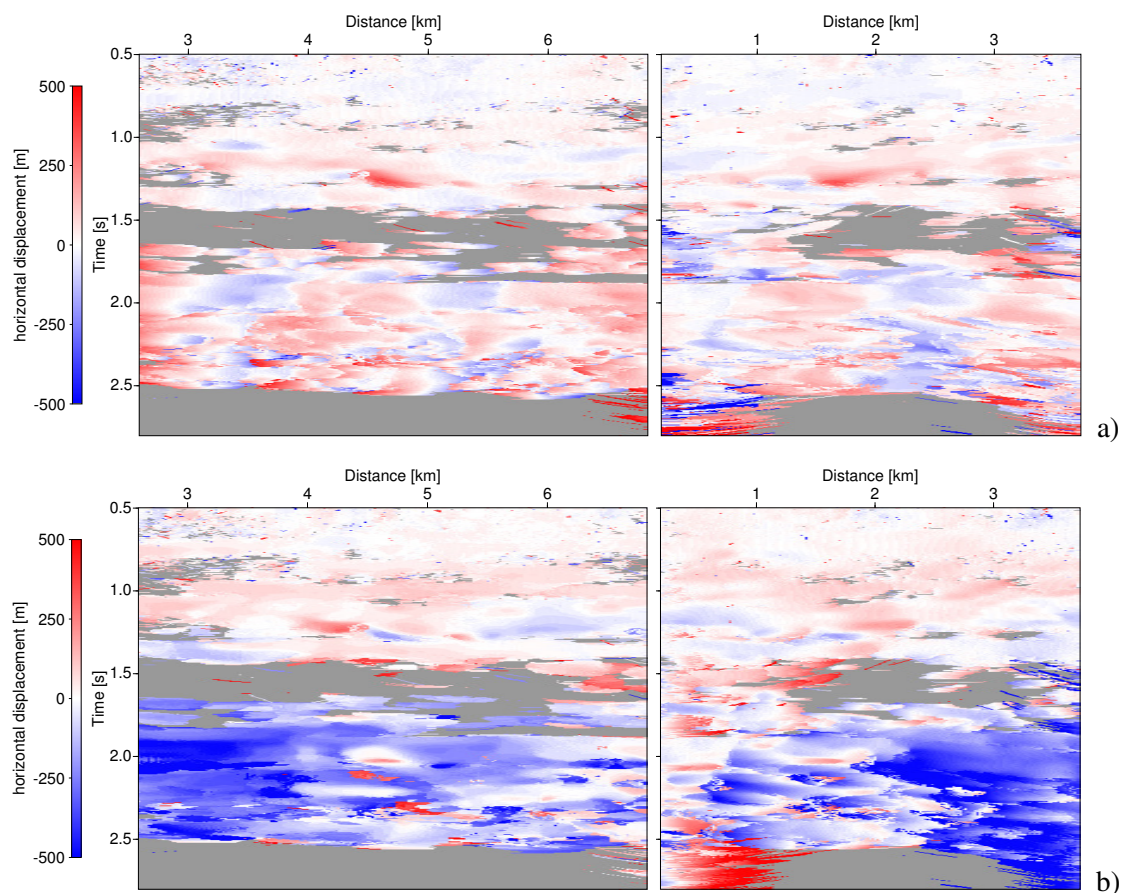
Figure 8.19: Horizontal displacement of the stationary points with respect to the operator apex in a) *x*-direction and b) *y*-direction. Only locations with detected stationary points are displayed.
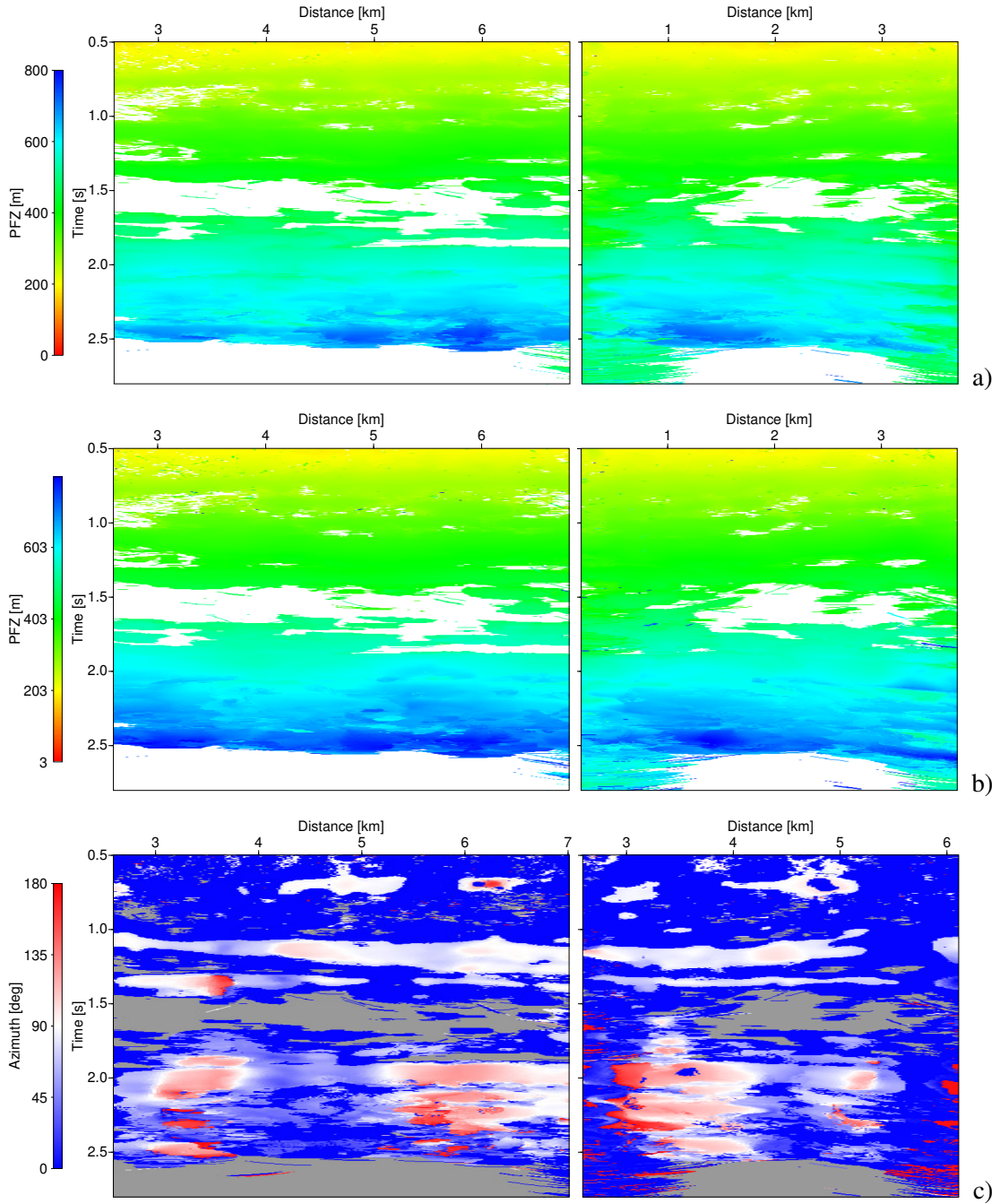
Figure 8.20: a) Principal major and b) minor axes of the elliptical minimum aperture. c) Orientation of the major axis with respect to *x*-axis.
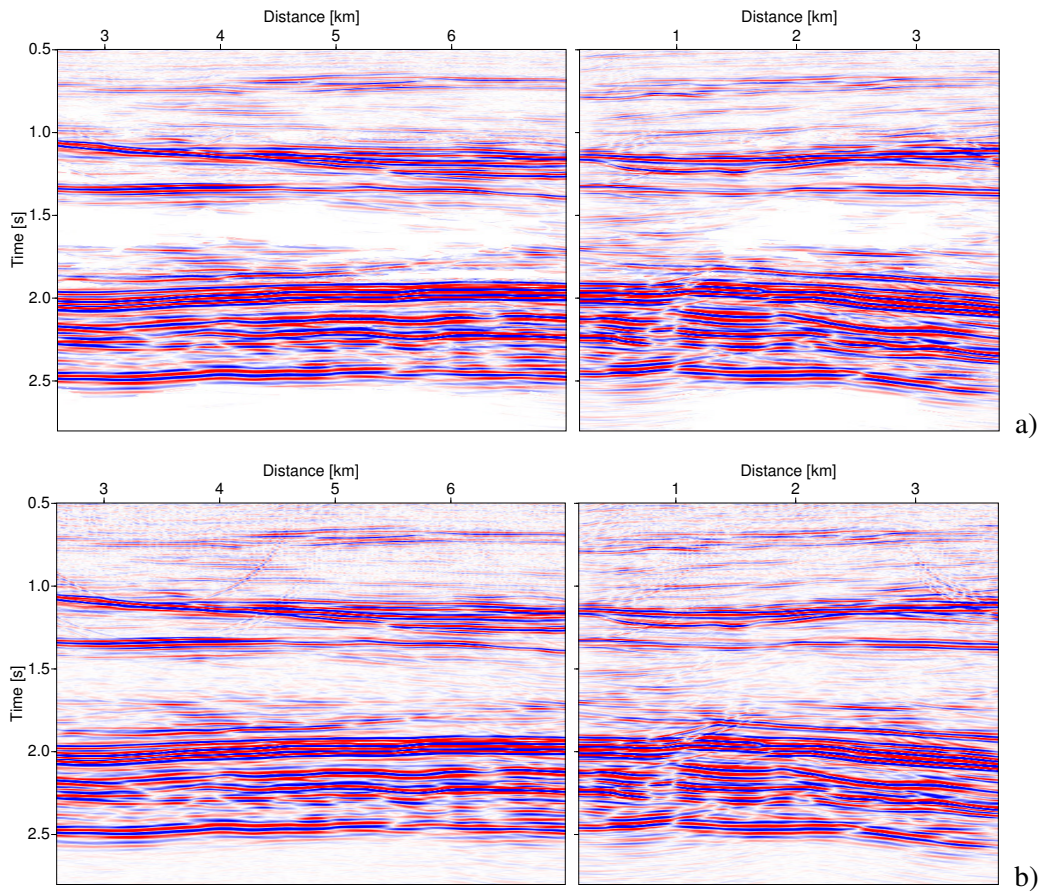
Figure 8.21: Inline (left) and crossline (right) sections of the Kirchhoff poststack migration result with a) minimum aperture and b) conventional aperture.
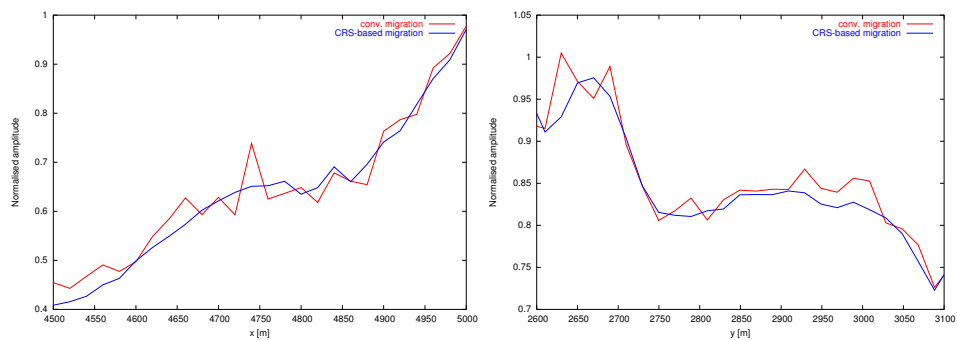
Figure 8.22: Amplitudes extracted from the conventional (red solid line) and CRS-based poststack migration result (blue dashed line) for the inline (left) and crossline (right) section.
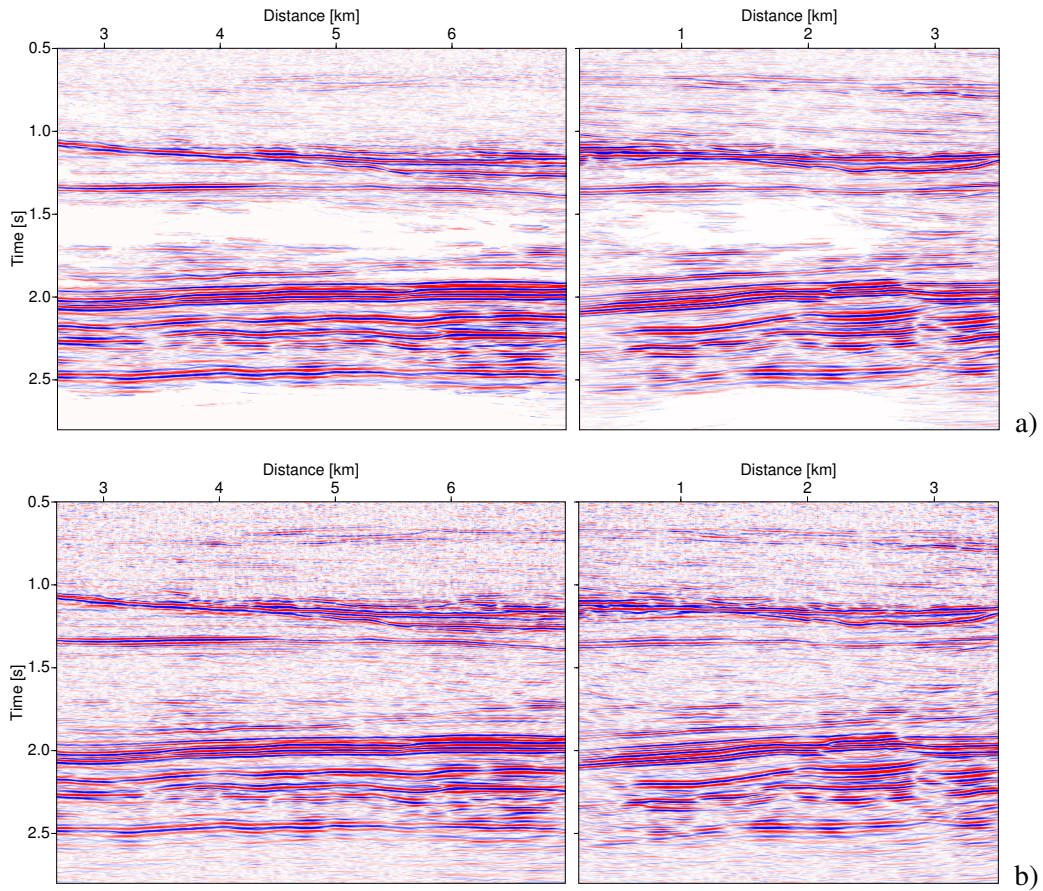
Figure 8.23: Inline (left) and crossline (right) sections of the Kirchhoff prestack migration result with a) minimum aperture and b) conventional aperture.
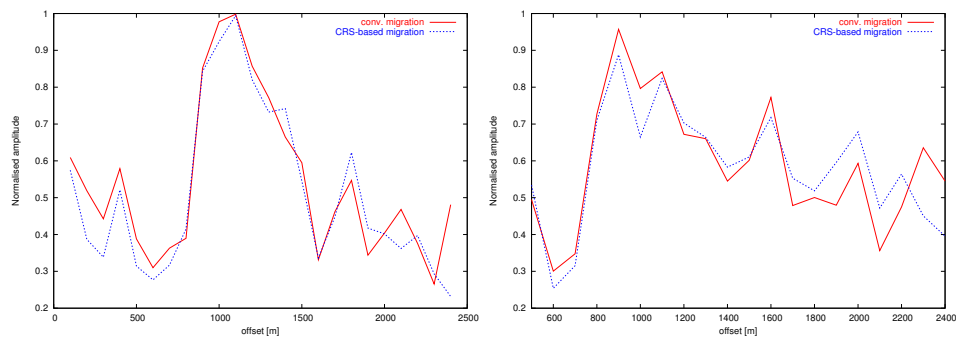
Figure 8.24: AVO curves extracted from the conventional (red solid line) and CRS-based prestack migration result (blue dashed line) for the strong reflection event slightly below 2 s.
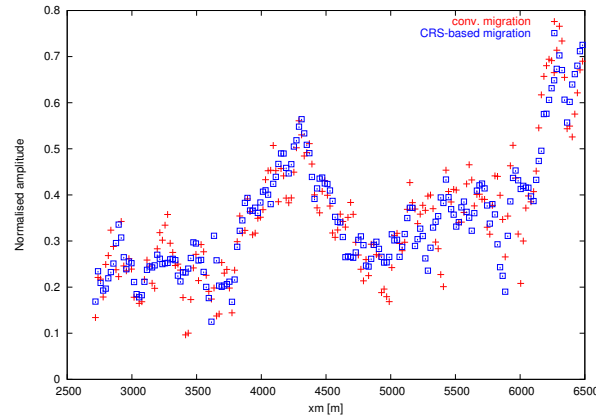
Figure 8.25: Amplitudes extracted from a representative CO section for the inline result for the strong reflection event slightly below 2 s. The conventionally obtained amplitudes are depicted in red, the CRS-based results in blue. The CRS-based result shows a reduction of the noise level in the amplitudes.

8.3 Summary

In this chapter, the applicability of the minimum-aperture time migration was evaluated for 3D on both synthetic and real data. For the real dataset, the concept allowed a stable estimation of the size and location of the optimum migration aperture for the poststack case and an approximate extension for finite offsets. As in the 2D case, the minimum-aperture migrated sections showed reduced migration artifacts and a decreased noise level and the amplitudes are less scattered compared to migration results with conventional user-defined aperture. For the synthetic data, I successfully applied the poststack migration scheme with similar improvements as for the real data. However, the prestack approach did not lead to sound and interpretable results except for a reduced noise level in the amplitudes. This is due to the limited modelling and processing capacities available. Nevertheless, there is no indication that the presented approach would not lead to the expected improvements if these technical limitations were overcome.

Chapter 9

Conclusion

In the scope of this thesis, I have studied the transformation of reflection seismic data into a structural image of the subsurface. This central step in the seismic imaging workflow is called migration. The extension to true-amplitude migration additionally compensates for the geometrical spreading effect during the transformation and, thus, allows to recover reflection amplitudes. Seismic time migration which is considered here has been introduced as an approximate transformation process based on the assumption of a laterally homogeneous velocity distribution. With this prerequisite, integral velocities are assumed to be sufficient to characterise the overburden and the velocity model building is considerably simplified. In practice, the assumption of a 1D medium is never strictly met. Therefore, the application of time migration is usually extended to media showing mild to moderate lateral velocity variations. The main advantage of time migration lies in its reduced sensitivity to velocity model errors compared to the depth migration process. This does not only influence the quality of the migrated image but also has a strong impact on the amplitudes. Thus, seismic amplitude analysis is usually carried out on time-migrated results because they provide more reliable and less distorted amplitude information.

Within this thesis, I have focussed on true-amplitude Kirchhoff time migration. A geometrical description of the migration process in terms of a weighted diffraction stack has been presented and the derivation of the true-amplitude weight function based on paraxial ray theory has been outlined. Starting from the general description of Kirchhoff migration in the depth domain, I have derived the approximate time domain approach based on the straight-ray assumption.

In order to apply migration in the time domain, a model of the integral velocities is required. For media showing lateral velocity variations, such migration velocities deviate from the stacking velocities and have to be determined by means of, e. g., migration velocity analysis or scanning routines. In this thesis, I have considered the derivation of an approximate time migration velocity model from the kinematic wavefield attributes provided by the Common-Reflection-Surface stack method. The model derivation considers the temporal and spatial shift between the stationary point and the migration operator apex and allows for an azimuth-dependency of the migration velocity. However, the latter cannot be fully exploited in the DSR operator for finite offset.

The main aspect of the thesis is to improve the image quality and in particular the amplitudes in the time-migrated image by restricting the migration operator to the optimum aperture. This aperture is centred around the stationary point and its size corresponds to the minimum aperture defined by the projected first Fresnel zone. For zero offset, both properties can be directly estimated from the

kinematic wavefield attributes which also allow to extrapolate the stationary point to finite offset. This strategy cannot be fully extended to 3D for arbitrary media. The 3D common-offset minimum-aperture migration approach considered here holds for mild to moderate lateral velocity variations which corresponds to the restrictions for time migration made in this thesis. The proposed application of the minimum-aperture migration in the time-migrated domain stabilises the approach originally introduced for depth migration.

I have applied the minimum-aperture approach to synthetic and real datasets. Furthermore, corresponding migration results with conventional aperture definition have been generated. The comparison has clearly exhibited improvements in the minimum-aperture migrated image: migration artifacts have been significantly reduced, operator aliasing has been avoided, and the overall noise level has been reduced. The focus of the application in the time-migrated domain concerns the quality of the migrated amplitudes. By restricting the migration operator to the optimum aperture size, the summation of unwanted noise is avoided and the amplitudes become more reliable and less scattered. As I have shown for a 2D example, this also has a direct impact on the reliability of AVO/AVA analyses.

The presented minimum-aperture migration approach in the time domain is based on the assumption of straight rays which limits its applicability to models of moderate complexity. The minimum-aperture concept is not tied to this assumption and might, therefore, be combined with more general time migration schemes. Irrespective of the employed scheme, the minimum-aperture approach strongly depends on the local reliability of the kinematic wavefield attributes. Thus, a diligent determination and evaluation of these attributes is crucial for practical application. In general, I consider the CRS-based minimum-aperture time migration as a complement rather than as a substitute for conventional Kirchhoff time migration, in particular if a target-oriented application in the context of a subsequent AVO/AVA analysis is considered.

List of Figures

Real data example

List of Tables

References

Abma, R., Sun, J., and Bernitsas (1999). Antialiasing methods in Kirchhoff migration. *Geophysics*, 64:1783–1792.

Aki, K. and Richards, P. G. (1980). *Quantitative seismology – theory and methods*, volume 1. W. H. Freeman & Co., San Fransisco.

Al-Chalabi, M. (1973). Series approximation in velocity and traveltime computations. *Geophys. Prosp.*, 21:783–795.

Baina, R., Nguyen, S., Noble, M., and Lambaré, G. (2003). Optimal anti-aliasing for ray-based Kirchhoff depth migration. In *Expanded Abstracts*. 73rd Ann. Internat. Mtg., Soc. Expl. Geophys. Session MIG P2.2.

Bancroft, J. and Sun, S. (2003). Fresnel zones and the power of stacking used in the preparation of data for AVO analysis. In *Expanded abstracts, 73rd Ann. Internat. Mtg.*, pages 231–234. Soc. Expl. Geophys.

Bergler, S. (2004). *On the determination and use of kinematic wavefield attributes for 3D seismic imaging*. Logos Verlag, Berlin.

Beylkin, G. (1985a). Imaging of discontinuities in the inverse scattering problem by inversion of a generalized Radon transform. *J. Math. Phys.*, 26:99–108.

Beylkin, G. (1985b). Reconstructing discontinuities in multidimensional inverse scattering problems. *Applied Optics*, 24:4086–4088.

Bleistein, N. (1984). *Mathematical methods for wave phenomena*. Academic Press Inc., San Diego.

Bleistein, N. (1987). On the imaging of reflectors in the earth. *Geophysics*, 52:931–942.

Bleistein, N., Cohen, J., and Stockwell Jr., J. (2001). *Mathematics of Multidimensional Seismic Imaging, Migration, and Inversion*. Springer Verlag, New York.

Boelsen, T. and Mann, J. (2005a). 2D CO CRS stack for multi-component seismic reflection data. In *Extended abstracts, 67th Conf.* Eur. Assn. Geosci. Eng. Session P063.

Boelsen, T. and Mann, J. (2005b). 2D CO CRS stack for OBS and VSP data and arbitrary top-surface topography. In *Extended abstracts, 67th Conf.* Eur. Assn. Geosci. Eng. Session P181.

Born, M. and Wolf, E. (1959). *Principles of optics*. Pergamon Press Inc., Oxford.

References

Bortfeld, R. (1989). Geometrical ray theory: rays and traveltimes in seismic systems (second-order approximations of the traveltimes). *Geophysics*, 54(3):342–349.

Buttkus, B. (2000). *Spectral analysis and filter theory in Applied Geophysics*. Springer Verlag, Berlin.

Castagna, J. and Backus, M., editors (1993). *Offset-dependent reflectivity – theory and practice of AVO analysis*. Soc. Expl. Geophys.

Červený, V. (2001). *Seismic ray theory*. Cambridge University Press, Cambridge.

Červený, V. and Soares, J. (1992). Fresnel volume ray tracing. *Geophysics*, 57:902–915.

Chapman, C. (2004). *Fundamentals of Seismic Wave Propagation*. Cambridge University Press, Cambridge.

Dix, C. H. (1955). Seismic velocities from surface measurements. *Geophysics*, 20(1):68–86.

Duveneck, E. (2004). *Tomographic determination of seismic velocity models with kinematic wavefield attributes*. Logos Verlag, Berlin.

Gajewski, D., Coman, R., and Vanelle, C. (2002). Amplitude preserving Kirchhoff migration: a traveltime based strategy. *Studia geophysica et geodaetica*, 46:193–211.

Gray, S. (2001). Seismic imaging. *Geophysics*, 66(1):15–17.

Hagedoorn, J. (1954). A process of seismic reflection interpretation. *Geophys. Prosp.*, 2:85–127.

Hanitzsch, C. (1997). Comparison of weights in prestack amplitude-preserving Kirchhoff depth migration. *Geophysics*, 62:1812–1816.

Heilmann, Z. (2002). The Common-Reflection-Surface Stack under Consideration of the Acquisition Surface Topography and the Near-Surface Velocity Gradient. Master's thesis, University of Karlsruhe.

Hertweck, T., Jäger, C., Goertz, A., and Schleicher, J. (2003a). Aperture effects in 2.5D Kirchhoff migration: a geometrical explanation. *Geophysics*, 68(5):1673–1684.

Hertweck, T., Jäger, C., Mann, J., and Duveneck, E. (2003b). An integrated data-driven approach to seismic reflection imaging. In *Extended abstracts, 65th Conf.* Eur. Assn. Geosci. Eng. Session P004.

Höcht, G. (2002). *Traveltime approximations for 2D and 3D media and kinematic wavefield attributes*. PhD thesis, University of Karlsruhe.

Höcht, G., de Bazelaire, E., Majer, P., and Hubral, P. (1999). Seismics and optics: hyperbolae and curvatures. *J. Appl. Geophys.*, 42(3,4):261–281.

Hubral, P. (1983). Computing true amplitude reflections in a laterally inhomogeneous earth. *Geophysics*, 48(8):1051–1062.

Hubral, P., Höcht, G., and Jäger, R. (1998). An introduction to the Common Reflection Surface stack. In *Extended abstracts, 60th Conf.* Eur. Assn. Geosci. Eng. Session 1-19.

Hubral, P. and Krey, T. (1980). *Interval velocities from seismic reflection traveltime measurements.* Soc. Expl. Geophys., Tulsa.

Hubral, P., Schleicher, J., Tygel, M., and Hanitzsch, C. (1993). Determination of Fresnel zones from traveltime measurements. *Geophysics*, 58(5):703–712.

Hubral, P., Schleicher, S., and Tygel, M. (1992a). Three-dimensional Paraxial Ray Properties. Part I: Basic Relations. *J. Seis. Expl.*, 1:265–279.

Hubral, P., Schleicher, S., and Tygel, M. (1992b). Three-dimensional Paraxial Ray Properties. Part II: Applications. *J. Seis. Expl.*, 1:347–362.

Jäger, C. (2005a). Minimum-aperture Kirchhoff migration by means of CRS attributes. In *Extended abstracts, 67th Conf.* Eur. Assn. Geosci. Eng. Session F042.

Jäger, C. (2005b). *Minimum-aperture Kirchhoff migration with CRS stack attributes.* Logos Verlag, Berlin.

Klüver, T. and Mann, J. (2005). Event-consistent smoothing and automated picking in CRS-based seismic imaging. In *Expanded abstracts, 75th Ann. Internat. Mtg.* Soc. Expl. Geophys. Session SPMI 3.6.

Koglin, I. and Ewig, E. (2003). Residual static correction by means of CRS attributes. In *Expanded Abstracts, 73th Ann. Internat. Mtg.* Soc. Expl. Geophys. Session SP 1.4.

Lay, T. and Wallace, T. (1995). *Modern Global Seismology.* Academic Press, San Diego.

Liner, L. (1999). Concepts of normal and dip moveout. *Geophysics*, 64:1637–1647.

Loewenthal, D., Lu, L., Robertson, R., and Sherwood, J. (1976). The wave equation applied to migration. *Geophys. Prosp.*, 24(2):380–399.

Mann, J. (2002). *Extensions and applications of the Common-Reflection-Surface Stack method.* Logos Verlag, Berlin.

Mann, J. and Duveneck, E. (2004). Event-consistent smoothing in generalized high-density velocity analysis. In *Expanded Abstracts, 74th Ann. Internat. Mtg.* Soc. Expl. Geophys. Session ST 1.1.

Mann, J., Hubral, P., Traub, B., Gerst, A., and Meyer, H. (2000). Macro-model independent approximative prestack time migration. In *Extended abstracts, 62nd Conf.* Eur. Assn. Geosci. Eng. Session B-52.

Martins, J., Schleicher, J., Tygel, M., and Santos, L. (1997). 2.5-D True-amplitude Migration and Demigration. *J. Seis. Expl.*, 6:159–180.

Mosher, C., Keho, T., Weglein, A., and Foster, D. (1996). The impact of migration on AVO. *Geophysics*, 61(6):1603–1615.

Müller, A. (2003). The 3D Common-Reflection-Surface stack – theory and application. Master's thesis, University of Karlsruhe.

Müller, N.-A. (2005). 3-D inversion with kinematic wavefield attributes. In *Extended abstracts, 67th Conf.* Eur. Assn. Geosci. Eng. Session B040.

References

Müller, N.-A. (2006). Elimination of the spread-length bias in the common-reflection-surface stack. In *Expanded abstracts, 76th Annual Meeting*. Soc. Expl. Geophys.

Müller, T. (1998). Common Reflection Surface stack versus NMO/stack and NMO/DMO/stack. In *Extended abstracts, 60th Conf.* Eur. Assn. Geosci. Eng. Session 1-20.

Newman, P. (1975). Amplitude and Phase Properties of a Digital Migration Process. In *Extended Abstracts, 37th Conf.* Europ. Assoc. Expl. Geoph. (Republished in: First Break, 8:397-403, 1990).

Popov, M. and Pšenčík, I. (1978). Computation of ray amplitudes in inhomogeneous media with curved interfaces. *Studia geoph. et geod.*, 22:248–258.

Robein, E. (2003). *Velocities, Time-imaging and Depth-imaging in Reflection Seismics: Principles and Methods*. EAGE Publications, Houten.

Schleicher, J., Hubral, P., Tygel, M., and Jaya, M. S. (1997). Minimum apertures and Fresnel zones in migration and demigration. *Geophysics*, 62(1):183–194.

Schleicher, J. and Santos, L. T. (2001). Resolution of Kirchhoff depth migration: offset and angle dependency. In *Ann. Report*, volume 5. Wave Inversion Technology Consortium.

Schleicher, J., Tygel, M., and Hubral, P. (1993). 3-D true-amplitude finite-offset migration. *Geophysics*, 58(8):1112–1126.

Schleicher, J., Tygel, M., and Hubral, P. (2007). *Seismic True-Amplitude Imaging*. Soc. Expl. Geophys., Tulsa.

Schneider, W. (1978). Integral formulation for migration in two and three dimensions. *Geophysics*, 43(1):49–76.

Sheriff, R. (1975). Factors affecting seismic amplitudes. *Geophys. Prosp.*, 23:125–138.

Sheriff, R. E. and Geldart, L. P. (1982). *Exploration Seismology*, volume 1. Cambridge Univ. Press, Cambridge.

Shuey, R. (1985). A simplification of the Zoeppritz equations. *Geophysics*, 50:607–614.

Trappe, H., Mann, J., and Buske, S. (2005). High-resolution images of subsurface CO_2 storage sites in time and depth by the CRS methodology (CO2CRS). *Geotechnologien Science Report No. 6: Investigation, utilization and protection of the underground*. Koordinierungsbüro Geotechnologien.

Ursin, B. (1982). Quadratic wavefront and traveltime approximations in inhomogeneous layered media with curved interfaces. *Geophysics*, 47(7):1012–1021.

Vermeer, G. J. O. (2002). *3-D seismic survey design*. Soc. Expl. Geophys., Tulsa.

Walden, A. T. (1991). Making AVO sections more robust. *Geophys. Prosp.*, 39:915–942.

Xu, S., Chauris, H., Lambaré, G., and Noble, M. (2001). Common-angle migration: A strategy for imaging complex media. *Geophysics*, 66:1877–1894.

Yilmaz, Ö. (2001). *Seismic data analysis, vols. 1 and 2*. Soc. Expl. Geophys., Tulsa.

Zhang, Y., Gray, S., Sun, J., and Notfors, C. (2001). Theory of migration anti-aliasing. In *Expanded Abstracts*. 71st Ann. Internat. Mtg., Soc. Expl. Geophys. Session MIG 4.7.

Zhang, Y., Gray, S., and Young, J. (2000). Exact and approximate weights for Kirchhoff migration. In *Expanded Abstracts, 70th Ann. Internat. Mtg.* Soc. Expl. Geophys. Session MIG 10.8.

Zhang, Y., Höcht, G., and Hubral, P. (2002). 2D and 3D ZO CRS stack for a complex top-surface topography. In *Extended abstracts, 64th Conf.* Eur. Assn. Geosci. Eng. Session P166.

Ziolkowski, R. and Deschamps, G. (1980). The Maslov method and the asymptotic Fourier transform: Caustic analysis. Electromagnetic Laboratory Scientific report 80-9, University of Illinois.

Zoeppritz, K. (1919). Erdbebenwellen VII: Über Reflexion und Durchgang seismischer Wellen durch Unstetigkeitsflächen. *Nachrichten der Königlichen Gesellschaft der Wissenschaften zu Göttingen*, pages 66–84.

Danksagung

Zur Entstehung dieser Dissertation haben zahlreiche Personen direkt oder indirekt beigetragen. Im Einzelnen gilt mein Dank besonders:

Prof. Dr. Peter Hubral danke ich für die Betreuung meiner Arbeit und die Übernahme des Referats. Er ließ mir viel Freiheit bei der Gestaltung meines Themas und hat mich jederzeit in allen Belangen unterstützt.

Prof. Dr. Dirk Gajewski danke ich für die Übernahme des Korreferats und sein Interesse an meiner Arbeit.

Alex Müller danke ich für Alles, was er für mich getan hat. Er weiss, was er mir bedeutet.

Dr. Jürgen Mann möchte ich für seine stete Unterstützung und Hilfsbereitschaft danken. Ungezählte Male ist er mit mir auf Fehlersuche gegangen und hatte stets ein offenes Ohr für meine Probleme. Dafür und für das Korrekturlesen dieser Arbeit bin ich ihm zu großen Dank verpflichtet.

Auch bei den anderen Mitgliedern meiner Arbeitsgruppe, namentlich **Mareike Kienast**, **Tilman Klüver** und **Markus von Steht**, möchte ich mich bedanken. Durch Diskussionen oder Hilfe bei der Lösung programmier- oder anwendungstechnischer Probleme haben sie mir immer wieder geholfen, meine Arbeit voranzubringen.

Ebenso möchte ich mich bei **Dr. Thomas Hertweck** für das Korrekturlesen meiner Arbeit bedanken. Trotz seiner vielen Verpflichtungen fand er immer wieder Zeit dazu, und war auch bei allen anderen Problemen ein hilfsbereiter und kompetenter Ansprechpartner.

Die Kaffeepausen mit **Paola Ledermann** und meinen bereits genannten Arbeitskollegen waren Anlass für viele interessante Gespräche nicht nur zu fachlichen Themen und lieferten neue Ideen.

I wish to thank *ENI S.p.A.*, in particular **Paolo Marchetti**, for their cooperation in the scope of this thesis.

Claudia Payne danke ich für Ihre stete Hilfsbereitschaft und unendliche Geduld bei allen organisatorischen und bürokratischen Problemen.

Meinen Eltern danke ich für all ihre Unterstützung während meines Studiums und der Doktorandenzeit.

Lebenslauf

Persönliche Daten

Name:	Miriam Spinner
Geburtsdatum:	27.08.1975
Nationalität:	deutsch
Geburtsort:	Ludwigshafen

Schulausbildung

1982 - 1986	Schiller Grundschule Brühl
1986 - 1995	Johann-Sebastian-Bach Gymnasium Mannheim
23.06.1995	Allgemeine Hochschulreife

Hochschulausbildung

1995 - 1998	Studium der Geologie an der Universität Heidelberg
26.03.1998	Vordiplom in Geologie/Paläontologie
1998 - 2000	Studium der Geophysik an der Universität Kiel
25.07.2000	Vordiplom in Geophysik
2000 - 2003	Studium der Geophysik an der Universität Karlsruhe (TH)
01.12.2003	Diplom in Geophysik
seit 2004	Doktorand am Geophysikalischen Institut der Universität Karlsruhe (TH)